Balancing act: investigating the coordinated mechanics of germband and amnioserosa in *Drosophila* morphogenesis

By

Monica Elaine Bennett

Dissertation

Submitted to the Faculty of the

Graduate School of Vanderbilt University

in partial fulfillment of the requirements

for the degree of

DOCTOR OF PHILOSOPHY

in

Physics

May, 2017

Nashville, Tennessee

Approved:

M. Shane Hutson, Ph.D.

Andrea Page-McCaw, Ph.D.

Erin Rericha, Ph.D.

John Wikswo, Ph.D.

To my excellent husband Daniel, who made me a Mrs. before a Dr.

and

To my parents, Lee and Yvonne, and sister, Melissa

ACKNOWLEDGMENTS

TABLE OF CONTENTS

LIST OF TABLES

LIST OF FIGURES

CHAPTER 1

Introduction

This chapter offers a brief overview of several topics that are germane and necessary for understanding the chapters that follow. First, I will introduce the model organism used for my research and explain its relevant features and the general focus of my work in terms of its development. Next, I will offer a brief explanation of the aims of biophysical study of biological systems, pointing out the differences in approach and scope between traditional biology and biophysics. I will close by presenting the developmental context for each chapter in the dissertation, and provide a recommended order of reading for emphasis on new experimental results.

Basics of *Drosophila melanogaster*

Drosophila melanogaster (the fruit fly) is a popular model organism in the realm of biology, and increasingly also in biophysics. The reasons for its popularity in biophysics are discussed at more length in the course of this dissertation, but the features that recommend it generally for research include the extensive gene homology that allows comparison to more complex organisms and the relative ease of care and breeding (see Chapter 3 for a brief discussion). It is also preferred for its quick generational turnover, thanks to its relatively short life cycle. *Drosophila* has an embryonic period of about twenty-four hours, during which it develops into a complex, multicellular embryo; the ensuing larval stage lasts about four days and involves three phases, or instars, characterized by noticeable changes in size and activity. At the end of the third instar, the larva forms a pupal casing and enters four days of pupation, in which many of the tissues and structures of the larva break down into a "soup" while the imaginal discs rearrange to form the body of the adult fruit fly. After metamorphosis is complete, the fly leaves the pupal casing, or ecloses (Brody, 1999). Once the adult emerges, it is fully matured and ready to breed

after 8-10 hours and can live for about 30 days. Figure 1-1 shows a general overview of the complete metamorphosis of *Drosophila*.
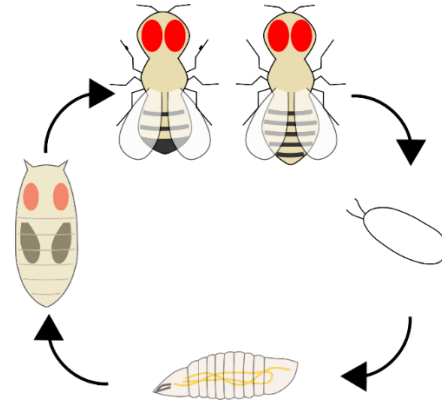
Fig 1-1. Life cycle of *Drosophila melanogaster*.

For biophysicists, *Drosophila* is of particular interest during embryonic development, which involves a series of morphogenetic stages that feature complex and extensive tissue specification, migration, and rearrangement. This work deals mostly with these embryonic stages, organized in Table 1-1 using the Bownes categorization of embryonic development. This is an incomplete list, with the stages included that are of most interest to this research, including specification, germband extension and retraction, and dorsal closure.

Bownes stage	Events	Time after fertilization
2	Mitotic cycles 1-9	15-70 min
3	Nuclear division 9	70-90 min
4	Mitotic cycles 1-10	90-130 min
5	Cellularization	130-180 min
8	Quick phase of germband extension	200-230 min
9	Slow phase of germband extension	230-260 min
12	Germband retraction	440-560 min
14	Dorsal closure begins	620 min
15	Dorsal closure ends	800 min

Table 1-1. Selected list of Bownes stages of embryonic development in *Drosophila*. Stages are listed as they appear on The Interactive Fly (Brody, 1999).

Major Questions of Biophysics

In studying *Drosophila*, biophysicists have somewhat different interests than the biologists who have accumulated the decades of knowledge that gives us the foundation of our work—a thoroughly documented developmental process, along with a well-sequenced genome and an arsenal of powerful genetic tools. Applying physics to biological systems often includes traditional methods like knockdowns and assays, using the available information to pursue answers not only about the underlying genetics and signaling, but also about the mechanisms of physical change at multiple scales. Of particular relevance to this dissertation, biophysical research at the cellular and tissue level approaches the questions of *Drosophila* development by seeking to understand the forces driving the dramatic migrations, deformations, and invaginations that characterize morphogenesis. These forces cannot and should not be separated from biological considerations, since a full picture of the developmental process involves actin and myosin II recruitment, apoptotic signaling, and countless other interactions of proteins and signals. However, a basic understanding of the biophysics at work can begin with the origins and effects of mechanical forces, which can then be combined with detailed knowledge of cellular processes to give more complete answers to the mysteries that still surround many of the best-described developmental events.

Biophysical approaches to biological events involve investigating the viscoelastic properties of the tissues and examining the physical evidence of applied forces. Both of these avenues of research have paved the way for the work presented in this dissertation, which builds on the existing models of forces in *Drosophila* development and adds to the store of knowledge in this field. This work represents another step toward the ultimate goal of these studies—to both understand the chemical and biological causes, and quantify the magnitude and effects, of the mechanical forces of morphogenesis.

Amnioserosal Roles in Development

In addition to the epithelial germband whose development plays a key role in morphogenesis, *Drosophila* embryos contain a somewhat unique tissue among insects, called the amnioserosa. The amnioserosa is extraembryonic, meaning that it is no longer present in the fully developed embryo, and is named for its origin as a combination of the two extraembryonic tissues that occur in most insects, the amnion and serosa. Unlike these two tissues, the amnioserosa remains contiguous with the germband during its lifetime, so that the amnioserosa and germband move in concert with each other and in some ways act as a single tissue. Through this contact, the amnioserosa acts as a critical part of the system of interacting points of contact and forces that drive some of the most dramatic events of morphogenesis. No study of the mechanics of morphogenesis is complete without an understanding of the amnioserosa's active role in multiple aspects of development.

Chapter 2 of this dissertation presents a literature review that acts as an extended introduction to the interactions between amnioserosa and germband, familiarizing the reader with the state of knowledge on the two connected tissues. This chapter gives an overview of the major morphogenetic events of specification, germband extension, germband retraction, and dorsal closure, and the amnioserosa's part in each; it also covers the evolutionary origin of the amnioserosa as a single tissue. In the context of the dissertation, which centers on the amnioserosa's role in development as a common theme, the review will inform the reader about the developmental stages that are of interest in the subsequent research, as well as the knowns and unknowns of the germband-amnioserosa relationship.

Beta-Theta Analysis

With a better understanding of the general sequence of morphogenetic events and the open questions in the area of developmental mechanics, we can move from the general information of the literature review to the original research paper included as Chapter 4 in this dissertation. This paper

presents data collected from the germband, not the amnioserosa, but it addresses the question of the balance between the active roles of the germband and amnioserosa in germband retraction; the two are interlinked so that information about one leads to greater understanding of the other.

Preceding this research, Chapter 3 offers brief explanations of related background information: *Drosophila* breeding, image collection and analysis, modeling, and cellular force inference methods. This material provides the context for the data presented in Chapter 4, which investigates the internal tensions or polarization of the germband during retraction. The findings discussed in this chapter increase our understanding of the internal workings of the germband and suggest implications for understanding the balance between amnioserosal and internal germband forces, within the events of retraction and in combination with earlier developmental stages.

Conclusions and Other Work

Following the discussion of experimental results in Chapter 4, I present conclusions to be drawn from the preceding work, as well as unanswered questions and future work. This chapter draws on material from the research of Chapter 4 and the general knowledge of Chapter 2. Following these final remarks are several appendices providing extra content and detailing related avenues of research that have not resulted in publication. These sections offer a more detailed look at the theory underlying beta-theta analysis and supplemental data for Chapter 4, as well as reports of research on photoactivatable GTPases and cell apoptosis in heat-shocked embryos.

Navigating This Work

As described above, this thesis contains a literature review on the amnioserosa's evolutionary history and role in retraction and other morphogenetic events, in addition to original research on the germband and amnioserosa in germband retraction. For the reader who is most interested in the content and implications of the research in Chapter 4, it is useful to read parts of Chapter 2

(Introduction, Germband Extension, and Germband Retraction) for basic knowledge of germband retraction and the surrounding developmental stages, and at least several sections of Chapter 3 (Finite Element Modeling, Force Anisotropy and Parameter Space, and Cellular Force Inference Methods). As companions to Chapter 4, Appendices A and B provide, respectively, more detail on the theory of beta-theta analysis and supplemental data. These parts of the dissertation will be sufficient to understand the content of Chapter 4 in relation to the relevant biological and mathematical background.

Although the research presented in Chapter 4 gives a special focus on the essential stage of germband retraction, this dissertation in its entirety encompasses several avenues of research. Most of these topics involve in some way the connection between germband and amnioserosa that is necessary for retraction and several other developmental stages in the *Drosophila* embryo. The dynamics of this balance are far from fully understood, as the following chapters will attest, affording numerous and varied opportunities for current and future biophysics research.

CHAPTER 2

Amnioserosa development and function in *Drosophila* embryogenesis: critical mechanical roles for an extraembryonic tissue

Authors of Manuscript

Monica E. Lacy and M. Shane Hutson

Abstract

Despite being a short-lived, extraembryonic tissue, the amnioserosa plays critical roles in the major morphogenetic events of *Drosophila* embryogenesis. These roles involve both cellular mechanics and biochemical signaling. Its best-known role is in dorsal closure – well-studied by both developmental biologists and biophysicists – but the amnioserosa is also important during earlier developmental stages. Here, we provide an overview of amnioserosa specification and its role in several key developmental stages: germband extension, germband retraction, and dorsal closure. We also compare embryonic development in *Drosophila* and its relative *Megaselia* to highlight how the amnioserosa and its roles have evolved. Placed in context, the amnioserosa provides a fascinating example of how signaling,

mechanics and morphogen patterns govern cell-type specification and subsequent morphogenetic changes in cell shape, orientation, and movement.

Introduction

The amnioserosa is essential to embryonic development, despite being an extraembryonic tissue that lasts through only the first half of embryogenesis (St Johnston and Nüsslein-Volhard, 1992; Frank and Rushlow, 1996; Schöck and Perrimon, 2002; Harris et al., 2009). During its short lifetime, the amnioserosa is a highly morphogenetically active tissue, undergoing dramatic changes in cell and tissue shape (Kiehart et al., 2000; Schöck and Perrimon, 2002; Pope and Harris, 2008; Solon et al., 2009). These changes are critical to proper morphogenesis: embryos without an amnioserosa exhibit defects in germband retraction and dorsal closure (Frank and Rushlow, 1996); and similar defects occur when amnioserosa-embryo connections and/or signaling are abnormal (Reed et al., 2004). The amnioserosa's function in dorsal closure has been studied extensively as a model process for wound healing (Kiehart et al., 2000; Wood et al., 2002; Belacortu and Paricio, 2011) and has been reviewed recently (Heisenberg, 2009; Gorfinkiel et al., 2011). This review aims to provide a broader discussion of how the amnioserosa is specified, how it has evolved, and how it contributes to morphogenetic mechanics and signaling during earlier developmental stages.

Figure 2-1 presents an overview of these developmental phases, showing a lateral view of a *Drosophila* embryo through Bownes Stage 12 (Fig. 2-1(A-D)) and then switching to a dorsal view (Fig. 2-1(E-G)). The amnioserosa forms during cellularization and early gastrulation as a monolayer on the dorsal surface (Panfilio, 2008). It spreads during germband extension to cover large portions of the embryo's lateral flanks (Fig. 2-1(A-B)) (Pope and Harris, 2008) and then retracts during germband retraction (Fig. 2-1(C-D)) to reshape into a dorsally located ovoid (Fig. 2-1(E)) (Schöck and Perrimon, 2002). Dorsal closure then commences with amnioserosa cells contracting apically and later invaginating (Kiehart et al., 2000).
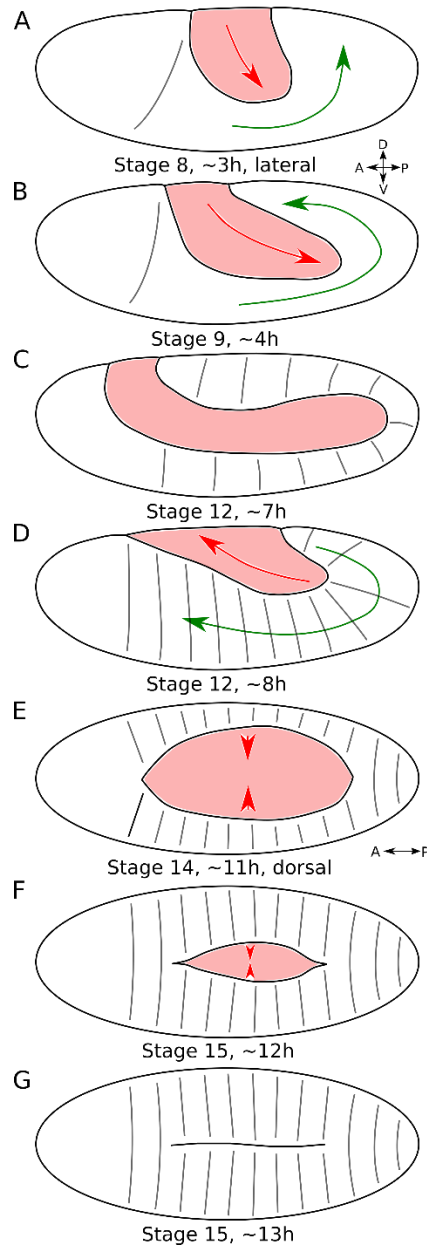
Figure 2-1. Overview of major stages in *Drosophila* development. Amnioserosa highlighted in pink. Lateral view in (A-D) and dorsal view in (E-G) with embryonic axes as indicated (A=anterior, P=posterior, D=dorsal, V=ventral). Red and green arrows throughout mark the directions of movement for amnioserosa and germband respectively. (A) Early germband extension: amnioserosa is partly extended; cephalic furrow is visible. (B) Late germband extension: amnioserosa is mostly extended; cephalic furrow is still visible. (C) Onset of germband retraction: amnioserosa is fully extended, but about to begin retracting; segmental furrows are visible in the germband, deepening during the pause between extension and retraction. (D) Mid-germband retraction: amnioserosa is partly retracted; some germband segments have visibly retracted around the posterior end. (E) Onset of dorsal closure: germband and amnioserosa have fully retracted; amnioserosa is beginning to contract. (F) Mid-dorsal closure: amnioserosa is contracting and invaginating; some germband segments have fused at the dorsal midline. (G) Completion of dorsal closure: epidermis is fused at dorsal midline; amnioserosa undergoes apoptosis.

9

By the end of this process, the dorsalmost cells of the lateral epidermis "zip" together to completely

cover the invaginated amnioserosa as it undergoes apoptosis (Fig. 2-1(E-G)) (Jacinto et al., 2002a;

Fernández et al., 2007; Cormier et al., 2012).

Dorsal Closure

Dorsal closure has been reviewed elsewhere (Harden, 2002; Jacinto et al., 2002b; Heisenberg,

2009; Gorfinkiel et al., 2011), so we include only a brief discussion here. This stage poses challenging

problems in biomechanics, with several force-generating mechanisms acting concurrently to pull the

lateral epidermis over the invaginating amnioserosa (Fig. 2-2). The lateral epidermis contributes through

multiple mechanisms including Decapentaplegic-regulated adhesion to peripheral amnioserosa cells (Fig.

2-2(A-B), square insets) (Stark et al., 1997; Stronach and Perrimon, 2001; Fernández et al., 2007; Wada et

al., 2007), formation and contraction of supracellular actomyosin cables in its leading edges (Fig. 2-2(A-

B), square insets) (Jacinto et al., 2002a), and lamellipodial- or filopodial-mediated zipping together of the

leading edges from opposite flanks (Fig. 2-2(B), square insets) (Hutson et al., 2003; Toyama et al., 2008;

Martin, 2010; Azevedo et al., 2011; Saias et al., 2015). The amnioserosa contributes through apoptosis-

driven cell extrusion (Toyama et al., 2008; Cormier et al., 2012), cell volume loss (Saias et al., 2015), and

myosin II-driven apical contractions (Fig. 2-2(A-B), circle insets) (Kiehart et al., 2000; Fernández et al.,

2007; Gorfinkiel et al., 2009; Harris et al., 2009; Solon et al., 2009; Blanchard et al., 2010; Azevedo et al.,

2011; Fischer et al., 2014). Its peripheral cells may also form and contract their own supracellular

actomyosin cables (Wada et al., 2007).

Despite a wealth of studies, the assignment of proper roles and interactions among these

mechanisms is not yet resolved. Contractile forces within the amnioserosa may increase with time or

may remain constant and rely on cell volume decreases to reduce resistance from intracellular pressures

(Saias et al., 2015). Stochastic early apoptosis of amnioserosa cells may provide between a half and a
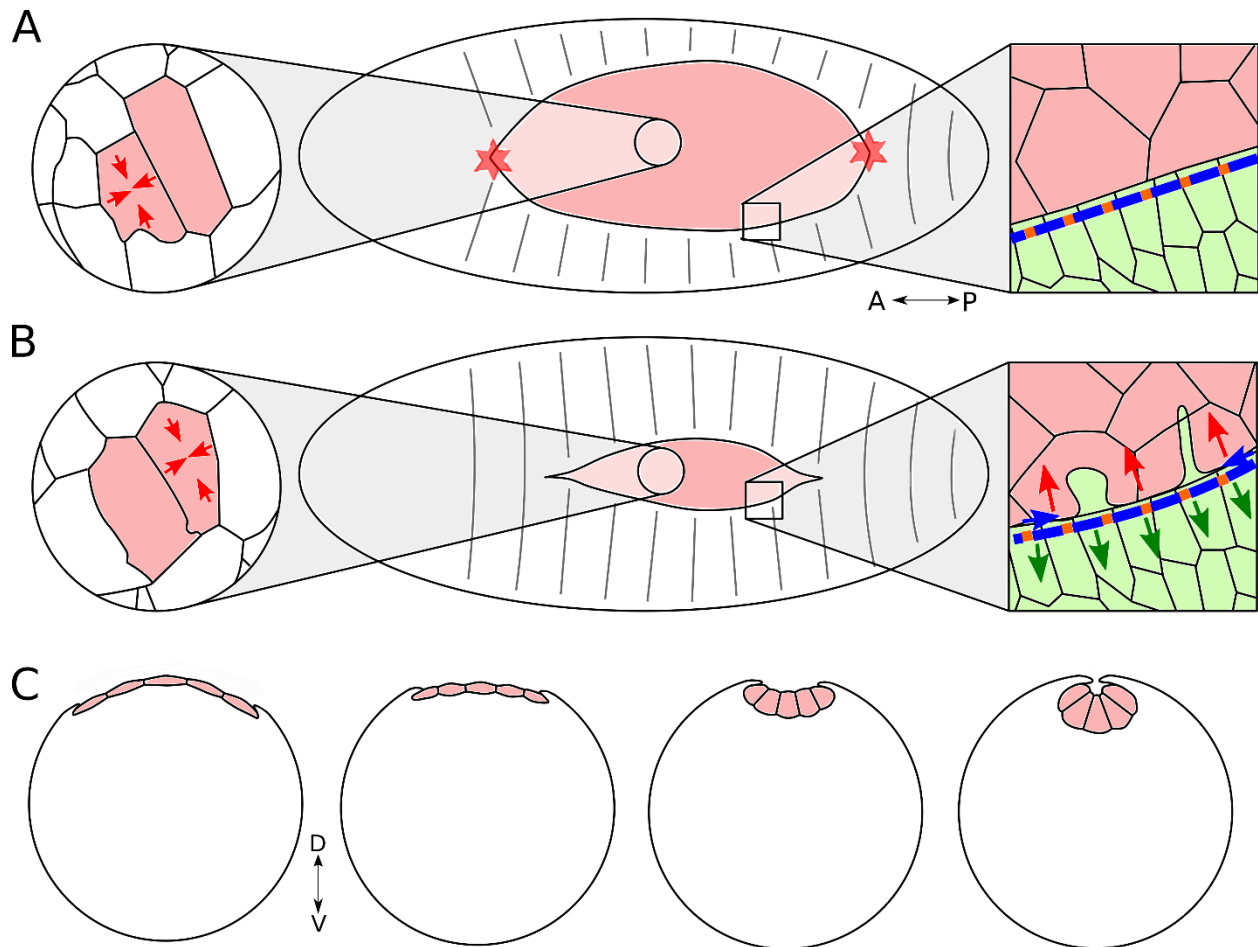
Figure 2-2. Dorsal closure. Embryonic axes as indicated (A=anterior, P=posterior, D=dorsal, V=ventral). Amnioserosa highlighted in pink. (A) Dorsal view of early dorsal closure. Canthi are marked with red stars. Circle inset shows cells undergoing asynchronous pulsation (red arrows showing contraction). Square inset shows the interface of amnioserosa and lateral epidermis. The supracellular actomyosin cable along the leading edge is marked blue with orange at cell junctions. (B) Dorsal view of mid-dorsal closure. Circle inset shows amnioserosa cells continuing pulsation, with a neighboring cell now undergoing contraction. Square inset shows the interface of amnioserosa and lateral epidermis with the actomyosin cable and examples of leading edge projections: lamellipodium (left) and filopodium (right). Arrows represent forces from the amnioserosa (red), actomyosin cable (blue), and lateral epidermis (green). (C) Transverse view of amnioserosa cells during closure. The leading edge cells (and later the underlying cardioblasts) migrate dorsally as amnioserosa cells initially contract without changing depth. As closure continues, amnioserosa cells become bottle-shaped and invaginate below the leading edge epithelial and cardioblast cells. After leading edge cells zip together the epidermis at the dorsal midline, internalized amnioserosa cells apoptose.

third of the amnioserosa's total contractile force (Toyama et al., 2008; Cormier et al., 2012) or may

instead increase the speed of zipping at the amnioserosa's canthi (Gorfinkiel et al., 2009). Zipping at the

canthi may not even be necessary: cutting one or both canthi using laser ablation decreases actomyosin

cable tension, but has little effect on the rate of amnioserosa contraction and epidermal fusion (Wells et

al., 2014). Finally, the leading edges' supracellular cables may function as purse-strings that actively pull

the lateral epidermis dorsalward (Kiehart et al., 2000; Hutson et al., 2003), or as restraints that coordinate dorsal advances among epidermal segments (Jacinto et al., 2002a), or as ratchets that passively lock in the epidermis' incremental advances (Solon et al., 2009).

However these mechanisms are coordinated, amnioserosa cells wedge into bottle-shaped cells (Fig. 2-2(C)) to eventually invaginate as lateral epidermis cells advance toward the dorsal midline. Once at the midline, Rac1- and Cdc42-regulated lamellipodia and filopodia help match up appropriate epidermal segments from opposite flanks (Jacinto et al., 2000; Fernández et al., 2007; Pickering et al., 2013), fusing the two flanks into a single coherent tissue. Amnioserosa cells are then separated from the leading edge by cardioblasts that will form the larval heart (Rugendorff et al., 1994) and the internalized amnioserosa cells apoptose (Cormier et al., 2012).

As highlighted by the summary above, dorsal closure has been much studied by both developmental biologists and biophysicists as a key model system for investigating the interplay of genetics and mechanics in development. In the sections below, we examine how the amnioserosa is initially specified and how its involvement in earlier developmental events (Fig. 2-1) sets the stage for dorsal closure.

Amnioserosa Specification (Bownes Stages 4-6, 6.5-8 hours pre-DC)

The amnioserosa develops from about 200 of the 6000 cells that form during cellularization (Hartenstein and Campos-Ortega, 1985; Schweisguth et al., 1991; St Johnston and Nüsslein-Volhard, 1992; Mazumdar and Mazumdar, 2002; Harris et al., 2009; Simonova and Burdina, 2009; Figard et al., 2013). Its extent is specified by the expression pattern of *zerknüllt* (*zen*), which is itself shaped by gradients of the morphogens Decapentaplegic (Dpp) and Dorsal (Créton et al., 2000; Rushlow et al., 2001; Schmidt-Ott et al., 2010).
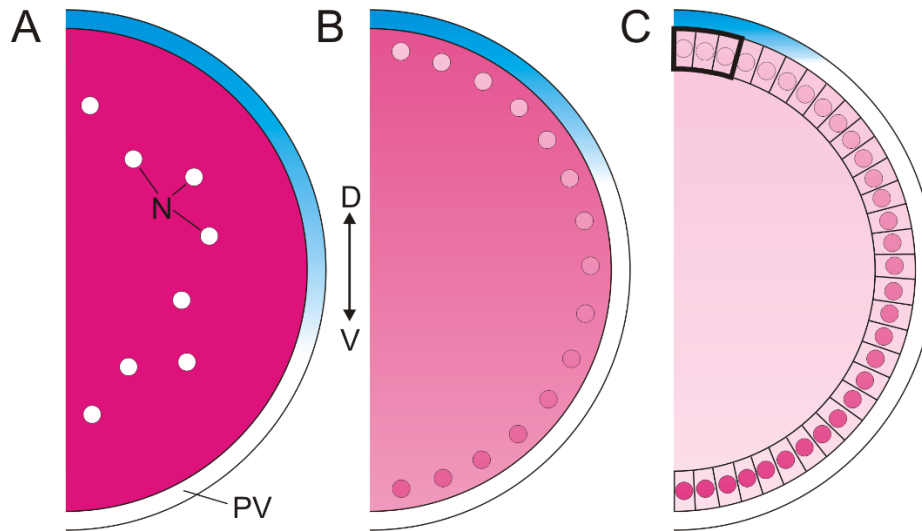
Figure 2-3. Specification. Transverse cross-sections of an early *Drosophila* embryo (only one lateral half is shown) with dorsal (D) up and ventral (V) down. Magenta and cyan shading respectively represent dynamic distributions of the signaling proteins Dorsal and Decapentaplegic (Dpp). (A) Pre-cellularization, nuclear cycles 1-9. Dorsal protein is uniformly distributed throughout the shared cytoplasm and does not enter nuclei (N). Dpp is found in the extracellular perivitelline fluid (PV) with a gradient that spans the dorsal half of the embryo. (B) Pre-cellularization, nuclear cycles 10-13. Dorsal protein now enters nuclei, under control of the Toll signaling pathway, and forms a gradient of nuclear localization that is highest at the ventral midline. More Dorsal protein is taken into ventral nuclei and depleted from the shared cytoplasm with each nuclear division. The Dpp gradient is narrowing toward the dorsal midline. (C) Completion of cellularization, nuclear cycle 14. Dorsal protein is almost exclusively present in nuclei, most strongly so in ventral nuclei. Dorsal protein levels in the dorsalmost nuclei are approximately equal to the cytoplasmic level. The Dpp gradient has narrowed to an intense, narrow stripe in the dorsalmost 10% of the embryo, tapering off sharply to either side. The dorsalmost 10% of cells – about three cells on either side of the dorsal midline – corresponds to the presumptive amnioserosa (thick black outline).

The Dorsal gradient is one of nuclear localization, with highest (lowest) nuclear concentrations in cells along the ventral (dorsal) midline (Fig. 2-3(A-B)) (Arora and Nusslein-Volhard, 1992; Créton et al., 2000; Kanodia et al., 2009). This gradient is initiated by active Toll signaling (St Johnston and Nüsslein-Volhard, 1992; Morisalo and Anderson, 1995; Moussian and Roth, 2005; Valanne et al., 2011; Haskel-Ittah et al., 2012) and is highly dynamic during the thirteen synchronous mitoses before cellularization (Fig. 2-3(A-B)) (Kanodia et al., 2009; Liberman et al., 2009; Bothma et al., 2010; Reeves et al., 2012). After cellularization (Fig. 2-3(C)), the Dorsal gradient stabilizes to directly and indirectly regulate zygotic transcription of some 60-70 target genes within broad ventral, lateral, and dorsal domains corresponding to high, medium and low Dorsal levels (Arora and Nusslein-Volhard, 1992; St Johnston and Nüsslein-Volhard, 1992; Jiang et al., 1993; Francois et al., 1994; Morisalo and Anderson, 1995; Hong et al., 2008).

13

The Dpp gradient is one of extracellular concentration, highest in the dorsalmost regions of perivitelline fluid (Fig. 2-3(B)) (Edgar and O'Farrell, 1989; Araujo and Bier, 2000; Ashe et al., 2000; Créton et al., 2000). The Dorsal gradient directly regulates transcription of *dpp* (Ferguson and Anderson, 1992; Huang et al., 1993), restricting it to the dorsalmost forty percent of the embryo (Nguyen et al., 1998; Ashe et al., 2000; Decotto and Ferguson, 2001; Sutherland et al., 2003; Hamaguchi et al., 2004; Künnapuu et al., 2014). The Dorsal gradient further refines Dpp activity by promoting the ventrolateral expression of *Short gastrulation* (*sog*), which modulates the localization of heterodimers of Dpp and Screw (Scw) – the most active Dpp signaling complex (Ashe et al., 2000). Sog and Twisted gastrulation (Tsg) bind Dpp/Scw heterodimers, preventing them from binding their receptor in ventrolateral regions and transporting them dorsalward via the net diffusive flux of Sog (Nguyen et al., 1998; Dorfman and Shilo, 2001; Mizutani et al., 2005). Active Dpp/Scw heterodimers are then released near the dorsal midline when bound Sog is cleaved by Tolloid (tld) (Decotto and Ferguson, 2001; Shimmi et al., 2005; Canty et al., 2006). Sog may also help establish the dorsoventral Dpp gradient by protecting Dpp from degradation (Decotto and Ferguson, 2001; Mizutani et al., 2005).

The Dorsal and Dpp gradients are integral to amnioserosa specification through their effects on the expression domain of *zen.* Dorsal antagonizes *zen* transcription in all but the dorsalmost domain (Lynch et al., 2012). This initially broad expression of *zen* is then coordinately localized with Dpp to a narrow dorsal stripe (~ 6 cells wide, Fig. 2-3©) defining the presumptive amnioserosa (Créton et al., 2000; Rushlow et al., 2001; Schmidt-Ott et al., 2010). The mutual refinement of Dpp and Zen patterns depends on Zen-driven expression of Egr and Cv-2, which respectively promote and inhibit Dpp signaling (Arora and Nusslein-Volhard, 1992; Morisalo and Anderson, 1995; Schmidt-Ott et al., 2010; Gavin-Smyth et al., 2013). This Zen/Dpp system is thought to canalize amnioserosa specification, buffering against environmental and genetic perturbations (Gavin-Smyth et al., 2013; Panfilio and Roth, 2013).

Germband Extension (Bownes Stages 7-9, 4-6 hours pre-DC)

From its initially specified dorsal domain, the amnioserosa changes shape dramatically during germband extension. Its cells become extremely elongated and stretch over large regions of the embryo's lateral flanks; the attached germband concurrently elongates and wraps around onto the embryo's dorsal surface (Fig. 2-4). These movements may be triggered by forces from mesoderm invagination and by cytoplasmic connections with the yolk sac that pull posterior pole cells onto the dorsal side, followed closely by the extending germband (Rickoll, 1976; Rickoll and Counce, 1980; Butler et al., 2009). Extension of both the amnioserosa and germband takes about two hours, divided into a fast phase (~ 30 minutes) and a second slower phase (~ 90 minutes) (Hartenstein and Campos-Ortega, 1985; Harris et al., 2009). Both extensions involve active processes: convergent extension via cell neighbor exchanges in the germband (Keller et al., 2000; Tada and Heisenberg, 2012) and rotary cell elongation in the amnioserosa (Pope and Harris, 2008). Cells in the germband also change shape, but this contributes only about one third of the initial fast extension rate (Butler et al., 2009).

These cell rearrangements are driven by pair-rule-regulated differences in adhesion and tension along dorsoventral and anterior-posterior cell edges (Irvine and Wieschaus, 1994; Rauzi et al., 2010; Levayer and Lecuit, 2013), reflected in anisotropic distributions of Bazooka and myosin II (Fig. 2-4(B), circle inset) (Zallen and Wieschaus, 2004; Harris et al., 2009; Goldenberg and Harris, 2013). This cellular anisotropy is an example of planar cell polarity (Bertet et al., 2004; Fernandez-Gonzalez and Zallen, 2009; Rauzi et al., 2010; Levayer and Lecuit, 2013) and is regulated by multiple factors including Toll receptors (Paré et al., 2014) and serotonin signaling (Colas et al., 1999a; Colas et al., 1999b; Schaerlinger et al., 2007).

Rather than exchanging neighbors, individual amnioserosa cells actively elongate (Fig. 2-4, circle insets) (Pope and Harris, 2008), initially in a dorsal-ventral direction and later switching to anterior-
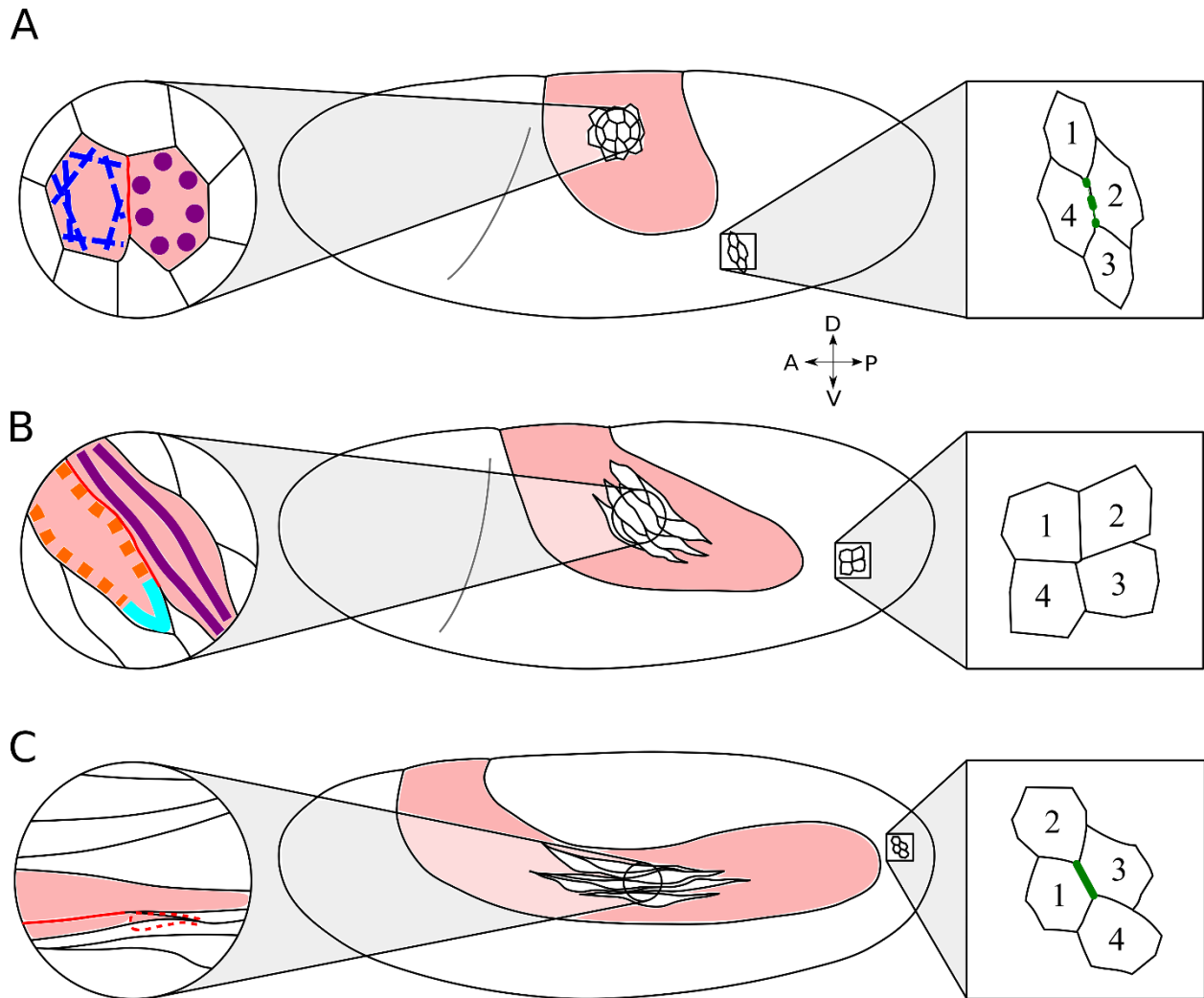
Figure 2-4. Germband extension. Lateral view with embryonic axes as indicated (A=anterior, P=posterior, D=dorsal, V=ventral). Amnioserosa is marked in pink throughout. (A) Early germband extension. Circle inset magnifies cells beginning to extend; two neighboring cells are identified as 1 and 2. The cortical actin network of cell 1 is marked in dashed blue lines; microtubule cross-sections in cell 2 are marked in purple. Square inset shows a group of germband cells beginning a four-cell T1 neighbor exchange, with cells 2 and 4 in contact. (B) Mid-germband extension. Circle inset shows that elongating amnioserosa cells 1 and 2 remain in contact. Edges of cell 1 show the relative localization of non-muscle myosin II (orange) and Bazooka (blue). Microtubules in cell 2 are marked in purple and have now rotated to extend in the direction of cell elongation. Square inset shows germband cells 1-4 in the intermediate phase of a T1 exchange. (C) Late germband extension. Circle inset shows fully elongated amnioserosa cells with characteristically thin, elongated tips. Cells 1 and 2 remain in contact with one another. Square inset shows the completion of a T1 neighbor exchange in the germband, with cells 1 and 3 now in contact.

posterior (Fig. 2-4(A-B)). As these cells elongate, they also change from columnar to a more flattened

squamous shape. This directional elongation and flattening has been referred to as rotary cell

elongation, so called due to the movement of microtubule bundles spaced around the cell perimeter

that are initially oriented apicobasally (cross-sections in Fig. 2-4(A), circle inset), but then elongate and

16

rotate until their previously apical ends point ventrally (Fig. 2-4(B), circle inset) (Pope and Harris, 2008).

This process is aided by cortical networks of actin and non-muscle myosin II that restrain and redirect the

elongating microtubules (Fig. 2-4(A), circle inset). If the cortical actin network is weakened in

amnioserosa cells, elongating microtubules cause sharp apical protrusions without rotation (Pope and

Harris, 2008). Interestingly, weakening cortical actin in the germband causes those cells to elongate in a

manner similar to normal amnioserosa cells, suggesting that rotary cell elongation can be suppressed by

cortical actin that is either too weak or too strong (Pope and Harris, 2008).

Amnioserosa cell elongation also requires adherens junctions to adapt to the continually

changing length of cell-cell interfaces – some lengthening, some shortening – by delivery of new

adherens junction proteins or by lateral redistribution and endocytic and exocytic turnover of existing

proteins (Goldenberg and Harris, 2013). For anterior-posterior cell edges, these processes are insufficient

to compensate for elongation, resulting in a lower cadherin abundance per unit membrane length. For

dorsal-ventral edges, no compensation is necessary because these edges do not change length.

Nonetheless, their adherens junctions still undergo constant turnover, possibly because rotating

microtubules apply force to the ventral "front" edges. As in the germband, amnioserosa cells have

anisotropic protein distributions with more Bazooka along dorsal-ventral edges and more myosin II along

anterior-posterior edges (Fig. 2-4(B), circle inset) (Zallen and Wieschaus, 2004; Harris et al., 2009;

Goldenberg and Harris, 2013). This anisotropy is consistent with a model in which dorsal-ventral contacts

are remodeled due to microtubule rotation and enhanced myosin is needed along anterior-posterior

contacts to limit microtubule extension (Pope and Harris, 2008).

Once rotary cell elongation is complete, amnioserosa cells are roughly ten times their initial

length and about one-fifth their original diameter (Fig. 2-4, circle insets) (Pope and Harris, 2008). This

dramatic cell reshaping accounts for all of the amnioserosa's tissue elongation. By the end of germband

extension, the amnioserosa has lengthened from a dorsal ovoid to a U-shape with its base across the

dorsal surface and its arms extending posteriorly along the embryo's lateral flanks. The amnioserosa's arms fill the space between the dorsal and ventral regions of the similarly U-shaped germband, whose caudal tip has curled around the posterior end of the embryo and onto the mid-dorsal surface (final position shown in Fig. 2-4(C)) (Irvine and Wieschaus, 1994).

Germband Retraction (Bownes Stage 12, 0-2 hours pre-DC)

Over the course of about two hours, segments of the extended germband contract along the rostral-caudal axis and elongate toward the amnioserosa, shortening the entire tissue in a process known as germband retraction (Fig. 2-5) (Schöck and Perrimon, 2002; Lynch et al., 2013). This process is not the reverse of germband extension; instead of de-intercalating, germband cells now elongate parallel to their respective segments (Fig. 2-5, square insets) (Schöck and Perrimon, 2002). Amnioserosa cells concurrently shorten to eventually become squamous, roughly isodiametric, and hexagonal (Fig. 2-5(C), circle inset) (Schöck and Perrimon, 2002; Pope and Harris, 2008), retracting the amnioserosal flanks anteriorly and dorsally. By the end of retraction, the amnioserosa occupies an ovoid region of the dorsal surface and the germband covers the ventral and lateral surfaces, with its caudal end at the posterior of the embryo (Fig. 2-5(C), almost fully retracted).

The amnioserosa plays a key role in this process and germband retraction fails when the amnioserosa's epithelial integrity is compromised. For example, retraction fails in mutants of the u-shaped group – u-shaped (*ush*), hindsight (*hnt*), serpent (*srp*), and tail-up (*tup*) – mostly due to premature amnioserosa apoptosis (Frank and Rushlow, 1996). The notable exceptions are *tup* mutants in which the amnioserosa is reduced, but does not prematurely apoptose (Frank and Rushlow, 1996), and *hnt* mutants in which retraction fails even when apoptosis is suppressed by other means (Yip et al., 1997; Lamka and Lipshitz, 1999). Both suggest additional roles for these regulators. Nonetheless, similar failures occur when amnioserosa cell maintenance and/or its monolayer epithelial structure are
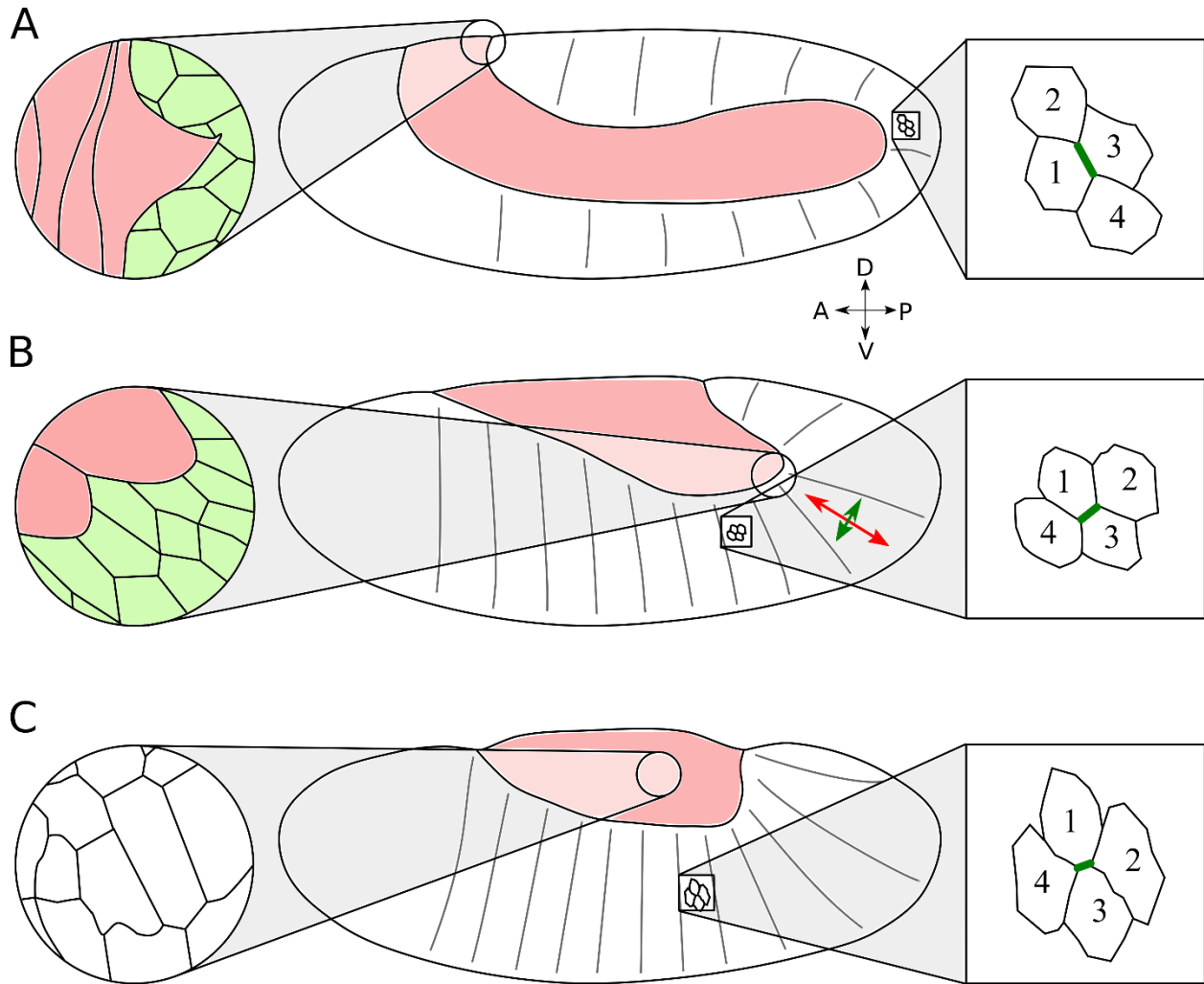
Figure 2-5. Germband retraction. Lateral view with embryonic axes as indicated (A=anterior, P=posterior, D=dorsal, V=ventral). Amnioserosa is marked in pink throughout. (A) Onset of germband retraction. Circle inset shows dorsal view of a crawling lamellipodium at the interface between amnioserosa and germband. Square inset shows a group of cells in the extended germband, with cells 1 and 3 in contact. (B) Mid-germband retraction. Crossed double-headed arrows represent tensile stress anisotropy in one segment in the crook of the germband; largest principal stress is towards the amnioserosa. Circle inset shows interface between amnioserosa and germband at the posterior crook of the germband; the amnioserosa-germband interface is concave at junctions between amnioserosa cells, indicative of a pulling force from the amnioserosa. Square inset shows retracting germband cells, maintaining contact between cells 1 and 3. (C) Late germband retraction. Circle inset shows roughly isodiametric amnioserosa cells. Square inset shows germband cells slightly elongated in the direction of the amnioserosa. Cells 1 and 3 remain in contact, showing that retraction has occurred without cell intercalation.

compromised by disruption of ecdysone signaling (Kozlova and Thummel, 2003) or laminin-integrin interactions (Stark et al., 1997; Schöck and Perrimon, 2003). Finally, retraction defects are observed when epithelial integrity of the amnioserosa is disrupted by laser ablation (Lynch et al., 2013) or by non-specific environmental perturbations like hyperthermia (Eberlein, 1986). Interestingly, hyperthermia

leads to retraction defects when the heat shock is applied early in embryogenesis (at gastrulation) and

holes open in the amnioserosa several hours later (Crews et al., 2015). These examples demonstrate that

the mechanisms of germband retraction rely on the germband and amnioserosa as two contiguous,

coordinated epithelia.

Through this contiguity, the amnioserosa exerts key forces on the germband. At the onset of

retraction, the amnioserosa's dorsal bridge – the thin dorsal portion connecting its lateral flanks –

overlaps the caudal end of the germband. Loss of this overlap causes the amnioserosa to collapse below

the germband and results in incomplete retraction (Schöck and Perrimon, 2003). The overlap decreases

as retraction progresses, but the posteriormost bridge cells extend lamellipodia to maintain contact with

and crawl posteriorly over the caudal germband (Fig. 2-5(A), circle inset) (Schöck and Perrimon, 2002).

This crawling is reduced in integrin or laminin mutants, and is disrupted even more strongly in integrin-

laminin double mutants, establishing an important role in retraction for integrin-laminin-mediated forces

(Schöck and Perrimon, 2003).

The amnioserosa also exerts force along the lateral edges of the germband. Close inspection of

segments in the posterior crook of the germband (segments A4-A7) reveals an amnioserosa-germband

interface here that is concave at amnioserosa cell junctions (Fig. 2-5(B), circle inset), indicating a pulling

force from the amnioserosa (Schöck and Perrimon, 2002). This pulling force has been further explored by

laser-wounding experiments in which linear incisions in different germband segments opened with

different aspect ratios dependent upon the incision direction and the segment-specific balance of

anisotropic forces (Lynch et al., 2013). Such experiments demonstrated strong force anisotropy

specifically in segments around the crook of the germband, consistent with an external tensile stress

exerted on these segments by the amnioserosa (Lynch et al., 2013). Computer modeling of these results

shows that the germband must have its own internal anisotropic forces that counteract those from the

amnioserosa and limit germband cell elongation (Lynch et al., 2014). An example of these counteracting

anisotropic forces is shown schematically in Fig. 2-5(B) for a single segment in the crook. In the absence of amnioserosa forces, germband cells still elongate during this stage of development, but their elongation can be misdirected without the proper balance of germband and amnioserosa forces (Lynch et al., 2013).

By the end of retraction, the proper combination of forces brings the amnioserosa and germband into their appropriate dorsal and lateral positions for the commencement of dorsal closure. The stage has been set.

Evolution

Despite the amnioserosa's critical role in *Drosophila* embryogenesis during germband extension, retraction, and dorsal closure – all morphogenetic stages that are common among insects – the amnioserosa itself is an anomaly. Most insect orders develop two extraembryonic tissues, amnion and serosa, which separate from each other early in development (Panfilio, 2008; Schmidt-Ott et al., 2010); the serosa surrounds the embryo, while the amnion remains contiguous with the embryonic epithelium. The single fused amnioserosa is known to occur only in *Drosophila* and some of its cyclorrhaphan relatives (Panfilio, 2008; Rafiqi et al., 2008). Current research places the divergence corresponding to the evolutionary origin of a fused amnioserosa between 80 and 145 million years ago (Rafiqi et al., 2010; Hodar et al., 2014).

Figure 2-6 compares extraembryonic development in *Drosophila* and its close relative, the scuttle fly *Megaselia abdita*, which provides an example of development with separate amnion and serosa (Wotton et al., 2014). Although somewhat unusual in lacking an amniotic cavity (Schmidt-Ott, 2000; Horn et al., 2015), *Megaselia* is useful here to highlight *Drosophila*'s essential points of departure. The two insects have similar, narrow dorsal stripes of *zen* expression by late blastoderm stages, but *Megaselia* skips any initial broad *zen* expression pattern and uses its narrow *zen* stripe to specify just its

serosa (Fig. 2-6(A)); its amnion is *zen*-negative (Falciani et al., 1996; Rafiqi et al., 2008; Rafiqi et al., 2010; Schmidt-Ott et al., 2010). The two developmental paths diverge further during germband extension when *Megaselia*'s amnion and serosa separate (Fig. 2-6(B)). The serosa subsequently expands and by the beginning of germband retraction, it surrounds the entire embryo (Fig. 2-6(C)) (Falciani et al., 1996; Rafiqi et al., 2008; Schmidt-Ott et al., 2010). The amnion, meanwhile, bears morphological similarity to *Drosophila*'s amnioserosa throughout germband extension and retraction (Fig. 2-6(B-D)) (Panfilio, 2008; Rafiqi et al., 2008; Rafiqi et al., 2010; Wotton et al., 2014). As dorsal closure commences, *Megaselia*'s surrounding serosa ruptures and retracts around both ends of the embryo to join the amnion on the dorsal surface as both tissues invaginate – very similar to the amnioserosa's behavior in *Drosophila* dorsal closure (Fig. 2-6(D-E)) (Rafiqi et al., 2012; Wotton et al., 2014).

With the central role of *zen* in specifying extraembryonic tissues for a wide range of insects (Falciani et al., 1996; van der Zee et al., 2005; Lynch et al., 2012; Heffer and Pick, 2013; Sharma et al., 2013), *zen* is strongly implicated in the evolutionary origin of the single amnioserosa (Rafiqi et al., 2010; Hodar et al., 2014). In *Drosophila*, the key differences from insects that form a distinct amnion and serosa appear to be earlier expression of a wide and shallow *zen* gradient that then narrows to a dorsal stripe with greater posterior extent, overlapping the region in which *zen*-negative amnion forms in other insects (Fig. 2-6(A), compare posterior extension of pink strip in *Drosophila* to orange area in *Megaselia*). These differences may have inhibited amnion formation and thus encouraged the formation of a more serosa-like tissue (Rafiqi et al., 2008; Rafiqi et al., 2010; Schmidt-Ott et al., 2010). The *Drosophila* amnioserosa does not, however, remain serosa-like. It stops expressing *zen* during gastrulation, unlike the continuously *zen*-positive serosa (Rafiqi et al., 2010), and subsequently takes on an amnion-like morphology. Instead of having spatially segregated *zen*-negative and *zen*-positive extraembryonic tissues, *Drosophila*'s single amnioserosa switches from *zen*-positive to *zen*-negative temporally
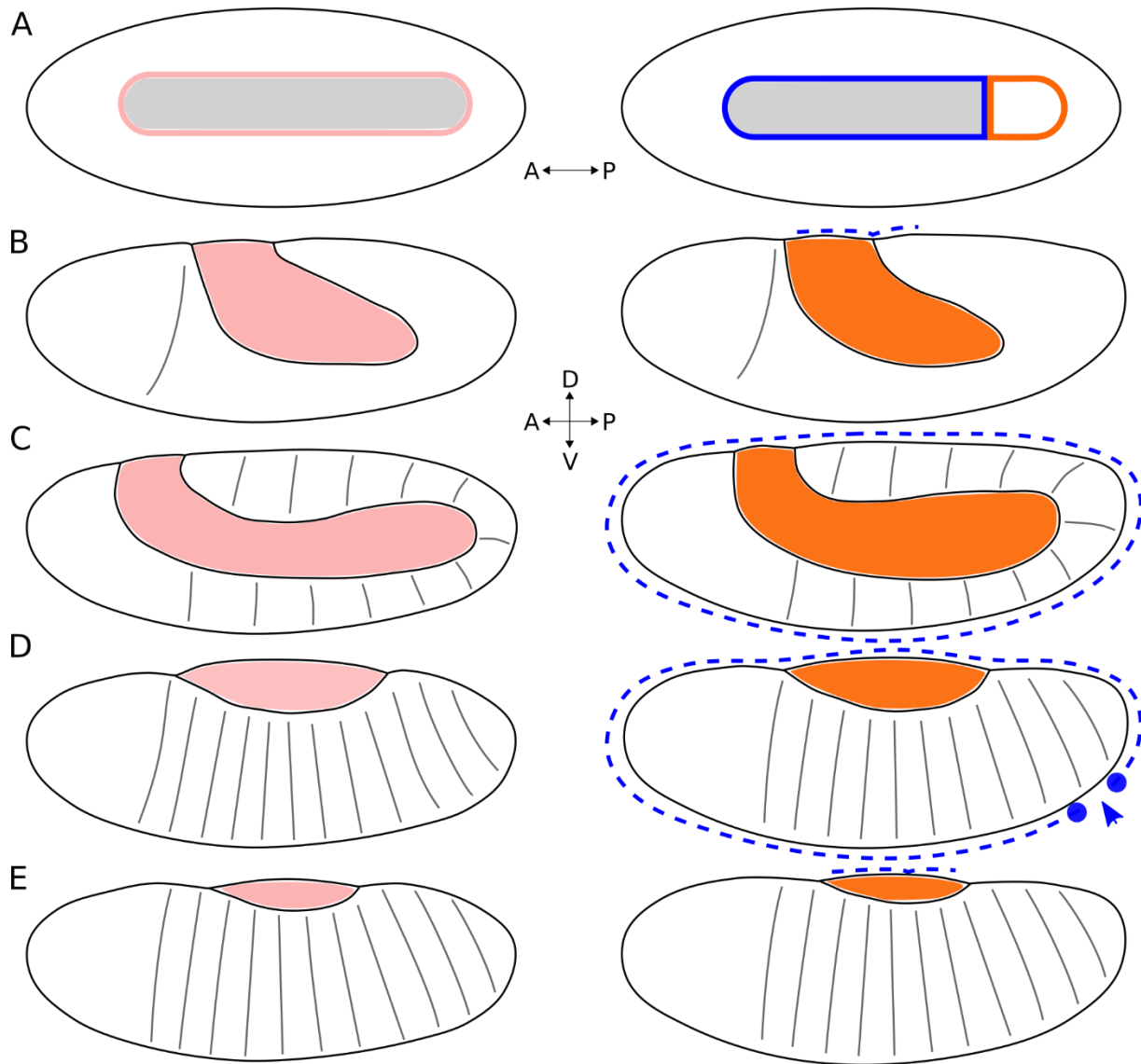
Figure 2-6. Key stages at which amnioserosa morphology differs from amnion and serosa morphology in *Megaselia abdita*. Dorsal view in (A) and lateral views in (B-E) with embryonic axes as indicated (A=anterior, P=posterior, D=dorsal, V=ventral). Amnioserosa is highlighted in pink, amnion in orange, and serosa in blue throughout. (A) Late blastoderm *zen* expression (gray) in *Drosophila* (left) and *Megaselia* (right). Solid outlines represent presumptive amnioserosa or presumptive amnion and serosa. (B) Early germband extension. *Megaselia*'s serosa (dashed blue line) begins to expand from its point of division from the amnion. (C) Onset of germband retraction. The serosa completely surrounds a *Megaselia* embryo, but is absent in *Drosophila*. (D) Early dorsal closure. *Megaselia's* serosa ruptures at the posterior end (blue arrow marks gap, blue circles mark serosa endpoints). (E) Late dorsal closure. *Megaselia's* serosa retracts completely and is internalized with the amnion by the end of dorsal closure.

(Schmidt-Ott et al., 2010). Further understanding of the phylogeny and origins of the amnioserosa

should shed light on the evolution of signaling pathways and morphogenesis of extraembryonic tissues.

Conclusions and Future Directions

The amnioserosa represents a departure from the common course of extraembryonic development in insects, arising from a fusion of the ancestral serosa and amnion to play multiple essential morphogenetic roles. Throughout embryogenesis, the amnioserosa's dramatic changes in cell and tissue shape offer challenges and opportunities for biophysical studies. For example, during germband extension, the elongation of amnioserosa cells requires rotation and extension of microtubule bundles, a proper range of stiffness in the cortical actomyosin network, and turnover and redistribution of adherens junctions. We have some quantitative data on the rates of microtubule extension (Pope and Harris, 2008) and adherens junction redistribution (Goldenberg and Harris, 2013), but our understanding of the interplay of these dynamic structures is at present qualitative. There are multiple opportunities to measure these interactions experimentally and explore their coordination computationally. In addition, during germband retraction, the amnioserosa exerts external anisotropic forces on the germband, and germband cells have their own internal anisotropic tensions, but these forces are still not fully understood. Models to date can place limits on how these internal and external forces are related (Lynch et al., 2014), but better measurements are needed to quantitatively map both. These open questions are in addition to those remaining in the well-studied process of dorsal closure, which still stands as an excellent model for midline fusion, a common process in many developmental events in both vertebrates and invertebrates (Ray and Niswander, 2012). In all of the above, there are additional interesting questions about morphogenetic robustness and contingency in the face of genetic and environmental perturbations – *i.e.*, understanding how and to what extent morphogenetic mechanics can adapt to perturbations of earlier events.

The same features that have made *Drosophila* convenient as a model organism will continue to make the amnioserosa an attractive model tissue. Recent investigations of the amnioserosa as an active contributor to *Drosophila* embryogenesis have laid the groundwork, but there is ample scope for future

work, with numerous unanswered questions about amnioserosa mechanics and its role in several major movements of morphogenesis. Future studies of the amnioserosa will shed light on parallels to morphogenesis in other tissues and organisms, and usher in new challenges in biophysics and cellular mechanics.

Acknowledgments

CHAPTER 3

Experimental Methods in *Drosophila* Research

This chapter is included as an introduction to some of the most important aspects of the experimental research described in this dissertation, both in Chapter 4 and in the appendices that follow the main text. The selected methods here deal with a diverse range of topics that have been of particular significance for my research, including constructing genetic crosses, best practices for imaging and ablation, and modeling anisotropic forces in cell sheets. To understand the research presented in Chapter 4, it is especially useful to refer to the later section on Force Anisotropy and Parameter Space, which provides a background in previous research, and Cellular Force Inference Methods, which gives an overview of recent reverse-modeling methods of inferring forces from live images.

Drosophila Care and Breeding

Among the advantages of *Drosophila* is its simple care regimen. One stock (genetic line) can be kept for several weeks in a plastic vial, feeding on a solidified paste of brown sugar and yeast, and transferred to a fresh vial once the new generation of adults begins to emerge to provide fresh egg-laying potential. For straightforward imaging needs, useful *Drosophila* stocks can be obtained from stock centers and kept unchanged for generations, but for some applications it is necessary to breed specific genetic lines to produce the desired phenotype.

Setting up a breeding scheme, or cross, involves careful observation and identification of traits like sex and characteristic mutations. Adult *Drosophila* sex is easily identified; females are larger than males and have dark dorsal abdominal stripes, and males have dark dorsal abdomens and visible bristle combs on their front forelegs. In addition to separating females and males, it is critical to identify virgin females, which have eclosed within the last 8-10 hours. These newly emerged females are larger and paler than older females, and their ventral abdomens show a dark spot called the meconium, the

26

remnant of the larva's last meal. Selecting these females ensures that they have not been fertilized by males of their own genotype; this is generally done by transferring adults to a new vial before the pupae begin to eclose, to guarantee that any adults found in the old vial are newly eclosed.

Selecting the right offspring in each generation is made possible by mutant phenotypes, which are often present in adult flies due to balancer chromosomes. Balancer mutations are inserted in the second copy of the chromosome containing the mutation of interest, so that either their presence or absence indicates the correct flies. Common balancer traits include eye color, wing shape, and bristle length; for complex crosses, flies with the desired genotype may display multiple balancer phenotypes from different chromosomes, limited only by the fact that *Drosophila* have only four pairs of chromosomes. When collecting flies from two strains, only females should be collected from one and only males from the other; the chromosomal locations of the genes of interest may dictate which sex to assign to each strain.

The GAL4/UAS System

One genetic tool of particular use for obtaining flies with specific and localized traits is the GAL4/UAS system. GAL4 is a sequence in the *Saccharomyces cerevisiae* (yeast) genome that codes for a protein that binds to an Upstream Activating Sequences (UAS) element, a region that is necessary for transcription of a particular downstream gene. GAL4 drivers are created by inserting the GAL4 sequence downstream of an existing activator sequence, which transcribes GAL4 only in a particular pattern that targets a specific tissue and/or developmental stage. A *Drosophila* strain with the desired Gal4 protein expression is then crossed with a second strain containing a UAS element tied to the gene of interest. As illustrated in Fig. 3-1, when the two strains are mated, some of the offspring will contain one copy of the GAL4 drive and one copy of the UAS element, so that the gene is transcribed according to the pattern of Gal4 expression (Duffy, 2002).
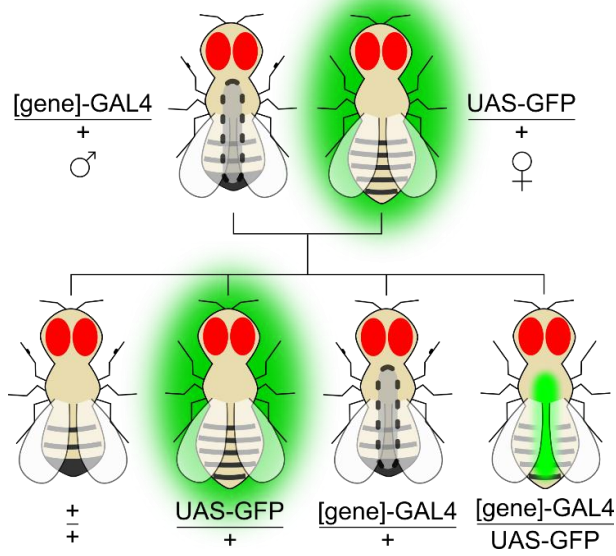
Fig. 3-1. Illustration of the GAL4-UAS system. Some of the offspring of a GAL4xUAS cross will contain both the GAL4 and UAS sequences, resulting in the desired trait expressed in the desired region (shown in the last of four offspring here).

Imaging

Imaging specimens for biophysics research presents several challenges. Structures at the tissue and cellular level must be clearly visible, and for live imaging, we must be able to sustain imaging over time, capture events occurring on short timescales, and often probe the mechanics of the system rather than merely observing. Confocal imaging (basic schematic shown in Fig. 3-2) is a good choice for clarity, longevity, and speed, since it eliminates much of the out-of-plane noise and allows continuous imaging of *in vivo* development, with exposure times as low as 100 ms for a spinning disk confocal microscope.

For live imaging, careful orientation is essential for good image quality, especially when imaging over the course of several hours and multiple developmental phases. Accordingly, the specimens used in the research presented here were oriented to present lateral or dorsal views, to best accommodate possible changes in the location of the tissues of interest. Another factor to consider is photobleaching, which dims the resulting images; this is inevitable over time, but imaging protocols can minimize photobleaching by regulating imaging frequency and resolution.
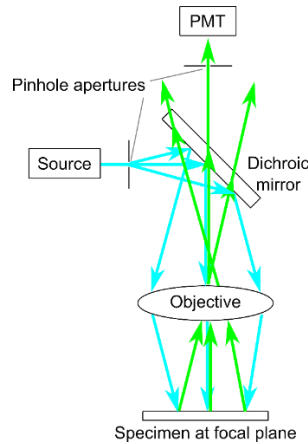
Fig. 3-2. Basic schematic of a confocal microscope. The source illumination (blue) passes through the same objective as the reflected light (green), allowing a tighter focus on a thinner plane and cutting down on light pollution from other planes of the specimen.

For ablation purposes, the laser-scanning confocal microscope used for this research is coupled with targeted pulses from the third harmonic of a 5-ns pulse width Q-switched Nd:YAG laser (355 nm; Continuum Minilite II, Santa Clara, CA). Ablation involves both calibrating the targeting system to accuracy within a few pixels on a 512x512 image and adjusting the laser energy to an appropriate level. In most cases, the goal of ablation is not to cause widespread tissue damage but to precisely sever a single cell edge or series of edges at a specific point. For this purpose, the laser can be controlled by opening and closing the shutter for a set amount of time or by changing Q-switch modes so that the laser pulses only for a short period of time. The targeting system can also draw lines at various speeds in addition to targeting single points.

Seedwater Segmenter

The paramount need in image processing for cell-level biophysics research is the clear and accurate delineation of cell boundaries. The changes in cell size, location, and contacts that occur over time give critical information about their behavior in development and their reactions to stimuli. To capture clear images of cell edges, fluorescent tags are generally used with proteins that are recruited to cell-cell interfaces, most often E-cadherin. After imaging, the cell borders are traced using Seedwater

Segmenter, a program developed by David Mashburn around a watershed algorithm, which identifies

the centroids and boundaries of each cell by treating the darkest areas in an image as basins and filling

them until the basins meet at cell edges (Mashburn et al., 2012). Seedwater is most useful for drawing

cell boundaries because of the combination of this watershed method with extensive user control,

enabling redrawing and moving of boundaries as necessary to correct wrong assignments thrown off by

noisy images and unclear cell edges.

In addition to identifying cell boundaries, Seedwater can output and save a set of calculations of

individual cell area, perimeter, vertex position, and other information about the segmented cells. This

information is used heavily for beta-theta analysis, providing the cellular Voronoi diagram for angle

analysis through a Python program that generates CVDs from Seedwater's logs. Figure 3-3 shows an

example of Seedwater cell identification along with the resulting CVD. Seedwater also provides the

centroid-based measurements that are used to find the moment of inertia tensors for the cell aspect

ratios used in the extended analysis.
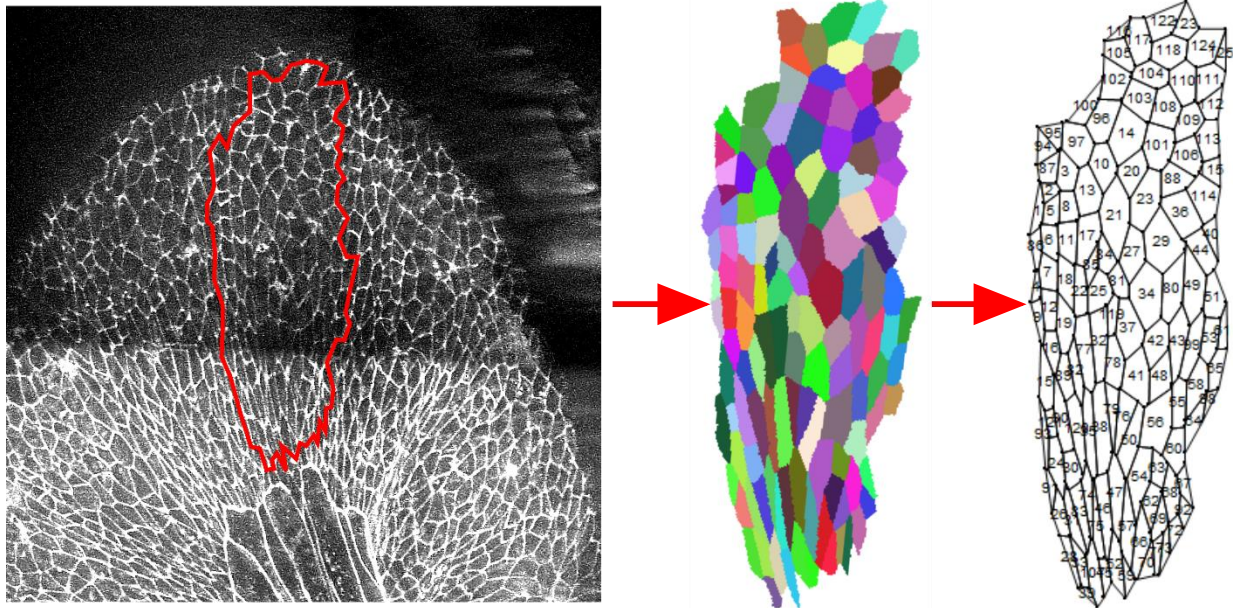
Fig. 3-3. Visualization of Seedwater Segmenter output. Confocal image of germband retraction embryo, center, with segment A5 marked with red rectangle. Color map of segmentation from Seedwater Segmenter at left, cellular Voronoi diagram produced in Mathematica from Seedwater Segmenter output at right.

Finite Element Modeling

Although this work is not directly concerned with the more in-depth modeling of *Drosophila* embryogenesis that has been done in recent years, the beta-theta analysis discussed in Chapter 4 uses previous results from simulations following current epithelial tissue models (Lynch et al., 2014). Because of this foundation and the potential of beta-theta analysis for internal tension inference, it is appropriate here to briefly discuss the background of epithelial finite element modeling and related force inference methods.

In studying embryogenesis at the cell and tissue level, we deal with the germband and the amnioserosa, both of which are single cell layers. It is thus possible to treat both epithelia as cell sheets that can be modeled with finite element principles. Finite element modeling divides the cell sheet into polygons that often represent individual cells, but can represent larger areas with accurate results for bulk tissue changes and properties (Brodland et al., 2006). Earlier finite element epithelial modeling treated the cell as a set of triangles, one for each cell edge. The outer sides of the triangles were cell edges that carried tensions dependent on the edge direction and tissue properties, and the triangles pointed inward to meet at a node inside the cell as well as at the outer vertices (Brodland et al., 2006). However, more recent work suggests that a more accurate model involves orthogonal sets of internal dashpots the strength of which depends on both direction and uniform viscosity μ (see Fig. 3-4 for a depiction of triangular elements and orthogonal dashpots) (Brodland et al., 2007). The edges continue to carry a direction-dependent tension γ.

Epithelial tissue varies in its mechanical properties according to many factors, including viscosity, cell shape, and the presence of elements such as the extracellular matrix (ECM), which can limit reorganization or intercalation in response to tissue strain (Brodland and Wiebe, 2004). All of these factors can change during the course of development; for example, the germband cells intercalate

extensively during germband extension but not during retraction a few hours later (Schöck and

Perrimon, 2002). Analysis of the germband's response to cell-edge ablations during retraction suggests

that it has viscoelastic responses to stimuli that are characteristic of both solids and liquids, with an

initial elastic response and a later viscous phase. In mathematical terms, this can be represented by a

choice or combination of the Maxwell model (for viscoelastic liquids) and the Kelvin-Voigt model (for

viscoelastic solids). The Kelvin-Voigt model puts a spring and dashpot in parallel so that deformation can

be completely reversed because of the spring; the Maxwell model uses the same elements, but in series

so that deformation is not completely reversible. Previous work has suggested that adding viscoelastic

trusses to the cell edges can reproduce the basic characteristics of the germband's wounding responses;

Hutson et al. combined the two models in parallel (Hutson et al., 2009), but Lynch et al. chose to use

Kelvin-Voigt elements alone as edge trusses (Fig. 3-4 inset) (Lynch et al., 2014).
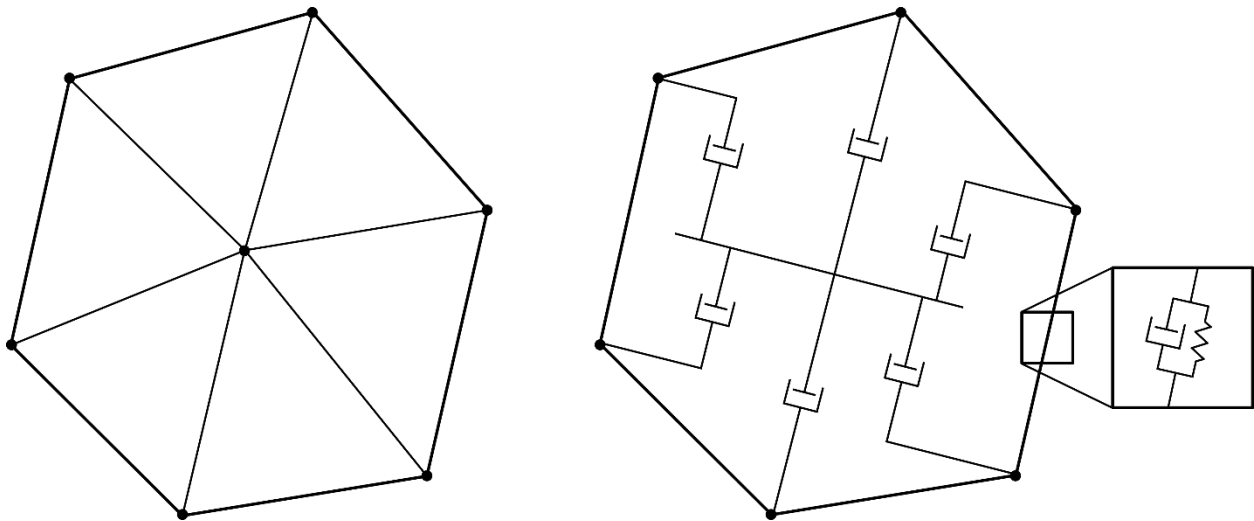
Fig. 3-4. Finite element representations of a single cell. The triangle formulation treats all cell edges as the outward-facing edges of triangles that meet inside the cell at a central node; the outer edges carry interfacial tensions, and previous work tested the accuracy of placing dashpots along all the rod elements linking the nodes. A more accurate model instead uses sets of orthogonal dashpots (only one axis is shown here for simplicity) and outer interfacial tensions. The inset focuses on one of these cell edges, showing the Kelvin-Voigt element that serves as a viscoelastic truss along each cell edge.

Force Anisotropy and Parameter Space

In using a finite-element cell sheet to model the reactions of germband segments to laser

wounding, Lynch et al. divided the forces acting on the sheet into external stresses, applied at the edges

of the cell sheet by the amnioserosa or by neighboring germband segments, and internal tensions,

carried by the cell edges within the sheet. The internal edge tension for any given edge is represented by

γ; the anisotropy of the average edge tension $\bar{\gamma}$ is quantified in the simulations by the anisotropy (or

polarization) parameter f, defined so that

$$\gamma = \bar{\gamma}(1 - \frac{f}{2}\cos[2(\beta - \beta_o)]),\tag{3-1}$$

where β is the edge orientation and β_o is the direction of minimum edge tension. The average external

stress $\bar{\sigma}$ is also assumed to be anisotropic, with directional components $\sigma_1 = \bar{\sigma} + \Delta$ and $\sigma_2 = \bar{\sigma} - \Delta$ that

allow the stress anisotropy parameter $\frac{\Delta}{\bar{\sigma}}$ to be defined as

$$\frac{\Delta}{\bar{\sigma}} = \frac{\sigma_1 - \sigma_2}{\sigma_1 + \sigma_2}.\tag{3-2}$$

The possible combinations of internal and external anisotropies were visualized by plotting them as

coordinate pairs in a parameter space. These parameter pairs were used to run simulations mimicking

actual experiments in which linear wounds were opened parallel or perpendicular to the direction of cell

elongation (Lynch et al., 2013). The resulting simulated cell and wound aspect ratios (referred to as κ_{cells},

$\kappa_{w,As}$, and $\kappa_{w,RC}$) were plotted as contours in the parameter space; the *in vivo* wound data was then

matched to the parameter points that corresponded to the most accurate combination of wound and

cell aspect ratios (Lynch et al., 2014).

This method offered several possible best-fit options based on the specific aspect ratios for each

segment, but there was no way to narrow down the possible values to a single set. The fits suffered

from a lack of specific information about the cell aspect ratio of individual segments, instead using

κ_{cells}≈1.33 for all segments. Moreover, these fits were based on observation at one point in retraction

(<R>=36+/30% GBR), and the changing conditions of the germband throughout retraction made it

unlikely that these single data points would offer a fair picture of the germband's overall force

anisotropy (Lynch et al., 2013). Chapter 4 explains how beta-theta theory and analysis offer a solution to

the problem of multiple possible parameter fits, as well as expanding the available data well beyond

isolated snapshots of germband retraction.

Cellular Force Inference Methods

Before discussing the unique features of beta-theta analysis, it is useful to provide context for

this new method by discussing other current methods of force inference that have influenced or

inspired its development and can be used in similar situations. These methods, like beta-theta analysis,

have the benefit of being noninvasive in themselves, allowing observation of the forces at work in

normal development without perturbing or derailing the usual course of events. They may, of course,

also be combined with invasive methods like laser ablation and atomic force microscopy to investigate

responses to abnormal stimuli, but the benefits of noninterference are clear for understanding both the

tissue mechanics in general and their specific application in the stages under observation.

One of these methods is video force microscopy (VFM), which arose from the cell-based

constitutive finite element formulation developed by Brodland et al. (2006). The foundation of VFM is

the idea of mapping deformation in a finite element tissue by using a tensor to transform initial vectors

to final ones that reflect the overall changes in the material. In the initial presentation, these vectors and

the associated points corresponded to locations in the entire epithelial patch, rather than specific cell

edges or nodes (Brodland et al., 2006). In VFM, the idea of transformations is applied for the purposes of

inverse modeling, or inferring tissue properties from experimental images rather than trying to select

model parameters to match observed behavior (Brodland et al., 2010). A set of images is converted into finite element meshes by assigning polygons to individual cells, parts of cells, or groups of cells, depending on the shapes and deformations of the various parts of the tissue. For each time step *i* in the resulting set of images, a vector of node displacements $\dot{\boldsymbol{u}}_i$ is found, as well as a matrix $\boldsymbol{C}_i$ representing the geometry and viscosity of the tissue in step *i*. The global forces $\boldsymbol{f}_i$ at this step can then be found with

$$\boldsymbol{C}_i\dot{\boldsymbol{u}}_i = \boldsymbol{f}_i \qquad (3\text{-}3)$$

and separated into individual pressures and tensions by solving for the combined vector $\boldsymbol{T}_i$ in

$$\boldsymbol{G}_i\boldsymbol{T}_i = \boldsymbol{f}_i \,, \qquad (3\text{-}4)$$

where $\boldsymbol{G}_i$ is the combined tension and pressure geometric matrix. To improve solution stability and accuracy, this equation is considered in terms of previous and subsequent time steps as well, incorporating a weighted factor so that for *n* time steps,

$$\sum_{k=1}^{n}[\lambda_i^{|i-k|}\boldsymbol{G}_k\boldsymbol{T}_i] = \sum_{k=1}^{n}[\lambda_i^{|i-k|}\boldsymbol{f}_k] \qquad (3\text{-}5)$$

with $\lambda_i^{|i-k|}$ decaying for time steps farther from *i*. This method was used to map cell-edge tensions in *Drosophila* embryos during ventral furrow formation, with results that verify VFM's potential for analyzing the tensions and pressures underlying tissue deformation over time (Brodland et al., 2010). However, other applications have struggled with issues of noise sensitivity and instability in the original VFM methods, with improvements necessary to obtain consistent results.

One solution to the problems of VFM is offered by CellFIT (Cellular Force Inference Toolkit), which was developed from the same principles as VFM with a few crucial differences. For one, the finite element rendering of images allows curvilinear rather than straight cell edges (Brodland et al., 2014; Veldhuis et al., 2015). By adding nodes within cell edges and finding a best-fit radius of curvature, the angle of the edges coming into a triple junction can be reproduced more accurately. Another change is

that movement of the nodes is assumed to be slow enough that viscous forces are negligible and the system is in equilibrium. This allows the derivation of the relationship

$$\Delta p_{ij} = \frac{\gamma_{ij}}{\rho_{ij}} \tag{3-6}$$

where Δp_{ij} is the pressure difference at the interface between cells i and j, ρ_{ij} is the radius of curvature of the interface, and γ_{ij} is the tension along the interface. Equilibrium conditions also mean that the tension equation for each triple junction is

$$\sum \gamma_{mn} \hat{\boldsymbol{r}}_{\boldsymbol{mn,A}} = \boldsymbol{0} \tag{3-7}$$

where m and n are the cells interfacing at each cell edge coming into junction A. With adjacent junctions sharing the same tension from the connecting cell edge, a tissue sheet quickly accumulates more equations than unknowns, and some problematic edges and their associated triple junctions can be removed from calculations without jeopardizing the solutions (Brodland et al., 2014).

The process of solving for tissue parameters is simplified considerably by the fact that the node forces involve only the tensions, from which the pressures are calculated using Eqn. 3-6. This means that the pressure solutions are optional, for cases in which only the tension solutions are of interest. The tensions and pressures calculated by CellFIT are only relative values in the absence of a pair of actual tensions or pressures; by themselves, they should be considered as a general solution that reflects a wide array of possible sets of actual pressures and tensions, subject to scaling (Brodland et al., 2014).

The net effect of the changes from VFM to CellFIT is to allow the tension equations for a patch of cells to be solved more accurately and without the need for the time-weighted factors used in VFM (see a sample tension mesh in Fig. 3-5). Thus, CellFIT is applicable to single images and can provide useful solutions based only on edge tensions, assuming equilibrium conditions for all edges and nodes. These features are also part of beta-theta analysis, which owes much to CellFIT in this sense.
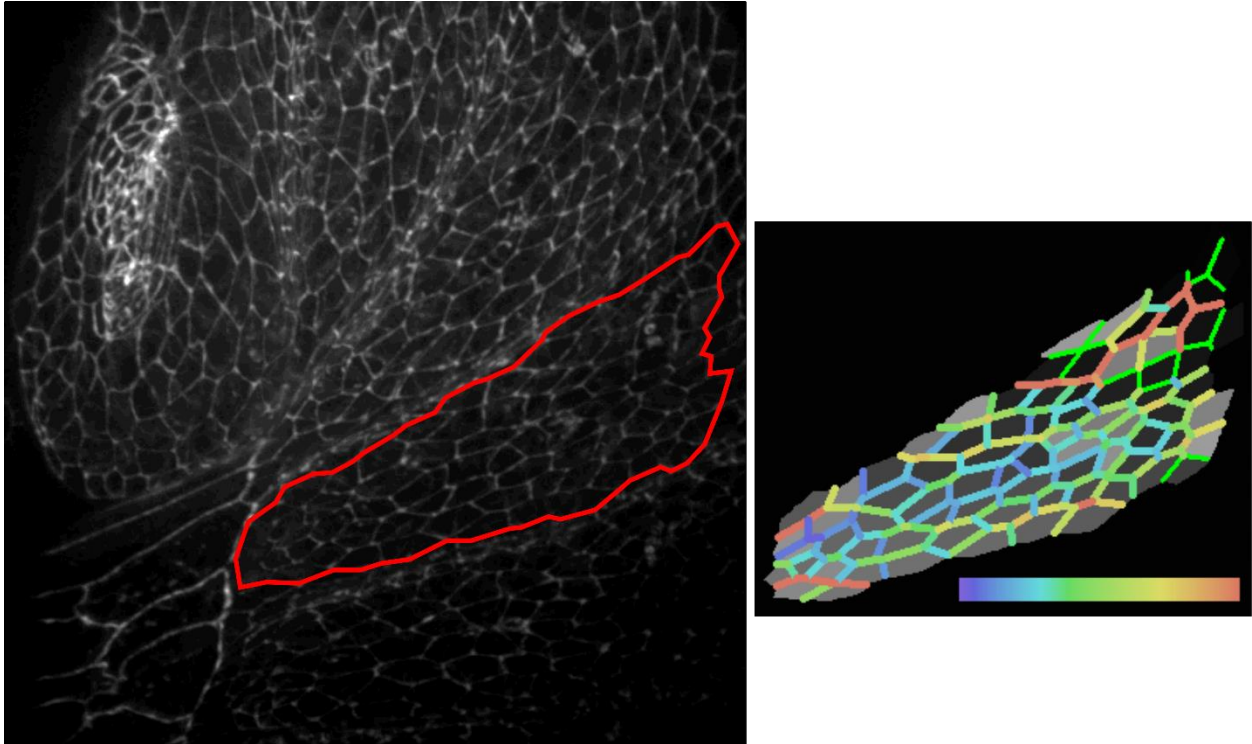
Fig. 3-5. Visualization of CellFIT edge-tension solutions. Confocal image with segment A5 marked in red. To the right is a CellFIT tension mesh for this segment, with 0 nodes along the cell edges to better match the cellular Voronoi diagrams used for beta-theta analysis.

Beta-theta analysis, like VFM and CellFIT, is a form of inverse modeling, and Chapter 4 presents an example of how it can complement existing forward modeling to obtain better solutions and deeper understanding of those solutions. One main difference between beta-theta analysis and the two force-inference methods discussed here is that while CellFIT and VFM both concentrate on individual tensions and pressures, beta-theta analysis looks at the general patterns of tension anisotropy (or polarization) in the tissue. Individual tensions can be calculated once the polarization is determined, but this is not the major focus in this work. This unique approach makes beta-theta analysis an interesting companion and complement to existing force-inference methods.

CHAPTER 4

Investigating the internal tensions of germband retraction through triple-junction angle analysis

Authors of Manuscript

Monica E. Lacy, Tracy S. Edwards, Holley M. Lynch, M. Shane Hutson

This chapter has been submitted to *Physical Review Letters* as "Investigating the internal tensions of germband retraction through triple-junction angle analysis".

Abstract

During the essential morphogenetic process of *Drosophila* germband retraction, the germband tissue undergoes major migration and shape change, which is understood to result from both internal germband tensions and external stresses. Understanding of these forces has hitherto been limited by the inability to distinguish the relative strengths and directional effects of internal tensions and external stresses. We present a new way of analyzing the internal tension anisotropy, or polarization, of the germband cells based on the angles formed by the three cell edges that meet at each triple junction in the tissue. This method uses patterns in the distribution of triple-junction angles throughout the tissue to find the direction of minimum edge tension and the relative magnitude of polarization. Our results indicate that polarization and external stress anisotropy both increase over the course of retraction, acting in the same direction but with different strengths in different segments of the germband.

Introduction and Beta-Theta

Biophysics research in model organisms such as *Drosophila melanogaster* has often focused on major morphogenetic events, including embryonic germband retraction. During retraction, the twelve germband segments change shape as the epithelium retracts rostrally around the posterior end of the embryo, elongating toward the amnioserosa, a connected extraembryonic tissue. The individual

germband cells produce the segment elongation without intercalation by elongating in the same direction (Brody, 1999; Schöck and Perrimon, 2002).

Physical evidence shows that the germband experiences mechanical force from the amnioserosa and requires amnioserosal integrity for proper retraction (Schöck and Perrimon, 2002; Schöck and Perrimon, 2003; Lynch et al., 2013). On the other hand, isolated patches of germband cells retain much of their elongation, and some elongate reasonably well even with an ablated amnioserosa, indicating a role for autonomous cell elongation (Lynch et al., 2013). The epithelial germband thus is influenced by both anisotropic external stress and internal polarization, each of which either drives or opposes elongation toward the interface with the amnioserosa.

Previous work by Lynch et al. investigated the balance of anisotropies by analyzing *in vivo* wound expansion following linear ablations of each segment, both parallel and perpendicular to the direction of elongation (Lynch et al., 2013). The results were matched by multiple finite-element simulations, using existing models in which orthogonal dashpot networks approximate cell viscosity and parallel spring-dashpot combinations (Kelvin-Voigt viscoelastic elements) serve as truss elements in addition to the tensions carried by cell edges (Brodland et al., 2007; Hutson et al., 2009; Lynch et al., 2014). To represent the anisotropy of internal cell-edge tensions and stresses applied at the edges of the mesh, Lynch et al. defined anisotropy parameters (f for internal polarization and $\frac{\Delta}{\sigma}$ for external stress) and organized their results in terms of a phase space for polarization and stress anisotropy pairs (Lynch et al., 2014). The coordinate pairs that produced the most accurate aspect ratios and orientations for cells and wounds fell into two categories: either the anisotropies reinforced each other to produce extreme elongation, or they worked perpendicularly to counteract each other and restrain cell elongation. The vast majority fell into the second category, indicating that perpendicular internal and external forces are most likely to produce stable elongation.

This insight into germband retraction forces was limited by the inability to reduce the many possible parameter fits to a single solution. Here, we introduce beta-theta analysis, a new way to evaluate polarization from cell-edge tensions through the angles at the triple junctions where germband cell membranes meet. The theory behind this method focuses on the geometry of triple junctions, where three cell edges meet. For each edge within a tissue, we define the edge tension γ to depend on the average edge tension $\bar{\gamma}$ and the polarization parameter f (defined as positive when the direction of polarization matches cell elongation) so that

$$\gamma = \bar{\gamma}(1 - \frac{f}{2}\cos 2(\beta - \beta_o)).\qquad(4\text{-}1)$$

The tension also depends on an edge orientation angle β and a reference direction β_o so that for positive values of f, minimum edge tension ($\bar{\gamma}(1 - \frac{f}{2})$) occurs for $\beta = \beta_o$ and maximum tension ($\bar{\gamma}(1 + \frac{f}{2})$) occurs for $\beta \perp \beta_o$. (Note that changing the sign of f is equivalent to changing β_o by 90°.)

We also consider triple junctions to be moving slowly enough that viscous forces are neglected and equilibrium conditions apply (Brodland et al., 2014). Thus, for given values of f, β_o, and β_1, the edge tensions that meet at a triple junction can be written as

$$F_{net,x} = \bar{\gamma}[(1 - \frac{f}{2}\cos 2(\beta_1 - \beta_0)\cos \beta_1) + (1 - \frac{f}{2}\cos 2(\beta_2 - \beta_0)\cos \beta_2) + (1 - \frac{f}{2}\cos 2(\beta_3 - \beta_0)\cos \beta_3)] = 0 \quad (4\text{-}2)$$

and

$$F_{net,y} = \bar{\gamma}[(1 - \frac{f}{2}\cos 2(\beta_1 - \beta_0)\sin \beta_1) + (1 - \frac{f}{2}\cos 2(\beta_2 - \beta_0)\sin \beta_2) + (1 - \frac{f}{2}\cos 2(\beta_3 - \beta_0)\sin \beta_3)] = 0, \quad (4\text{-}3)$$

yielding unique solutions for β_2 and β_3.

We define another parameter, θ, as the opening angle opposite an edge at a triple junction; this takes into account not only the orientation of one edge, but the placement of other edges as well. In

simulation, these opening angles can be plotted opposite orientation angles (referred to here as a beta-theta plot) to give more information about the simulated tensions. For example, θ reaches a maximum at $\beta = \beta_o$, corresponding to edges that experience minimum tension, while θ_{min} corresponds to edges that carry maximum tension [Fig. 4-1(a)]. The magnitude of polarization also produces changes in the plot, with greater differences between values of θ_{max} and θ_{min} as f becomes larger. The fits produced for different values of f in simulated beta-theta plots should be applicable to experimental data that follows the theoretical patterns established here.
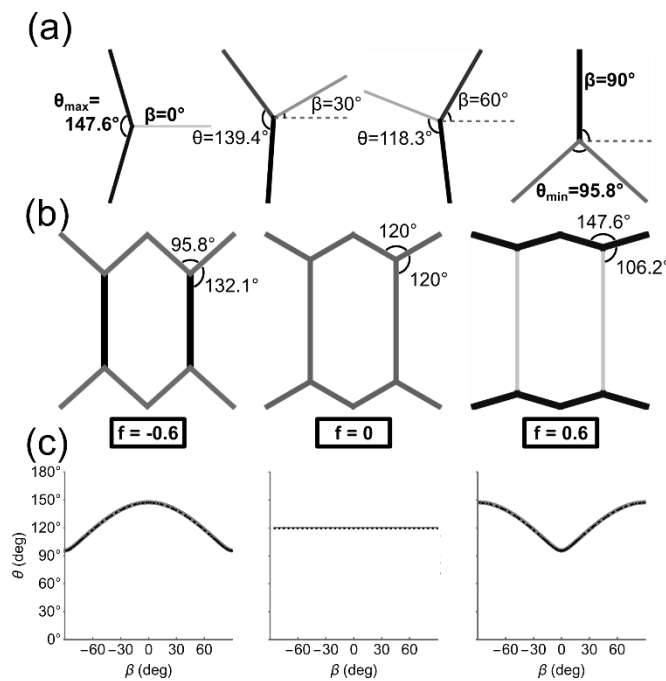
Fig. 4-1. Theoretical beta-theta distributions. (a) Given internal polarization and the orientation of one edge (β), there are unique solutions to the angles formed at triple junctions. Note that for edges parallel or perpendicular to the direction of minimum tension (β₀, dashed horizontal axis), the opposite angle at the junction (θ) reaches a maximum or minimum, respectively. (b) Cells with same aspect ratio but different shapes due to polarization caused by relative edge tensions, shown by both line thickness and darkness. For negative polarization (f = -0.6), vertical edges are most tense and contract to encourage horizontal elongation. For positive polarization (f = 0.6), horizontal edge tensions are strongest, encouraging vertical elongation. (c) Beta-theta distribution plots for same values of f, showing minima and maxima for θ where β corresponds to directions of maximum and minimum tension.

Methods

To gather images for experimental analysis, we chose a *Drosophila* strain (ubi-DE-Cad-GFP; Drosophila Genetic Research Center, Kyoto, Japan), which enables fluorescent imaging of E-cadherin in cell-cell junctions (Oda and Tsukita, 2001). Embryos were collected on grape juice agar plates smeared with yeast paste and aged at room temperature (25° C) or in an incubator (15° C) until germband retraction (~7-8 hours after collection); they were dechorionated in a solution of 50% bleach, mounted laterally on a glass coverslip with a heptane-based adhesive and slightly dehydrated, then immersed in halocarbon 27 oil and covered by an oxygen-permeable membrane attached to a metal slide (Ma et al., 2009). Embryos were imaged with a 40X, 1.3 NA oil-immersion objective on a spinning disk confocal microscope (WaveFX-X1, Quorum Technologies, Ontario, Canada; built onto an Eclipse Ti, Nikon Instruments, Melville, NY). Stacks of image planes ranging from 20 to 40 μm in height were later resolved into Z-projections in ImageJ (Rasband, 1997-2017), with multiple X-Y stage positions then stitched together using ImageJ's MosaicJ tool to provide views of the entire embryo. In each image, individual cells and cell-edge orientations were identified using SeedWaterSegmenter, a watershed algorithm that allows precise user correction of automatic watershed assignments (Mashburn et al., 2012). The developmental stage was also determined by a process detailed elsewhere (Lynch et al., 2014), comparing contours at the germband-amnioserosa interface to a standard set representing percentages of germband retraction completion.

Mathematica was used for staging and angle analysis, importing a cellular Voronoi diagram for each segment to create plots of triple-junction opening angles (θ) vs. orientation angles (β) (2016). Plots were created for all instances of each segment, as well as for the aggregate data for each segment, rotated so that the composite long axis of the cells was vertically aligned. The nonlinear fits for these plots were then used to interpolate between curves for values of f between -2 and 2 to find values for each segment's polarization.

Results and Discussion

For these fits, it was particularly important to determine β_o, the direction of lowest edge tension. In all twelve segments, β_o is close to 0°, setting the direction of maximum tension close to 90°, toward the amnioserosa. These vertical tensions indicate that f is negative, representing polarization that opposes the direction of cell elongation. (Thus, a downward trend in f represents stronger polarization.) The first parts of Fig. 4-2(a-c) show the similarity between these plots and those created from theoretical angle sets in Fig. 4-1(b), demonstrating the successful application of our equations to live epithelial images.
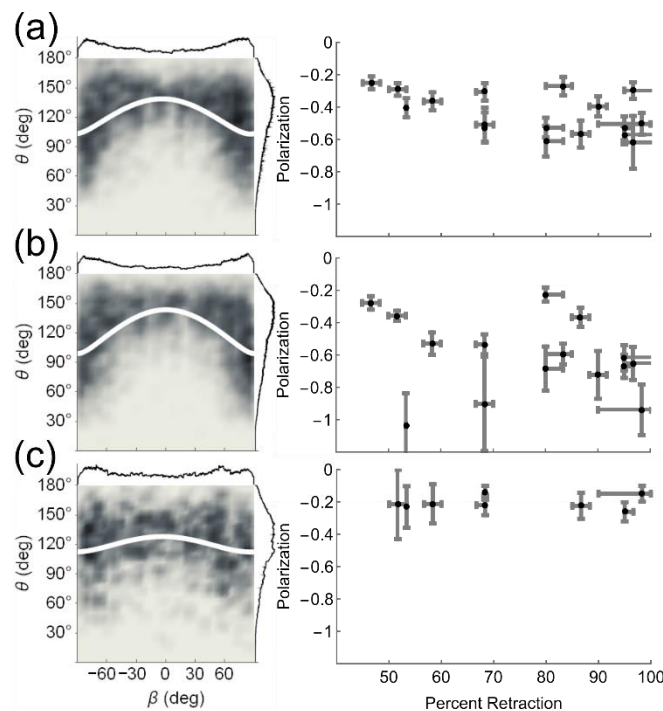
Fig. 4-2. Experimental beta-theta distributions. Beta-theta density histograms and polarization vs. time for experimental data from segments (a) A3, (b) A5, and (c) A8. Beta-theta best-fit curves in white, with greater range of θ denoting stronger polarization. Polarization is shown as a function of developmental progress in germband retraction, with each data point from a separate embryo (N=17 for A3 and A5, N=8 for A8). Note that negative trend indicates stronger polarization.

Based on the signs of external force from the amnioserosa and differences in reaction to ablation between segments A2 and A5, previous simulation results for internal and external anisotropies

had predicted that the crook of the germband (segments A4-A6) would show this combination of vertical

polarization encouraging horizontal (or rostral-caudal) elongation, opposed by external force anisotropy

driving vertical elongation (Lynch et al., 2014). Some non-crook segments were expected to show the

reverse, with polarization driving vertical elongation. Instead, our results indicate that internal

anisotropy acts against vertical elongation in all twelve segments, not only the crook segments that show

the strongest evidence of external vertical force. Although the direction of polarization is the same for all

germband segments, the magnitude differs significantly, with mean values of f ranging from -0.21 for

segment A8 to -0.72 for A5. As seen in the beta-theta plots, the strongest composite values of f are

found in the crook segments, A5 and A6, and the surrounding segments [Fig. 4-2(a-c), left]. In addition to

a composite value of f for each segment, the data was broken down by individual embryos to examine f

as a function of the percentage completed in germband retraction [Fig. 4-2(a-c), right]. As with the

composite data, crook segments show overall higher values for f. More strikingly, almost all segments

show an increase in f over time, though the trends are difficult to follow, partly due to natural variation

between individual embryos.

To better compare these crook segments with others, segment A5, along with the more anterior

and posterior segments A3 and A8, were selected for more thorough investigation of trends in

polarization. Figure 4-3 shows the set of resulting plots for image sequences of these three segments in a

single embryo over time, demonstrating more coherence and nuance than the overall collected data in

the changes in f for all three segments. Initially, the plots in Fig. 4-3(a) agree with the trends from the

collected data from multiple embryos, with A5 most strongly polarized at the beginning; unlike the

isolated data points, however, A5 does not maintain the strongest polarization, being surpassed by A8 by

mid-retraction and by A3 by late retraction.
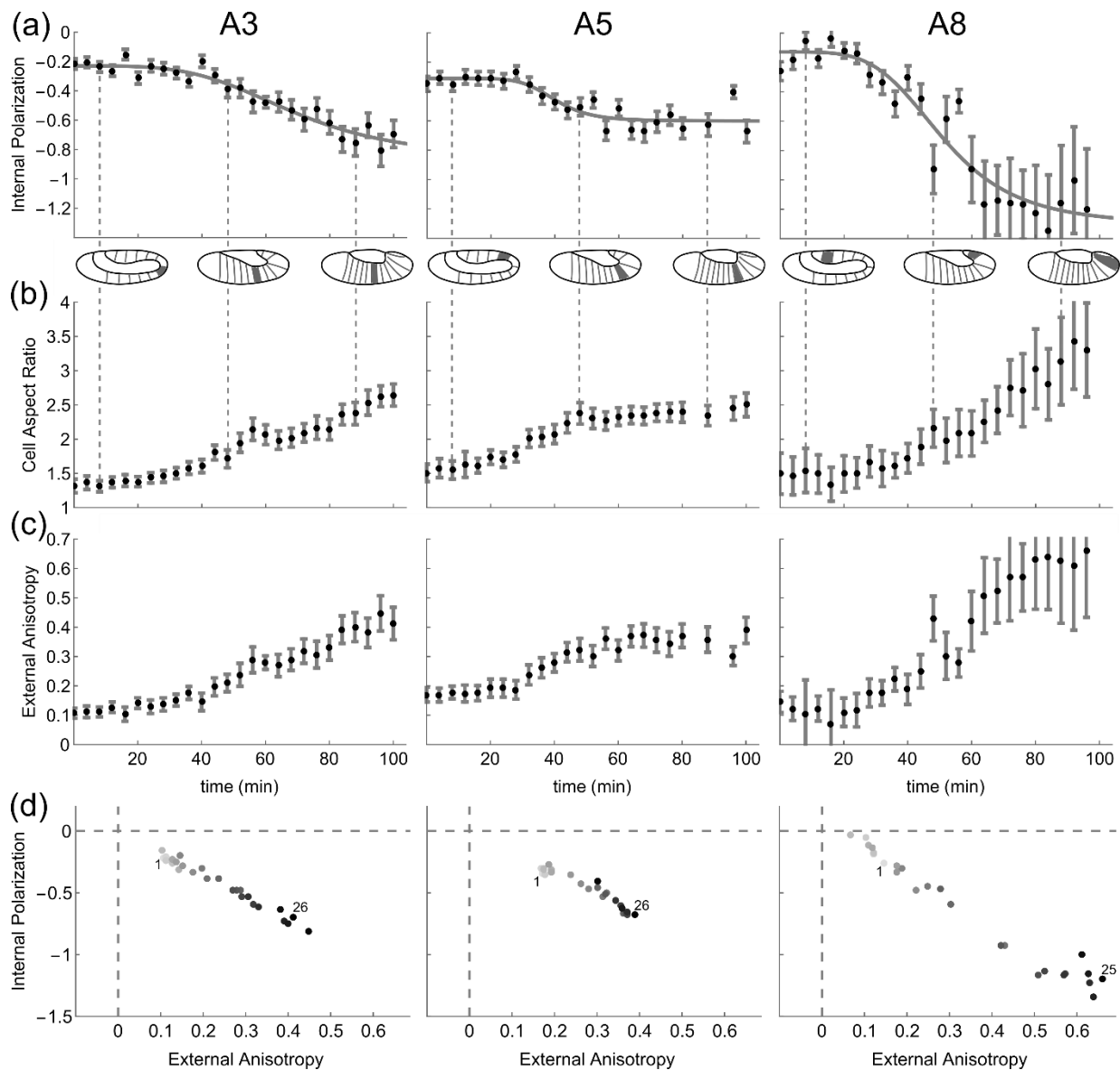
Fig. 4-3. Results of beta-theta time sequence analysis. (a) Polarization in segments A3, A5, and A8 vs. time (min) from beginning of imaging (0 min corresponds approximately to beginning of retraction, 100 min to 87% retraction). Data points represent time sequence from one embryo. Sigmoidal fits (gray lines) give time constant for point of inflection: A3=51 min, A5=43 min, A8=64 min. Cartoons show lateral view of early, middle, and late germband retraction with relevant segment darkened. (b) Composite aspect ratio (κ) vs. time (min). (c) Interpolated values of external stress anisotropy parameter $\frac{\Delta}{\sigma}$ vs. time from initial imaging (min). (d) Polarization vs. interpolated values of $\frac{\Delta}{\sigma}$. Note that all points lie in the fourth quadrant, indicating that polarization and stress oppose each other, with external stress causing vertical germband cell elongation and polarization opposing it. Data points increase in darkness with time.

Despite the differences from the plots of individual points in Fig. 4-2(b), our detailed time

sequences for A3, A5, and A8 also show a clear increase in polarization. While the single time points of

45

Fig. 4-2(b) are somewhat scattered, the time sequences in Fig. 4-3(a) offer a more coherent shape, with

an initially slow increase in *f*, followed by a period of rapid increase and a leveling off. This behavior can

be approximated by sigmoidal fits similar to the Hill equation, of the form

$$f = (r_{\max} - r_{\min}) \frac{t^h}{t_{50}^h + t^h} + r_{\min} \qquad (4\text{-}4)$$

where *t* represents the time in minutes, $r_{\min}$ and $r_{\max}$ are approximately the initial and final polarization

values, *h* is a coefficient that indicates cooperativity when this equation is used in the context of

receptor-ligand binding, and t_{50} represents the time at the half-max value of *f*. Table 4-1 shows the

parameter values for each of the three segments, demonstrating numerically that as shown in Fig. 4-

3(a), A5's increase in anisotropy begins earlier (t_{50}) and with stronger anisotropy ($r_{\min}$) than either A3 or

A8, but levels off sooner with weaker final anisotropy ($r_{\max}$).

Segment	A3	A5	A8
r_{max}	-0.87 ± 0.15	-0.60 ± 0.03	-1.31 ± 0.16
h	3.91 ± 1.26	7.13 ± 3.97	4.36 ± 1.50
t_{50} (min)	69.08 ± 9.83	39.98 ± 3.51	51.10 ± 4.54
r_{min}	-0.23 ± 0.02	-0.31 ± 0.03	-0.13 ± 0.07

Table 4-1. Parameters for the Hill-like equation fits for A3, A5, and A8. Note especially the differences in initial and final
polarization and time at half-max.

To extract the most information from these values of *f*, we returned to Lynch et al.'s parameter

space, which explored the theoretical relationship between *f* and the external anisotropy parameter $\frac{\Delta}{\sigma}$.

The coordinates for possible parameter fits were determined from contours of composite aspect ratio

values (κ) for the wounds in each segment, which were quantified from experiments, as well as for the

cells in each segment (Lynch et al., 2013; Lynch et al., 2014). The cell aspect ratio had been treated as a

constant with the value $\kappa \cong 1.33$ across all segments at all stages in the simulations, but with our image

sequences, we were able to average moment of inertia tensors for each cell in the segment to find a

distinct value of κ for each timepoint. Figure 4-3(b) plots κ over time, showing a consistent increase for

all three segments (Weisstein, 2017).

With values of f and κ for each point in our time sequence, we were able to interpolate values

for $\frac{\Delta}{\sigma}$ based on the nearest values in Lynch et al.'s parameter space. The interpolated values of $\frac{\Delta}{\sigma}$ are

uniformly positive and increase over time as f becomes more negative [Fig. 4-3(c), cf. Fig. 4-3(a)]; this

agrees with the expectation of external anisotropy acting against polarization to drive vertical

elongation. Like f, $\frac{\Delta}{\sigma}$ begins stronger in A5 but is outstripped by both A3 and A8 as retraction progresses.

Figure 4-3(d) shows the increase of both internal and external force anisotropy over time, keeping pace

with the heightened cell elongation.

The trends shown in Fig. 4-3 may seem to contradict Lynch et al.'s conclusions, but they also

explain some of their data, which was interpreted without recourse to time sequences. The ablation

experiments that led to the conclusion of stronger vertical polarization in A5 were performed at roughly

36% of retraction, before A5 loses ground to A3 and A8, so our results agree that A5 shows the strongest

polarization at that point (Lynch et al., 2014). Another somewhat puzzling finding for Lynch et al. was

that when the amnioserosa was heavily ablated, the cells in segment A5 came much closer to eventually

elongating normally than in segment A2. The authors concluded that this was evidence of forces on A5

from the far, unablated side of the embryo; if A2 behaves similarly to A3, however, Fig. 4-3(a) suggests

instead that the stronger late polarization inhibits A2's elongation compared to A5.

Conclusions

The differences between the data shown in Figs. 4-2 and 4-3 make it clear that understanding

the full picture of germband forces requires similarly detailed observation of all segments, especially to

compare the behavior of A5 with the other crook segments and establish comparisons between

neighboring segments. Regardless of the availability of time sequences, however, all of our results agree

that polarization acts vertically in all germband segments. These findings complement the results of

Walters et al., who observed upregulated Myosin II along the anterior and posterior edges of germband

cells in late retraction (Walters et al., 2006). This distribution is characteristic of the planar cell polarity

that drives intercalation in the earlier events of germband extension, and now has been shown to be

absent during a post-extension pause, after which it reappears in retraction (Zallen and Wieschaus,

2004; Blankenship et al., 2006). Enhanced anterior and posterior Myosin II implies vertical edge

contraction, consistent with increasing vertical polarization; the agreement with observed protein

distributions, as well as Lynch et al.'s ablation experiments, provides strong support for the general

accuracy of our results.

In this work, we have shown that beta-theta analysis agrees reasonably with existing

experimental data, suggesting that it can be applied to other monolayer tissues in which cell shape

change, rather than intercalation, drives tissue shape change and migration. Future work should include

such broader application, in addition to further assessing the differences between our methods and

other current force-inference tools, such as the finite-element-based video force microscopy and CellFIT

(see Fig. B-3 for CellFIT polarization estimates) (Brodland et al., 2010; Brodland et al., 2014). Fine-tuning

this and other reverse modeling methods will allow combination with more invasive tools like optical

tweezers to eventually quantify the forces at work in germband retraction and a host of other epithelia

(Neuman and Nagy, 2008).

CHAPTER 5

Conclusions and Future Work

The Amnioserosa as a Unifying Theme

This dissertation presents a body of work in which one major unifying theme is the function and purpose of the amnioserosa, the extraembryonic tissue that is involved in and essential for several major morphogenetic events in the embryo. Chapter 2 establishes that the amnioserosa's structural integrity is crucial for normal embryonic development, and how much there is still to understand in its connection to and influence on the germband. The research in Chapter 4 focuses on the germband, but its conclusions also apply to the amnioserosa's role in germband retraction. Following these concluding remarks, two of the appendices supplement the material in Chapter 4, and the final appendix describes research on light-mediated control of motor proteins in the amnioserosa. From beginning to end, this transient and short-lived tissue plays a central role in this dissertation, just as it does for *Drosophila* itself.

The Balance of Amnioserosa and Germband

In my study of germband retraction in Chapter 4, I approached the question of how internal and external forces contributed to retraction by focusing on the internal (germband edge-tension) forces. The results of my analysis show that the polarization of the germband cells and segments does not vary in direction with position in the germband, with autonomous cell elongation (discounting external forces) tending toward the horizontal, in contrast to the net vertical elongation. Ubiquitous vertical polarization is somewhat unexpected, since Lynch et al. predicted that direction would vary in different regions of the germband, but the magnitude and change over time vary between segments, as seen in the time sequences of segments A3, A5, and A8 (see Fig. 4-3) (Lynch et al., 2014).

The vertical anisotropy values obtained from the time sequences are only one side of the balance of forces we seek to understand and quantify. Lynch et al.'s previous simulations of germband wound responses, which produced possible parameters that mostly set internal and external anisotropy at odds with each other, suggested that controlled elongation usually stems from perpendicular external and internal force anisotropies. Using the experimental beta-theta values for polarization, I found that the best interpolations in this parameter space uniformly involved orthogonal internal and external anisotropies, reinforcing the theory that this arrangement is the most likely to produce stable elongation in the germband. These results also upset prior predictions that the amnioserosa might exert force preferentially on certain parts of the germband and suggests that external pulling force drives germband segment elongation all along the germband, not only where there is strong physical evidence (Schöck and Perrimon, 2002; Lynch et al., 2014).

These results do not exist in a vacuum, but can be compared to the knowledge gained from other germband retraction research. In strong support of the findings of vertical germband polarization, germband cells in retraction show evidence of anisotropic concentrations of myosin II, which is associated with cell contractility, along vertical cell edges (Walters et al., 2006). This accords with high vertical edge tensions and horizontal autonomous elongation. Moreover, this distribution is characteristic of planar cell polarity in the germband as described in Chapter 2, with the same distribution observed during germband extension, when it drives horizontal cell elongation and intercalation (Zallen and Wieschaus, 2004; Blankenship et al., 2006).

My results also explain some of the odd features noted by Lynch et al., such as the strong vertical wound expansion in crook segments coupled with the differences in crook and ventral cell elongation in late retraction after amnioserosa ablation (2013). Based on the simulations that suggested that some segments elongated because of dominant horizontal polarization, Lynch et al. concluded that segment A2's cells elongated less than A5's with an ablated amnioserosa because A2's elongation was

driven weakly by horizontal tensions and A5's elongation was still affected by vertical (albeit twisted)

external forces from the other, unablated half of the embryo (2014). In contrast, my findings show that

internal polarization resists elongation in all segments, and the data considered over time offers an

explanation for the behavior observed by Lynch et al. At the time of Lynch et al.'s wounding experiments,

my results show that segment A5 does indeed experience the strongest vertical forces, so that its

wounds expand more vertically. Later, however, segment A3 overtakes A5 in vertical polarization; if its

neighbors develop similarly, it is natural that A2's stronger vertical tensions would cause its cells to

elongate less than A5's when the external force of the amnioserosa is removed. Figure 5-1 illustrates the

directions and relative strengths of internal and external forces in Lynch et al.'s model and in the new

model suggested by my results.
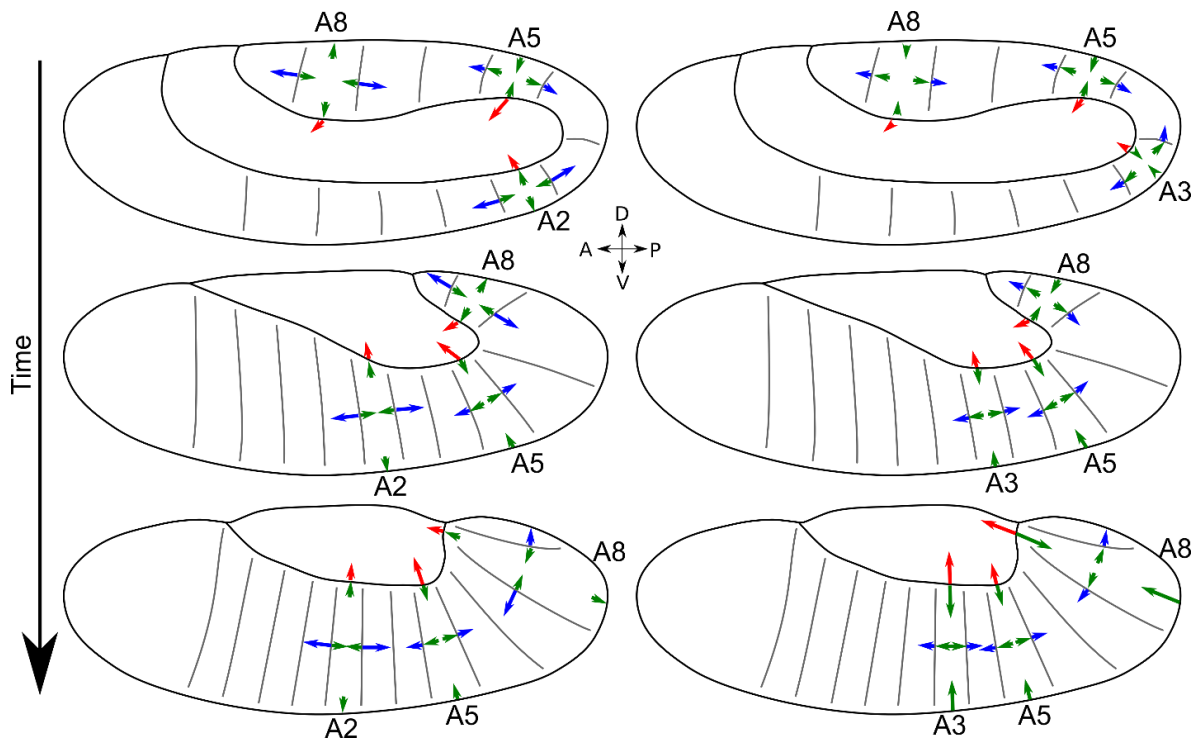
Fig. 5-1. Old (left) and new (right) models of forces acting on the germband during retraction. In the old model, the crook segments (represented here by A5) show internal polarization (green) resisting the dominant vertical external force (red), but for some other segments the external force is horizontal (blue). In the new model, all segments experience dominant vertical external force and corresponding vertical polarization. Note that while the old model has no data on change in strength of anisotropy over time, the new model shows that A5 initially has the strongest anisotropy and is later surpassed by both A3 and A8, as shown by the relative lengths of the colored arrows.

In light of these findings, what seems to be occurring in the germband during extension and retraction can be described generally by the analogy of muscle contraction. Germband extension may be like concentric contraction, in which the muscle contraction causes a change in position (e.g. lifting a weight); after the pause following extension, germband retraction then resembles eccentric contraction, in which the muscle contracts in the same way, but serves to mitigate and control elongation in the opposite direction. In other words, the same internal forces work to extend the germband, and then to control its retraction in the face of external force. The analogy can be further applied to failures in germband retraction due to lack of integrity in the amnioserosa, where we now suspect that little or no vertical elongating force is applied in the absence of the amnioserosa. In this case, the "muscle" remains contracted but stationary, with no external force to change the balance.

This new hypothesis of vertical polarization throughout the germband as a check on the dominant force from the amnioserosa fits with our general understanding of the amnioserosa's physical role in retraction, as well as current knowledge of planar cell polarity during this stage, but it is hardly the end of the story. Among other issues, the differences between my results and the predictions of the previous simulations highlights the need to obtain time-sequence data for all segments in the embryo, to see whether the trends in anisotropy in A3, A5, and A8 reflect differences between regions of the germband. With this thought, we now turn to discussing this and other future research directions suggested by my work in this thesis.

Future Questions and Research

The research and review material presented in this dissertation can provide fertile ground for continuations of this work, as well as new directions and experiments. In general biophysical terms, there is still much to be discovered about the specific tissue mechanics of *Drosophila* development. At present, force estimates mostly exist in the form of ratios or force ladders, which tell us about the

relative strength of different forces involved in a particular movement or stage, but do not offer known

quantities. The combination of these comparative measures with methods of direct measurement such

as optical tweezers may yield unprecedented results in the area of quantifying forces. Accurate

knowledge of morphogenetic mechanics will also benefit from multiscale modeling that can incorporate

elements that are currently beyond the scope of our modeling, such as the intracellular variation in cell

height, viscosity, and other attributes due to the differences between the nucleus and the cytoplasm. As

biophysics research becomes more truly interdisciplinary, it can reach new heights by taking full

advantage of the knowledge and methodology of both biology and physics.

Chapter 2 mentions several of the open questions surrounding Drosophila embryonic

development, especially as it involves the amnioserosa. Setting aside the details of its evolutionary

origin, the present-day amnioserosa interacts with the germband through a combination of signaling and

mechanical stresses that is far from fully understood. The interplay between applied forces at the

interface of the two tissues and the signaling exchanges that drive changes in both epithelia is a

beautiful and complex puzzle to be solved by the continued work of researchers focusing on multiple

stages and aspects of development.

The original research in this work as presented in Chapter 4 offers some answers, but raises

questions alongside them. My investigation of the germband's internal polarization shows intriguing

patterns that challenge prior thinking about the balance of internal and external forces during germband

retraction. With the knowledge that the internal edge tensions act against the net germband cell

elongation in retraction, we have a better picture of the amnioserosa's active involvement in retraction

and the counteractive response of the germband's polarization. However, we have only investigated

three segments of the germband in our detailed study of the germband over time, and the data from

single time points in various embryos is less informative because of the large degree of variability that

can exist between embryos, even in the same developmental stage (Brodland et al., 2014). With only

three segments, we have no basis for deciding whether the differences between A3, A5, and A8 are representative of the behavior of entire regions of the germband. Thus, a primary goal in further research is to obtain the same data for the remaining nine germband segments (or eight, since A9 is often hidden in the lateral imaging that is necessary to follow the segments throughout germband retraction).

Another direction suggested by these results is to validate the trends of polarization and the interpolated results for external force anisotropy by revisiting Lynch et al.'s wounding experiments. The experiments mimicked by the parameter-space simulations took place about 36% of the way into retraction, before our results indicate that A5 is surpassed by A3 and A8 in polarization strength (Lynch et al., 2013). A set of similar experiments done in late retraction would serve as a test of our anisotropy values, which indicate that late-retraction wounds in A5 are likely to have a lower vertical aspect ratio than in A3 or A8. If possible, an expanded version of the amnioserosa ablation experiment would also be desirable, in which the elongation of the germband cells can be recorded at earlier times as well as in late retraction.

Chapter 3's brief overview of other existing force-inference methods suggests another improvement on the methods used for beta-theta analysis thus far. CellFIT, like beta-theta theory, assumes equilibrium conditions that sum triple-junction edge tensions to zero; however, it also assesses those tensions with the additional accuracy of preserving the curved cell edges (Brodland et al., 2014). Appendix B compares the tensions calculated from beta-theta polarization values with the tensions from CellFIT meshes of the same embryos, but with no extra edge nodes, so that the meshes match the straight-edged cellular Voronoi diagrams generated by Mathematica. Future expansion and improvement of beta-theta analysis should include using the angles obtained from curvilinear meshes as well as straight edges, to better approximate the actual tissue conditions.

For biophysicists, the final pieces of the puzzle of amnioserosa-germband interaction will only fall into place when we can obtain actual values for the tensions and stresses at work in the tissue. This will require a combination of our forward and reverse modeling methods with more invasive tools like optical tweezers, which can be used to measure forces *in vivo* (Neuman and Nagy, 2008). Answering the questions posed by biophysics also involves linking these forces to tissue properties; this work should concentrate not only on germband retraction, but also on the surrounding stages of development. Germband extension involves similar planar cell polarity in the germband, but results in intercalation rather than only cell shape change, implying that the germband's response to contractile stress may change over time and is worth studying in multiple contexts (Schöck and Perrimon, 2002).

The work presented in this thesis is, in a way, representative of the spirit necessary to answer our present and future questions about the germband, *Drosophila* development, and embryonic tissue mechanics in general. Increasingly, filling the gaps in our scientific understanding will require interdisciplinary efforts, coupling decades of exhaustive biological information with mathematical concepts and cutting-edge instrumentation. The complex collaboration of biology and physics, multiscale experimentation and modeling, can develop into a symbiosis as fascinating as the balancing act of germband and amnioserosa.

Appendix A: Beta-Theta Theory

The following appendix presents more detail on the theory of beta-theta theory briefly in Chapter 4. We will begin from the first geometric principles of the theory, which is predicated on the idea that if there is a general tension anisotropy in the tissue, each cell edge has a tension based on the direction of the edge, given as Equation A-1:

$$\gamma = \bar{\gamma}(1 - \frac{f}{2}\cos[2(\beta - \beta_0)]) \tag{A-1}$$

This equation was proposed by Lynch et al. (2014) to assess edge tensions driving autonomous cell elongation in a cellular finite element model, with β_o representing the direction of autonomous elongation, β representing the relative angle of the cell edge, and absolute values of f ranging from 0 (where $\gamma = \bar{\gamma}$) to 2 (maximum anisotropy, where γ ranges between 0 and $2\bar{\gamma}$).

The second part of the geometric theory comes from considering the forces acting on a triple junction, where three edge tensions are acting. These tensions sum to zero in cases where motion is slow enough that viscous forces are negligible and the system is essentially in equilibrium, giving us the force equations

$$F_{net,x} = \gamma_1 \cos\beta_1 + \gamma_2 \cos\beta_2 + \gamma_3 \cos\beta_3 = 0 \tag{A-2}$$

and

$$F_{net,y} = \gamma_1 \sin\beta_1 + \gamma_2 \sin\beta_2 + \gamma_3 \sin\beta_3 = 0. \tag{A-3}$$

These equations can be solved by returning to Eqn. A-1 and choosing values for f, β_o, and β (which becomes β_1 in Eqns. A-2 and A-3, as the solution for γ becomes γ_1). With two equations, we can substitute the remaining tensions in terms of their respective angles and find unique solutions for the two remaining unknowns, β_2 and β_3, given β_1.

By iterating over many possible values for β_1, we can come up with a large array of sets of edge

angles that can occur for a given value of f. We can also look at these unique angle solutions from

another perspective, considering the angles that form between the edges at the junction rather than the

orientation of each edge. We can define the angle opposite the edge under consideration as θ, which

can be calculated from the values of β for each edge in the junction. Figure A-1 illustrates the

relationship between β and θ.
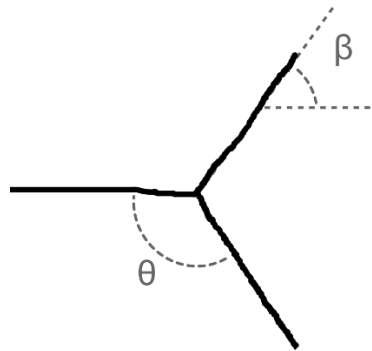
Fig. A-1. Illustration of beta and theta angles for a single cell edge at a triple junction. Here the direction of minimum tension, β_o, is horizontal, indicated by the dashed horizontal line that forms the other side of the angle labeled β. The other two edges meet to form the opposite angle, θ.

Further insight into the patterns formed by these angles can be gained by plotting theoretical

distributions of angle sets so that β and θ can be compared directly, referred to throughout Chapter 4 as

a beta-theta plot. This type of plot reveals a relationship between the orientation angles and opening

angles; the edges oriented parallel to the direction of minimum tension are associated with the largest

opposite opening angles, and the perpendicular edges are associated with the smallest respective

opening angles. Theoretical plots for different values of f also show differences in the range of θ, with

larger absolute values of f corresponding to a greater spread between the maximum and minimum

opening angles.

The next step is to apply this theory to experimental data, which can be readily obtained by

using node coordinates to calculate the orientations of the cell edges in a single image of a tissue sheet.

From these angles, we could make experimental plots and try to match them to a set of best-fit

parameters by iterating over possible values of f and β_o until we find the best match for the data, but

there is a more elegant option. The clear maxima and minima of the theoretical beta-theta plots make it

simple to find the direction of minimum tension, which occurs at the value of β that corresponds to

maximum values for θ. Finding a value for f is less straightforward, but we can solve Eqns. A-2 and A-3

for f based on the spread of θ by setting β_1 equal to the direction of either maximum or minimum

tension, and the other two orientation angles defined so that the angle between them is either θ_{min} or

θ_{max}. From this we obtain two equations for f,

$$f(\theta_{min}) = \frac{2 - 4\cos\left[\frac{\theta_{min}}{2}\right]}{\cos\left[\frac{3\theta_{min}}{2}\right] + \cos\left[\frac{\theta_{min}}{2}\right] - 1} \tag{A-4}$$

and

$$f(\theta_{max}) = \frac{4\cos\left[\frac{\theta_{max}}{2}\right] - 2}{\cos\left[\frac{3\theta_{max}}{2}\right] + \cos\left[\frac{\theta_{max}}{2}\right] - 1}. \tag{A-5}$$

One way to obtain a value of f is by solving these equations for θ_{min} and θ_{max}, which yields

cubic equations in terms of $\cos\frac{\theta}{2}$, of the form

$$1 - \frac{f}{2} + (-2 + f)\cos\frac{\theta_{min}}{2} - 2f\,(\cos\frac{\theta_{min}}{2})^3 = 0 \tag{A-6}$$

and

$$1 - \frac{f}{2} + (-2 - f)\cos\frac{\theta_{max}}{2} + 2f\,(\cos\frac{\theta_{max}}{2})^3 = 0 \tag{A-7}$$

with roots that must be chosen carefully for different regions of f values, in order to find solutions

within the real range of cosine values. Graphs of results for these roots show that only one of the three

roots for each equation provides a real solution, as shown in Fig. A-2 (color-coded to differentiate among

the three roots) along with the values of θ_{min} and θ_{max} that result from these roots. The range of values

58

for θ_{min} and θ_{max} as a function of f are reverses of each other, but in reality only the upper portion of each curve represents θ_{max} and only the lower portion represents θ_{min}, so that each curve makes sense only for positive values of f.
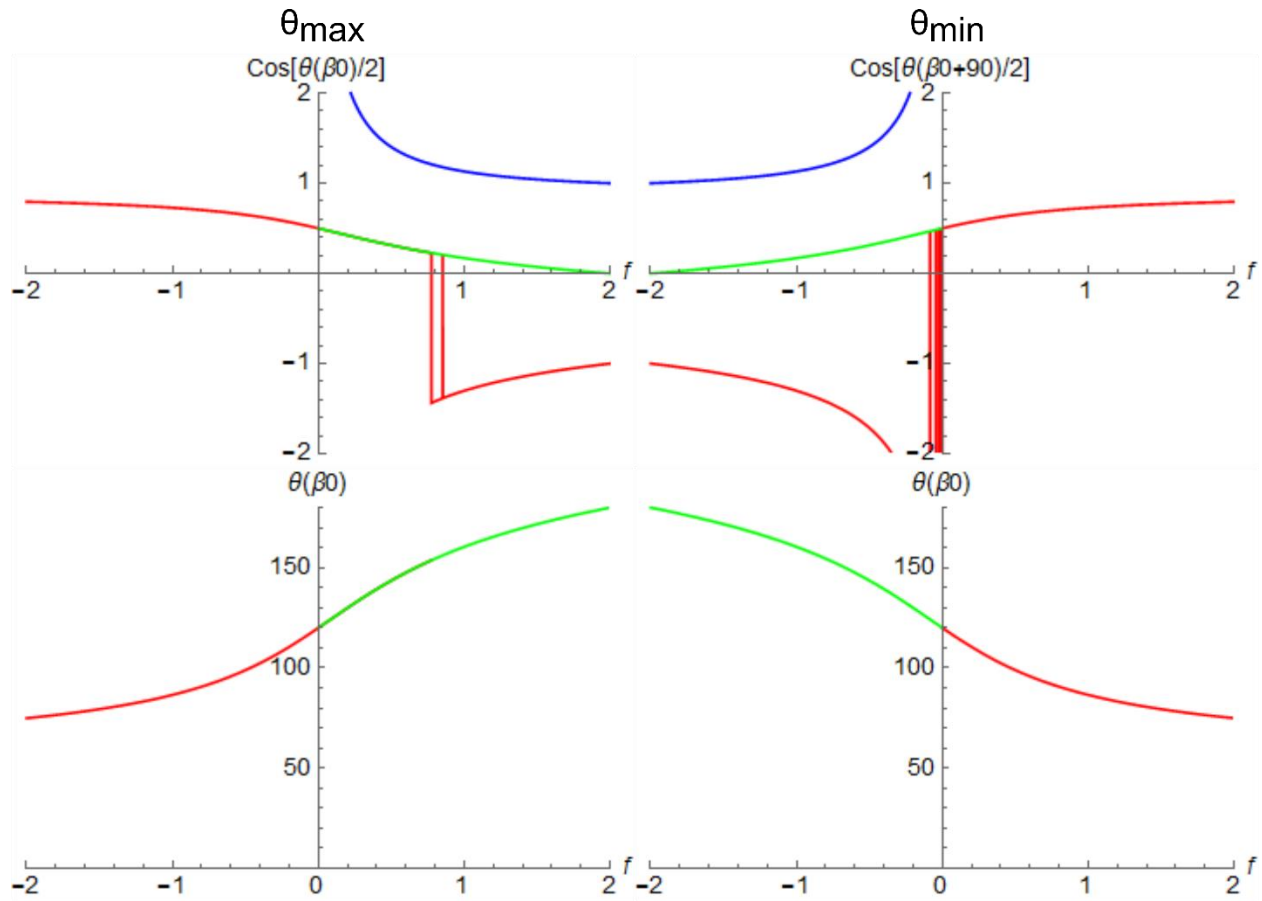
Fig. A-2. Roots for the equations solving for maximum and minimum values for opening angles. Top row shows roots of the equations for $\theta_{max}$ and θ_{min} in terms of $\cos\frac{\theta}{2}$ for values of f between -2 and 2, with the first root in red, the second root in green, and the third root in blue. Only roots with values that fall between -1 and 1 constitute real solutions for these equations, so the third root is excluded. Second row shows θ_{max} and θ_{min} for values of f between -2 and 2, with the same color coding as in the first row. Note that the maximum and minimum curves here are mirrors of each other, and only the portions of the curves for positive values of f correspond to the actual values for minimum and maximum opening angle.

Solving for f as a function of minimum and maximum θ is one option for estimating f from a beta-theta plot, but there is a second idea that avoids the complex roots of Eqns. A-6 and A-7. This approach, which takes advantage of the powerful interpolation capabilities of computational software, is to use the theoretical set of β and θ values for each f to construct interpolation functions in

Mathematica. These functions are then combined to give two different interpolation functions, shown in Fig. A-3, one of which fits best for positive values of f and one of which fits best for negative values. The interpolation functions are then used to estimate f based on the nonlinear model fit for an experimental dataset of β and θ values calculated from the cell edges of a cellular Voronoi diagram.
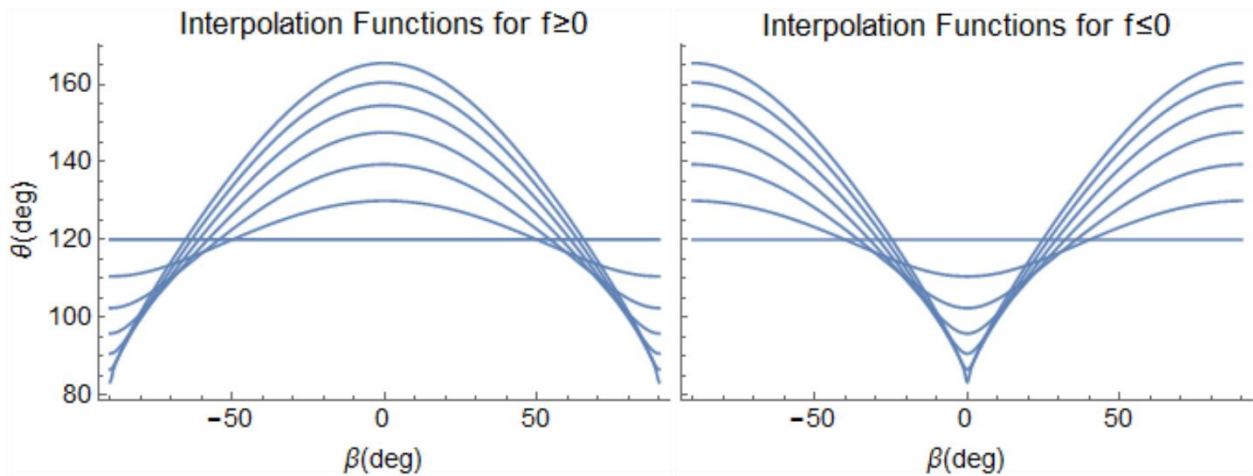
Fig. A-3. Interpolation functions for values of f between 0 and 1.2 and 0 and -1.2, respectively. Flat lines represent f =0 and increasingly curved lines represent increasing magnitudes of f.

In the work presented in Chapter 4, all the germband segment datasets were rotated according to their composite aspect ratio before nonlinear fits were applied, so that the segment as a whole was vertically oriented. Since all of our beta-theta plots showed θ_{max} close to 0°, the most suitable interpolation function was the one for positive values of f. This seems strange in light of the fact that all our estimates of f in Chapter 4 are negative, but the interpolation functions use a generalized definition in which f is positive if the minimum tension occurs at 0°. For the specific example of germband segment polarization, we define f as positive if it drives autonomous cell elongation in the same direction as net cell elongation; since the net elongation direction is approximately 90° and $\beta_o \cong 0°$ in all cases, polarization drives horizontal autonomous cell elongation perpendicular to net elongation and f is ultimately defined as negative for subsequent data analysis. In the initial fits, however, the dataset

rotations render positive values of f that resemble those in the first interpolation function graph in Fig.

A-3.

Appendix B: Supplemental Data for Chapter 4

This appendix presents supplemental data for the research discussed in Chapter 4. This includes

additional examples of theoretical beta-theta distributions as well as extra experimental data that

supplies details for the results presented in the paper. First, the limited selection of values for f (internal

polarization) in Fig. 4-1 does not display the full range of f, which runs from -2 to 2 (shown at intervals of

0.4 in Fig. B-1). At the far ends of this range, the solutions for β become non-unique, as shown in the

plots for f = ±1.4 and 1.8.
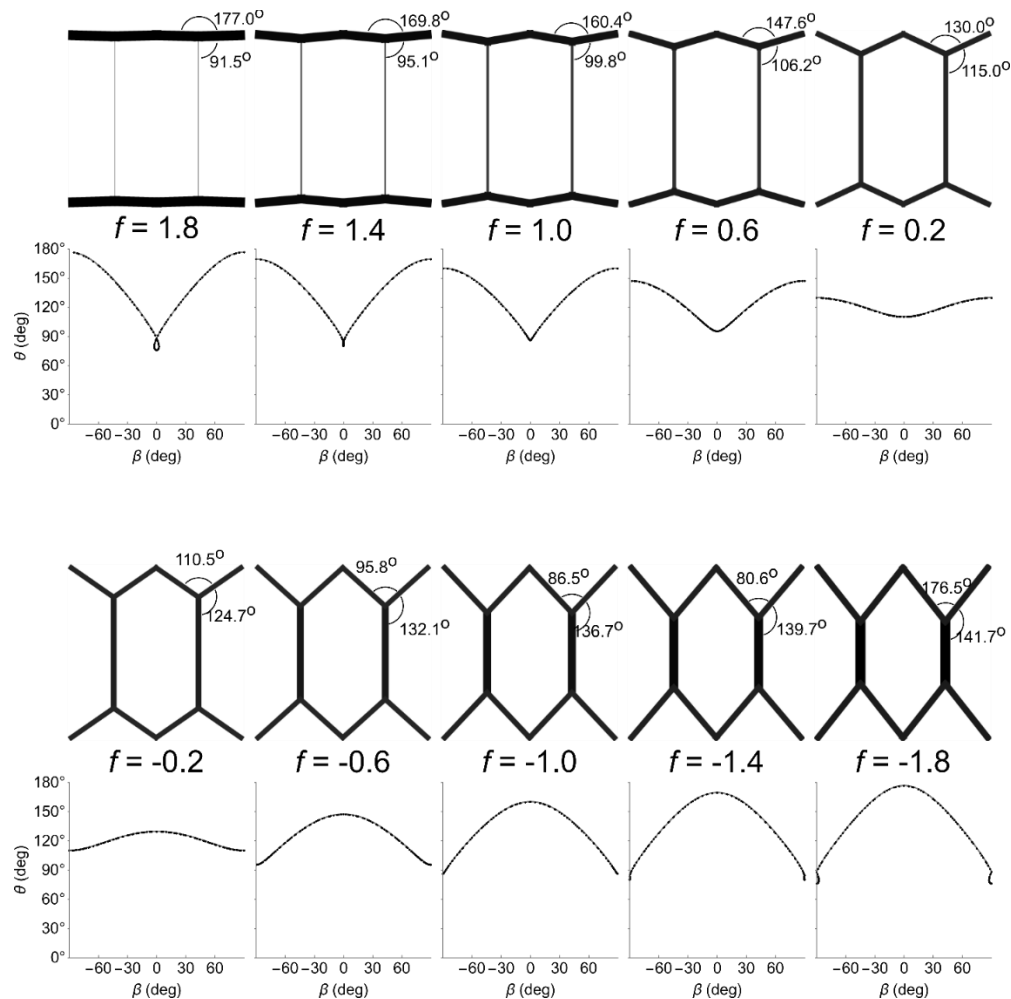
Fig. B-1. Drawings of single cells and accompanying beta-theta plots for different values of f. A larger range of values is
included here than in Fig. X of Chapter 4. Note that the cell drawings show only the symmetric solutions for f = -1.4 and -1.8;
there are multiple solutions at some angles for these higher magnitudes of f, including f = +1.4 and +1.8, as seen in the plots
below the cell drawings.

Chapter 4 shows specific data only for segments A3, A5, and A8, since these segments were the ones used in the time sequences. However, data exists for all segments in the form of single time points from a set of embryos. The estimates for *f* based on the data for each segment are shown here in their entirety in Fig. B-2, separated by segment and plotted as a function of estimated percent completion of germband retraction.
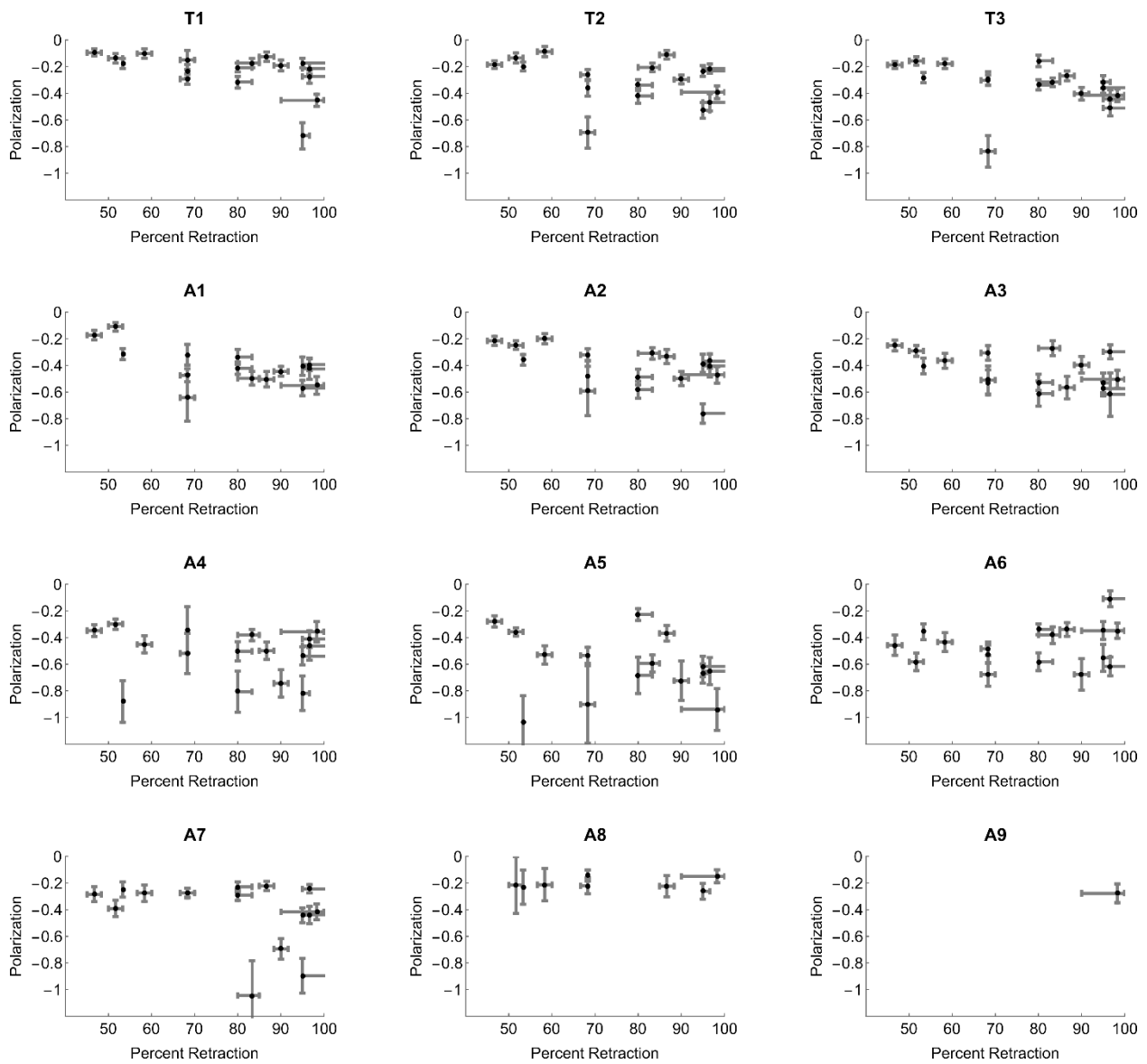
Fig. B-2. Polarization values estimated from nonlinear fits of beta-theta data for single time points from different embryos. Time is plotted as the percentage of germband retraction completed.

The data for most of the segments shows a distinct downward trend over time, indicating increasing polarization. Also, the crook segments around A5 (shown in the third row of Fig. B-2) show the highest magnitude of polarization. This localized increase in polarization agrees with previous observations that the amnioserosa visibly pulls on the germband in this crook area and that wounds in crook segments expand vertically, suggesting that they might experience more external force and perhaps proportionally more internal polarization (Schöck and Perrimon, 2002; Lynch et al., 2013).
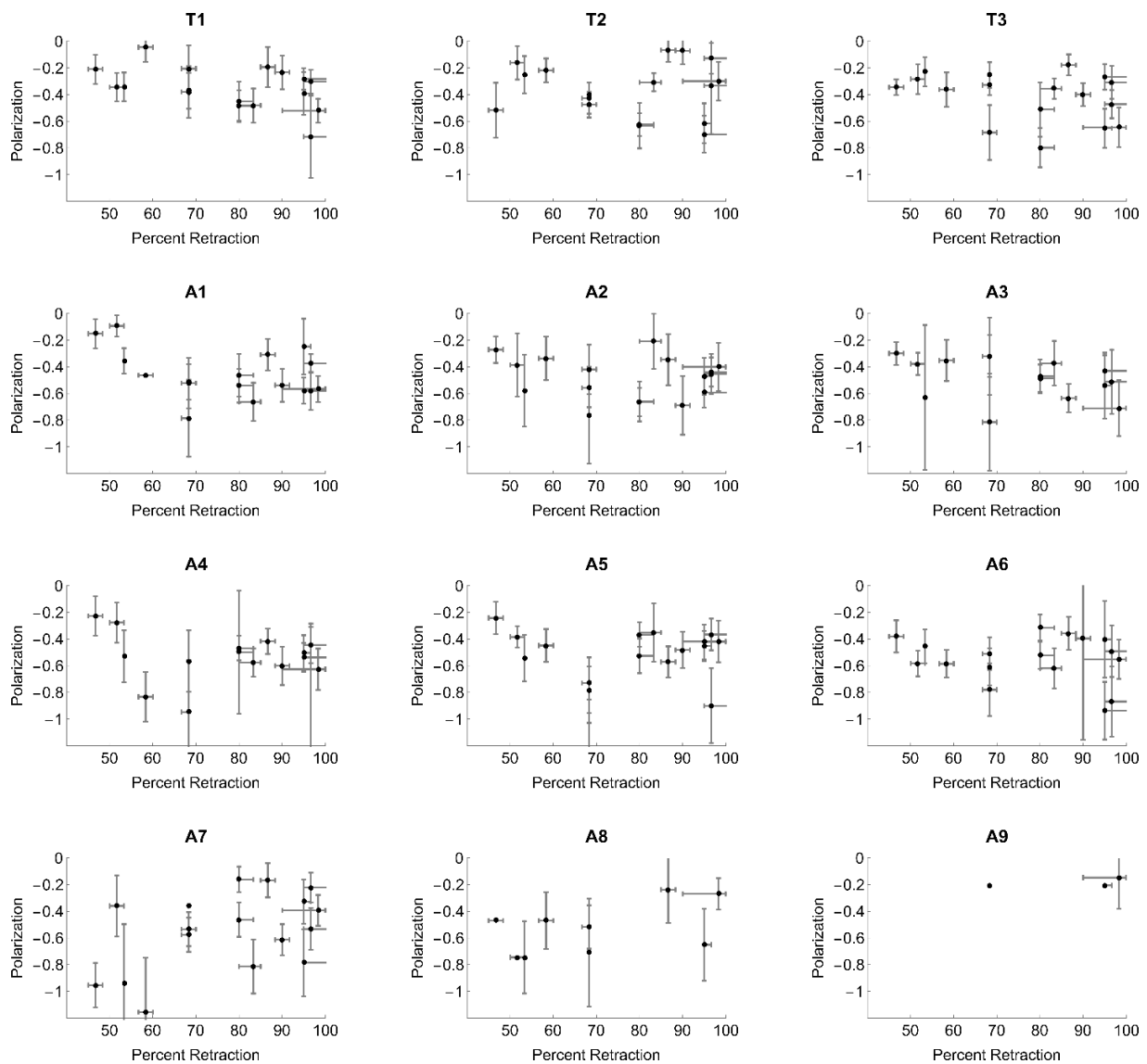
Fig. B-3. Polarization values as calculated from nonlinear fits of CellFIT tensions for single time points from different embryos.

Similar plots were created for the same images of each segment for values of *ƒ* calculated from

the relative tensions estimated by CellFIT, a force-inference method described in Chapter 4 (Brodland et

al., 2014). This provides a check for the beta-theta results, providing polarization values from fits for the

tensions in the CellFIT meshes. As Fig. B-3 shows, these plots demonstrate a much less marked

difference between the crook and non-crook segments, but the crook segments still show the strongest

polarization values. Again, most segments also show a downward trend (stronger polarization) over

time.
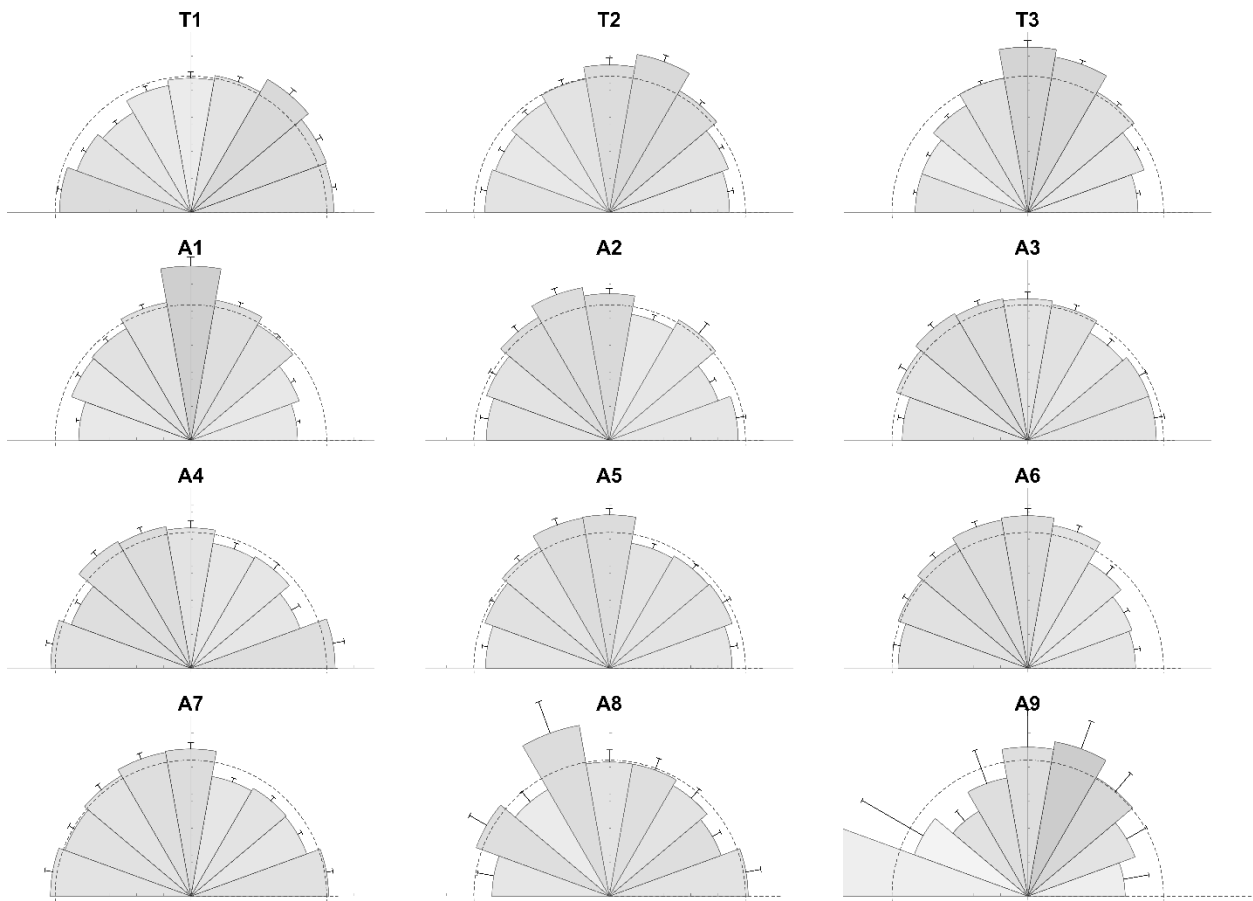
Fig. B-4. Plots of edge tension from all CellFIT meshes for each segment. Each dataset has been rotated so that the direction of composite elongation is vertical before combining. Length of wedges represents average tensions of edges aligned in each sector; grayscale represents fraction of total edges that are aligned in that direction.

Another way to look at this data is in terms of the direction and strength of the edge tensions themselves; this is shown here both as the direct output of CellFIT and as calculated from the composite values of f found for each segment by beta-theta analysis. The longest wedges in the plots in Fig. B-4 represents the highest average CellFIT-calculated edge tensions, which are aligned roughly vertically (toward the amnioserosa) for most segments, some more strongly than others. The darker wedges, representing a larger fraction of edges aligned in that direction, also mostly correspond to vertical edges, with some divergences from this pattern (most notably segments T1 and A4). Similar sector plots of edge tension calculated from the polarizations found by beta-theta analysis show much more vertically centered high tensions in all segments and larger vertically-aligned fractions of all cell edges (Fig. B-5).

The plots in Fig. B-5 represent the tensions calculated from composite values of f for each segment, which I found through both beta-theta analysis and CellFIT, in addition to the plots of polarization for individual time points shown in Figs. B-2 and B-3. These composite f values are shown in Table B-1, allowing a side-by-side comparison of beta-theta and CellFIT results. The composite values from beta-theta and CellFIT analysis agree generally with their respective plots as seen in Figs. B-2 and B-3; for beta-theta, anisotropy increases moving toward the crook segments, with A5 showing the strongest anisotropy, while CellFIT shows no such strong pattern and no dominance of the crook segments. As noted in Chapter 4, however, neither of the methods used to fit these collections of single time points agrees fully with the details of the time-sequence plots for segments A3, A5, and A8.

Figure 4-3 shows the interpolated values for external stress anisotropy found from Lynch et al.'s simulated parameter space (2014), but there are other ways to compare the experimental data to these previous simulations. One measure of comparison with previous work with anisotropy parameter space is the cell aspect ratios. Following Lynch et al.'s example, Fig. B-6 shows plots of aspect ratios for all cells in each segment, which can be compared to their simulated distributions.
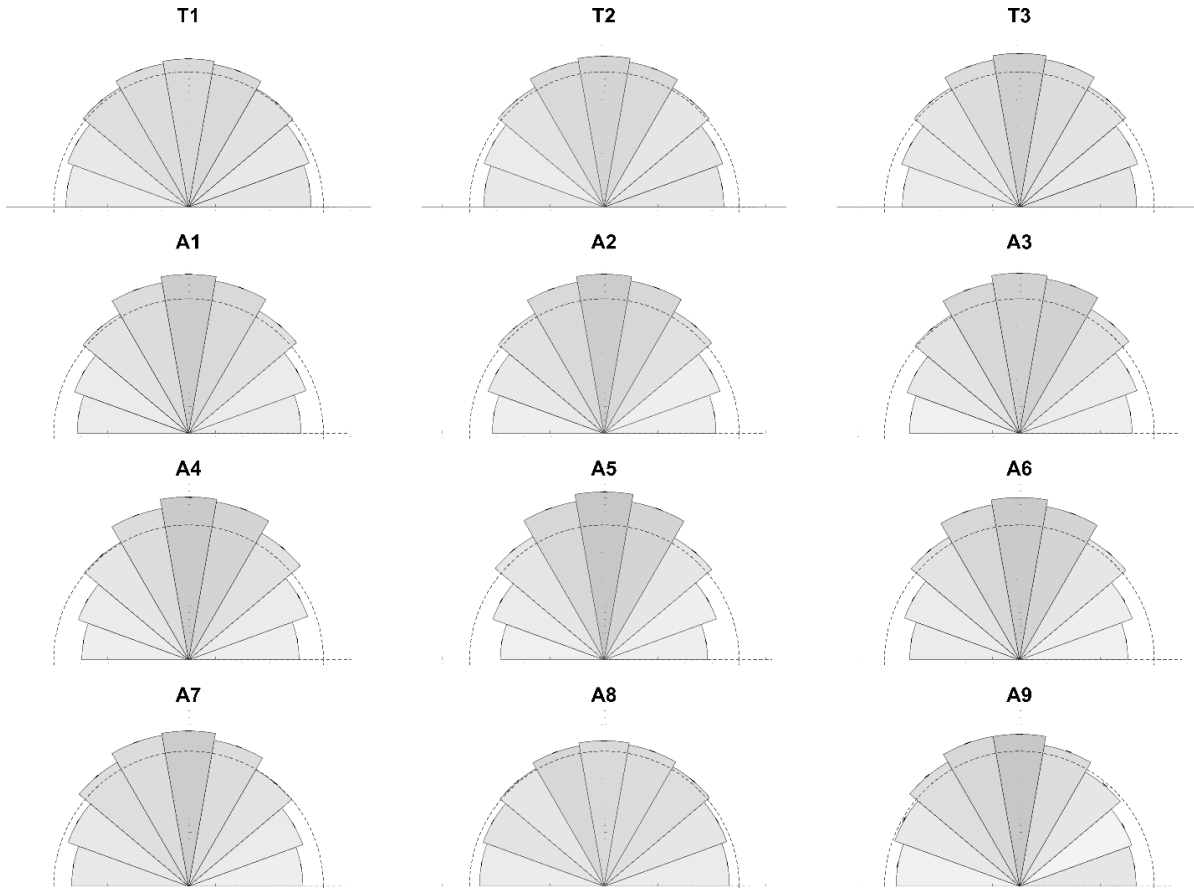
Fig. B-5. Plots of edge tension calculated using the polarization found from the composite nonlinear fit for each segment. Like the CellFIT data, each dataset has been rotated so that the direction of composite elongation is vertical before combining. Length of wedges represents average tensions of edges aligned in each sector; grayscale represents fraction of total edges that are aligned in that direction.

Segment	$f(\beta-\theta)$	f (CellFIT)
T1	-0.20 ± 0.01	-0.22 ± 0.04
T2	-0.24 ± 0.01	-0.25 ± 0.04
T3	-0.28 ± 0.01	-0.38 ± 0.03
A1	-0.36 ± 0.01	-0.37 ± 0.04
A2	-0.37 ± 0.01	-0.21 ± 0.05
A3	-0.38 ± 0.02	-0.16 ± 0.05
A4	-0.43 ± 0.02	-0.10 ± 0.05
A5	-0.50 ± 0.02	-0.20 ± 0.04
A6	-0.41 ± 0.01	-0.30 ± 0.04
A7	-0.31 ± 0.01	-0.15 ± 0.04
A8	-0.16 ± 0.02	-0.20 ± 0.13
A9	-0.28 ± 0.07	-0.15 ± 0.23

Table B-1. Composite polarization for the combined angle data and tension mesh data of all embryos for each segment.
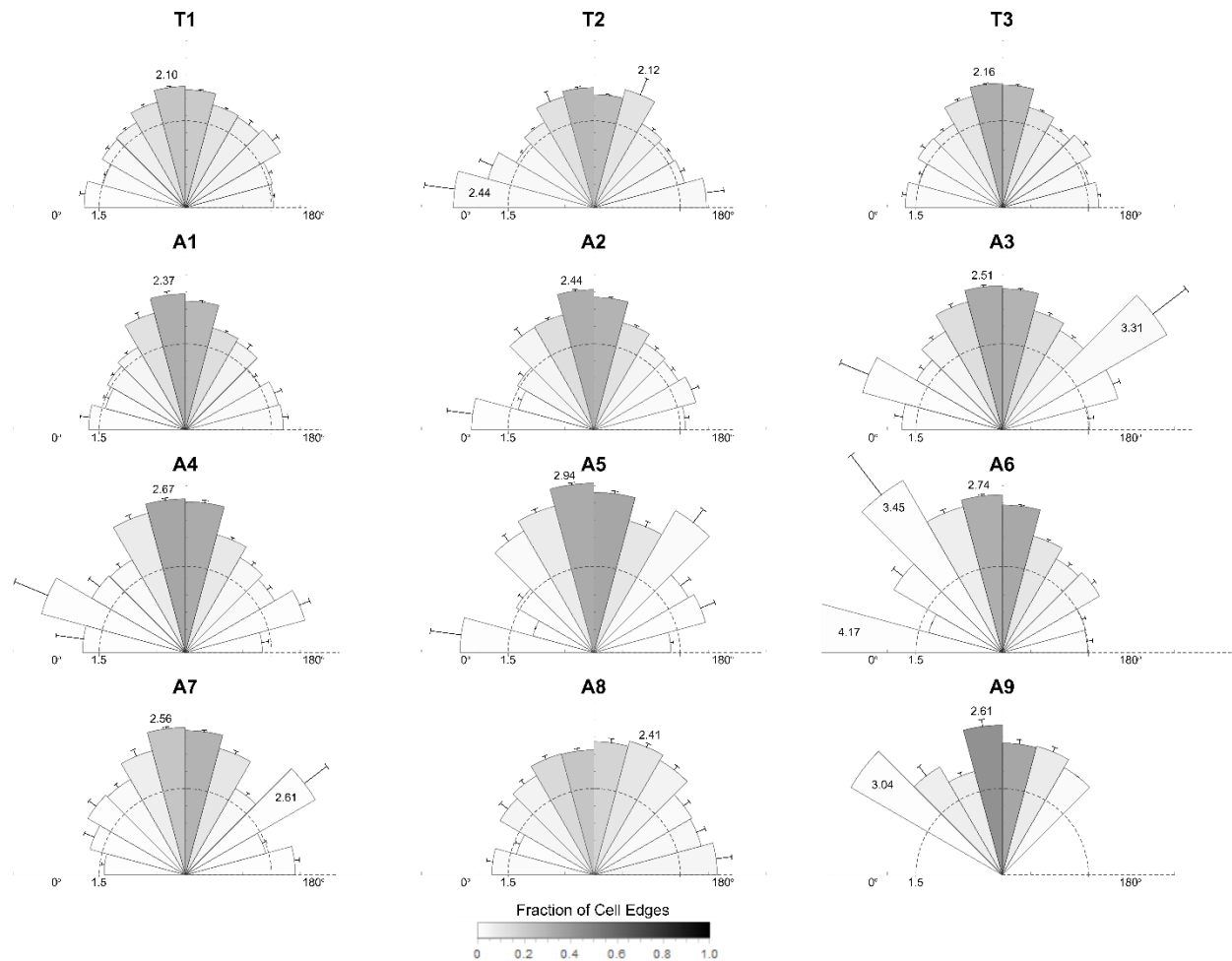
Fig. B-6. Distributions of aspect ratios and alignments for all cells within a segment, taken from all embryos imaged. Note that all segments show strong alignments and significantly higher mean aspect ratios in the vertical direction. Where the highest mean aspect ratio appears in a segment with a very low fraction of cell edges, both the highest value and the highest value in a high-fraction sector are shown.

The angular distribution of cell elongation axes is more dramatic than the edge tension plots, in both the difference in aspect ratio between the vertical and horizontal angle sectors and the fraction of cells in each segment that are vertically elongated (shown in grayscale). Note that the shading is much more concentrated in the more vertical sectors than it was for either set of edge-tension plots; of necessity, the cells themselves are more strongly aligned than their edges, which must still have a variety of orientations. For comparison with this data, Fig. B-7 reproduces Lynch et al.'s simulated aspect ratio and orientation plots for chosen best-fit values of polarization and stress anisotropy, with their initial experimental comparison.
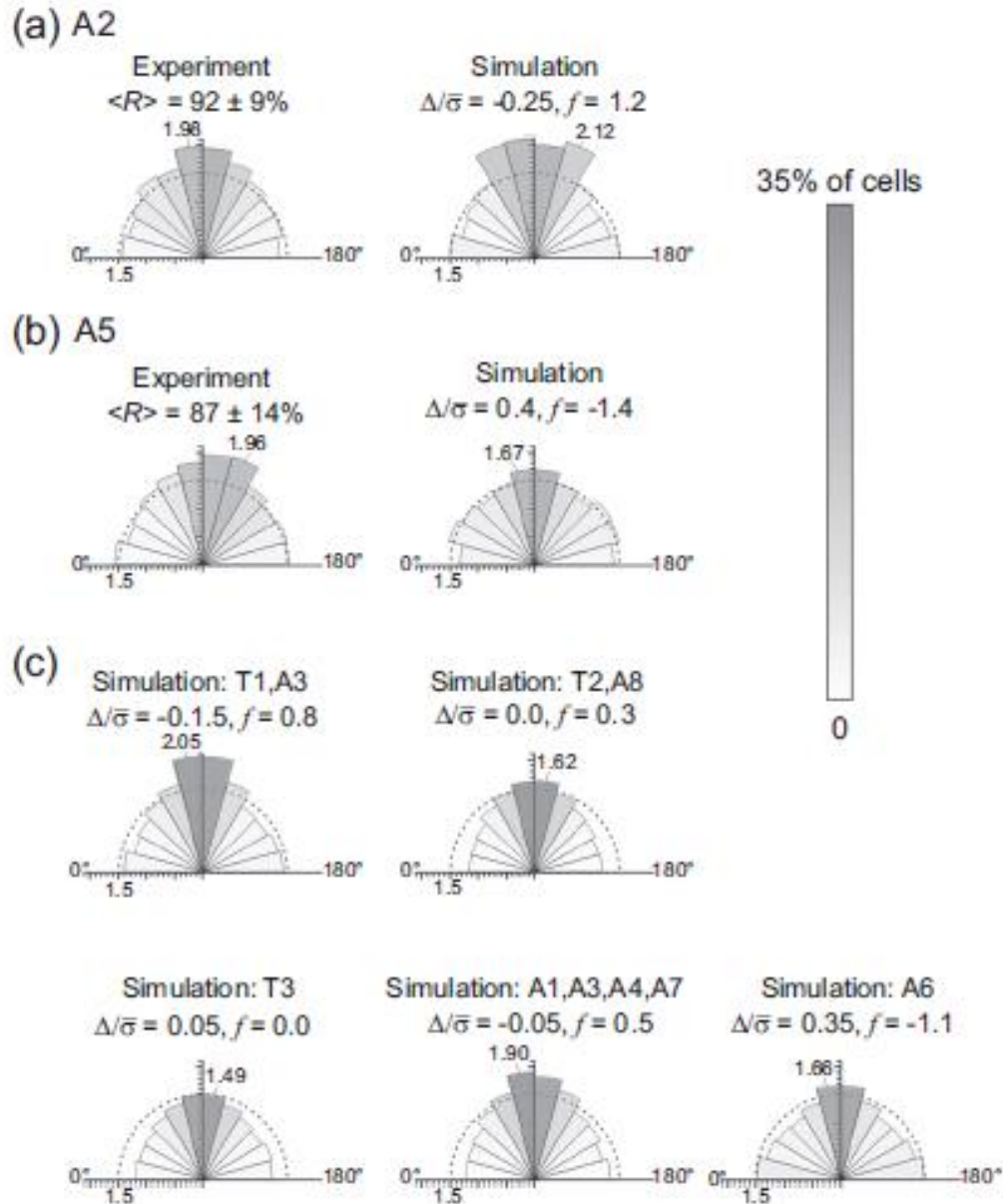
Fig. B-7. Lynch et al.'s simulated aspect ratio and orientation distributions for cell sheets created with the best-fit internal and external anisotropy values for each segment. Experimental plots for segments A2 and A5 were provided for comparison. Reproduced with permission from Lynch et al. (2014).

Comparing these simulated distributions with the experimental composite aspect ratio plots of Fig. B-6, we see that in general the experimental composite plots have much higher cell aspect ratios, not only in the sectors with the most elongated cells but in all sectors (compare the length of the experimental and simulated wedges to the dotted line at κ=1.5 in both figures). This difference is also

visible between our results and the two plots for A2 and A5 included with Lynch et al.'s simulations; the discrepancy is especially interesting since the data for these two segments is shown to be from late germband retraction, when we would expect the cellular aspect ratio to be higher than the average of many time points, not lower. Notwithstanding this difference between the experimental and simulated plots, the fractions of vertically aligned cells at least are comparable, as seen in the grayscale shading of the wedges closest to 90°.

Lastly, Lynch et al.'s best fits for parameter pairs were based on reproducing wound expansion that occurred in embryos at an average of 36% germband retraction. To compare the trajectory of polarization vs. stress anisotropy seen in Fig. 4-3(A) for the time sequences in A3, A5, and A8, I overlaid the simulated best-fit coordinates for each segment with the interpolated coordinate pair for t=40 min, which was staged at about 40% of germband retraction. Figure B-8 shows that each of these coordinates, shown as black dots, falls approximately in the line of possible simulated best fits, but the trajectory of the subsequent interpolation diverges from the line similarly in all three cases.
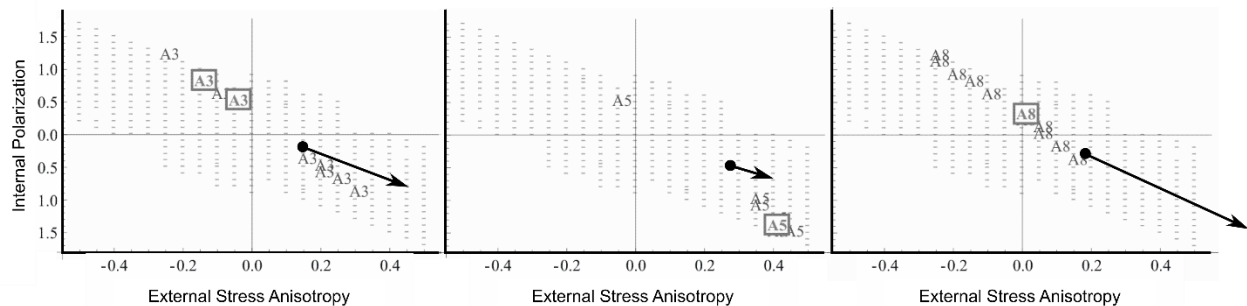
Fig. B-8. Interpolated points compared to simulated fits for polarization vs. stress anisotropy. Background simulation fits reproduced with permission from supplementary information for Lynch et al. (2014).

This divergence is likely due to the more complete data provided by the time sequence, which yielded not only polarization but also changing aspect ratios over time. As κ changes, the contour along which the associated anisotropy coordinates lie changes as well. These three plots are an example of the

improved data and anisotropy estimates we can expect from analyzing time sequences of all segments, replacing the previous generalized assumptions with specific data that reflects the differences between the individual germband segments.

Appendix C: Investigating Amnioserosal Crawling with Photoactivatable Proteins

For biophysicists, one of the most important aspects of morphogenesis, as well as general tissue response to external stimulus, is structural change in individual cells and the effect on the tissue as a whole. Changes in cellular structure are often due to actin, a protein that polymerizes to form filaments that contract or extend through cross-linking with motor proteins such as myosin II (Hibberd and Trentham, 1986; Pollard and Cooper, 1986). The various structures formed in this way underlie features often observed in single cells, such as lamellipodia (broad, flat cellular protrusions) and filopodia (thin, spiky protrusions) (Ridley et al., 1992). Although the functions of actin and the upstream signaling networks that regulate actin polymerization and recruitment have been studied extensively in some organisms, the protein homologs in other species do not always behave and interact in the same way. Thus the broad understanding of actin's function can transfer to *Drosophila* studies, but the details of the signaling involved may vary from previously known networks.

Actin recruitment and organization is directed in different ways for different structures; one family of proteins that is heavily implicated in several cytoskeletal functions is the small Rho GTPases. This family includes RhoA, which regulates stress fibers and focal adhesions (Ridley and Hall, 1992); Rac1, which is known to regulate lamellipodial formation in single cells (Ridley et al., 1992); and Cdc42, which is involved in filopodial regulation (Nobes and Hall, 1995). The cytoskeletal functions of these GTPases are of particular interest in studying the morphogenetic stages of germband retraction and dorsal closure. During germband retraction, the dorsal bridge of the amnioserosa overlaps the posterior end of the germband, with observed lamelliopodium-like projections at the dorsal midline (Schöck and Perrimon, 2002). In the following events of dorsal closure, the dorsal epidermis migrates over the amnioserosa with the help of more lamellipodium-like projections at the leading edge, and the opposite edges match up and fuse together with the aid of filopodia (Jacinto et al., 2000). The work described

72

here was proposed to investigate these cellular projections in terms of the roles of the Rho GTPases, to better understand the networks that govern actin regulation in *Drosophila*.

One relatively recent development in *Drosophila* research that has offered promise in investigating small GTPases in development is the creation of stable strains of photoactivatable proteins. Photoactivation is achieved by fusing the light-oxygen-voltage (LOV) domain of *Avena sativa* (wild oat) phototropin with a desired protein, in this case the *Drosophila* homolog of the small GTPase Rac1 (Wu et al., 2009). Rac1's activity in *Drosophila* cells can be controlled by exposure to blue light (approximate range 400-500 nm, peak absorption at 473 nm), which produces a reversible effect with a dark recovery half-life of 43 s (Wu et al., 2009). This effect was used to temporarily activate PA-Rac1 in polar cells in *Drosophila* oogenesis, targeting regions of a cell or group of collectively moving cells, which increased cell protrusions and movement in the region targeted. Similarly, activation of the dominant-negative form of PA-Rac1 slowed movement in the direction of the targeted region and caused protrusion and movement in the opposite direction (Wang et al., 2010). For this work, I obtained *Drosophila* strains from the lab of Denise Montell, expressing constitutively active (Q61L), dominant-negative (E17N), and light-insensitive (C450M) forms of photoactivatable Rac1 (PA-Rac1) on multiple chromosomes. Figure C-1 shows the placement of the LOV domain and attached Jα-helix, which prevent Rac1 activation until they are irradiated by the correct wavelength.
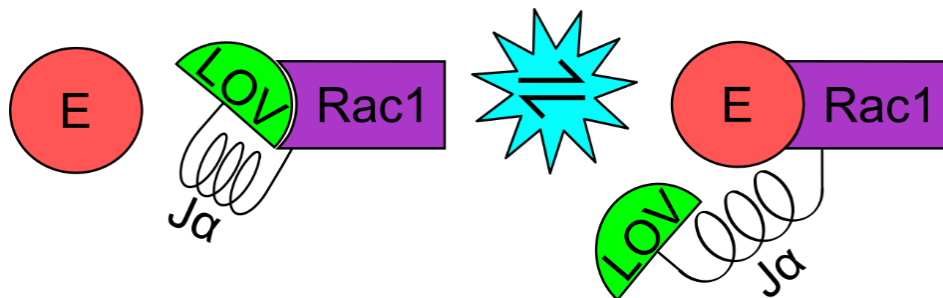
Fig. C-1. Conformation of photoactivatable Rac1 before and during irradiation. In the dark state, the LOV domain blocks Rac1's effector site, keeping the effector (E) from binding to Rac1. The Jα-helix unwinds when the protein complex is exposed to light between 400 and 500 nm, unblocking the Rac1 effector site and allowing E to bind with Rac1. Note that the double arrows indicate the reversibility of the light-state unwinding.

For the purposes of investigating its role in the amnioserosa, PA-Rac1 expression was confined to the amnioserosa by crossing the PA-Rac1 strains with particular GAL4 drivers. The GAL4-UAS system is described briefly in Chapter 3, and provides a way to limit expression of a desired gene to a specific part of the fly; to facilitate precision in expression, all the photoactivatable stocks I obtained were already UAS-tagged for use with GAL4 drivers. Since I originally proposed to study the Rho GTPases in embryonic dorsal closure, I chose two GAL4 drivers, one for ubiquitous embryonic expression and one for expression in the amnioserosa during dorsal closure (obtained from Bloomington *Drosophila* Stock Center). Both GAL4 drivers were crossed with constitutively active and dominant-negative strains of PA-Rac1, totaling four cross strains to express each type of PA-Rac1 either ubiquitously or in the amnioserosa/lateral epidermis region during dorsal closure.

To effectively carry out experiments with PA-Rac1, it was necessary to use a microscope that could provide both fluorescent imaging and more targeted illumination at the correct wavelength. This combination was achieved with a spinning-disk microscope, which somewhat reduces imaging contrast compared to traditional confocal imaging but offers the advantage of increased speed. The spinning-disk microscope used for these experiments also had a 405 nm ablation laser which fell within the required range of 400-500 nm and was used at very low power to provide targeted illumination.

In addition to imaging the cell membranes, we needed in this case to also visually track active Rac1. In initial studies with HeLa cells, PA-Rac1 was tagged with YFP to track Rac1 motion (Wu et al., 2009). The PA-Rac1 *Drosophila* strains I obtained were tagged with mCherry instead; both choices avoid the problems inherent in using GFP, which fluoresces in a wavelength range that might lead to accidental photoactivation during imaging. For these experiments, mCherry was also used with a membrane marker to delineate cell membranes and combined with the ubiquitous GAL4 driver. This double tagging

with mCherry made it difficult to distinguish the activated PA-Rac1 from the membranes, necessitating a focus on detecting changes in movement rather than new fluorescence as a result of photoactivation.

Although I had initially planned to carry out experiments on embryos in dorsal closure, the relative complexity of the factors in the germband's leading edge during this stage prompted me to begin instead with germband retraction. Thus, the PA-Rac1 experiments discussed here focused on the dorsal bridge of the amnioserosa, the posterior end of which maintains contact with the caudal end of the germband and crawls posteriorly over the caudal cells as the germband retracts. This crawling is accompanied and thought to be aided by the presence of projections resembling lamellipodia (Fig. C-2) (Schöck and Perrimon, 2002), which are associated with Rac1 function as mentioned earlier (Ridley et al., 1992). I hypothesized that using the spatial and temporal control offered by photoactivation, I could investigate the relationship between Rac1 activity at the posterior edge of the amnioserosa dorsal bridge and its crawling speed.
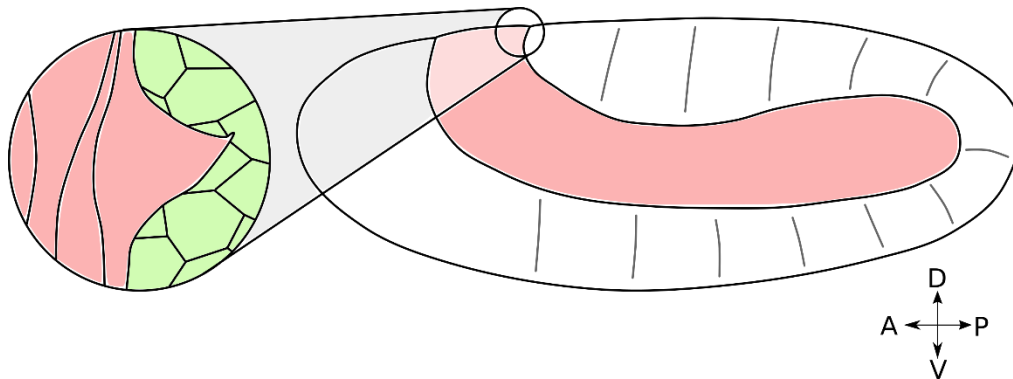
Fig. C-2. View of crawling dorsal lamellipodium and location relative to the rest of the embryo. The embryo shown here is at the beginning of germband retraction, so the germband cells visible under the crawling amnioserosa edge are not yet elongated.

To produce the most dramatic effect possible in spite of the non-ideal fluorophore combination, I used the dominant-negative form of PA-Rac1 (hereafter referred to as PA-DN-Rac1), hypothesizing that I would see a reduction in the crawling speed as the lamellipodia at the leading edge retracted. Possible

appropriate photoactivation protocols were limited by the capabilities of the Mosaic laser used with the 60x oil objective on the spinning-disk microscope, which limited accurate targeting to about the middle 50% of the field of view. Another limitation of the equipment was the inability to take images concurrently with Mosaic illumination, making it impossible to both photoactivate the tissue constantly over a period of minutes and record any immediate reaction. To approximate the effects of constant illumination over a period of time, I created a protocol that alternated between 15 seconds of illumination at 405 nm and approximately 5 seconds of imaging at 568 nm, spanning 5 planes 2 µm apart. This alternation continued for 500 seconds, after which the embryo was imaged for another 400 seconds while the PA-Rac1 ostensibly recovered and returned to its dark state. Controls in embryos with and without PA-DN-Rac1 were imaged for the same amount of time, with intermittent imaging according to the same timing as the photoactivation protocol, but with Mosaic power set to zero for the PA-DN-Rac1 controls. In all embryos, half of the leading edge was targeted for Mosaic illumination and half was left unilluminated.

Photoactivating PA-DN-Rac1 produced modest but measurable effects; amnioserosal crawling was not totally arrested in any cases, but the speed was reduced during Mosaic illumination. For N=16 embryos in which PA-DN-Rac1 was photoactivated, the difference between average crawling speeds during and before illumination was -7.10 nm/s in the targeted portion of the leading edge (P=0.01) and -6.24 nm/s in the untargeted portion of the leading edge (P=0.06). For N=10 PA-DN-Rac1 controls, the differences in speed were -0.50 nm/s (P=0.19) and -0.10 nm/s (P=0.68). For N=11 controls without PA-DN-Rac1, the differences in speed were -0.136 µm/s (P=0.34) and -71.2 nm/s (P=0.34). The visible difference between the targeted and untargeted data in the photoactivated embryos and controls is shown in Fig. C-3, which plots the averages of measurements of displacement of a point on the leading edge over the same period of time for targeted and untargeted regions of the same edge.
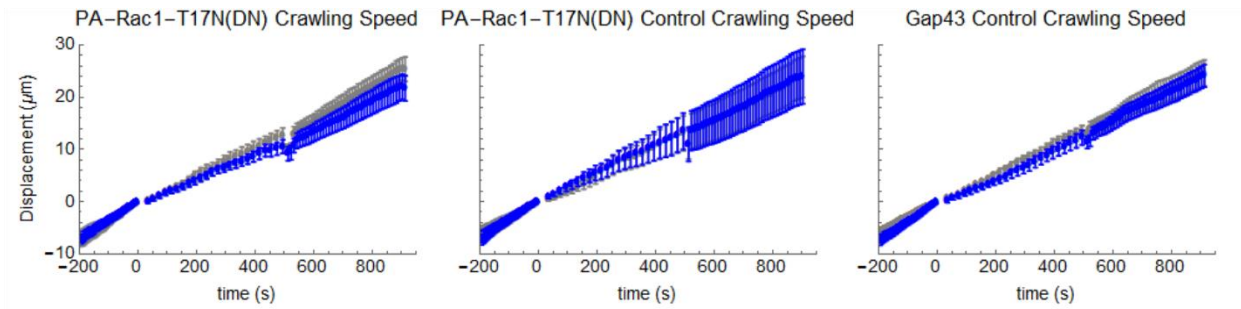
Fig. C-3. Averages of amnioserosa leading edge crawling speed (shown as displacement vs. time) for embryos expressing dominant-negative PA-Rac1, both with targeted Mosaic illumination and without as a control, and for embryos without PA-Rac1 as a second control. Blue and gray points represent averages of targeted and untargeted portions of the leading edge within the same set of embryos.

The differences in leading edge speed before, during, and after the period of illumination in embryos with photoactivated PA-DN-Rac1 are shown in more detail in Fig. C-4, which shows that in most embryos, the amnioserosal crawling speed was higher before illumination than during the 500 seconds or even afterward, during the 400 seconds in which it recovers from photoactivation.
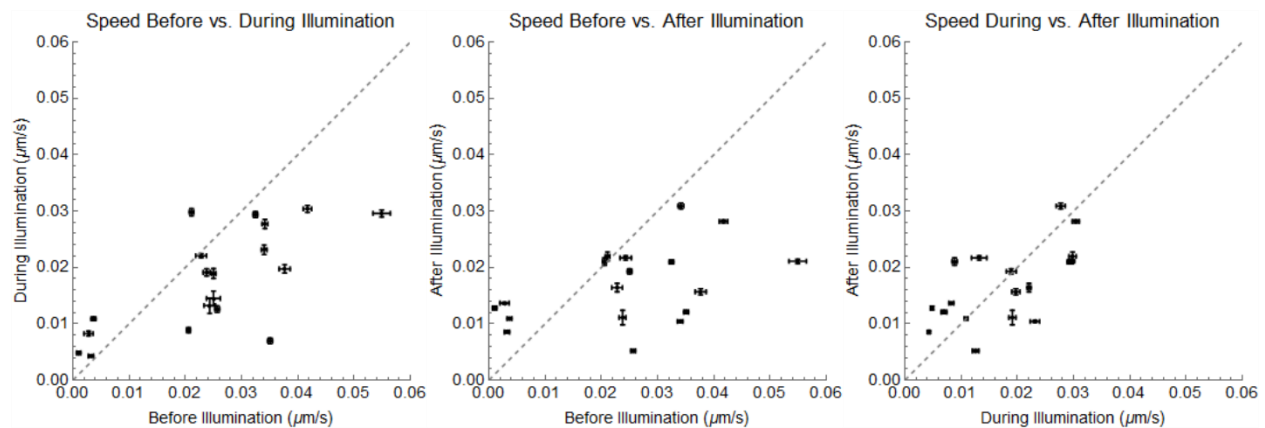
Fig. C-4. Comparison of amnioserosal edge crawling speed for single PA-DN-Rac1 embryos before, during, and after photoactivation. For crawling speed before vs. during photoactivation, P=0.004.

To further characterize the effect of Rac1 on the dorsal crawling and the associated lamellipodial formation, I attempted to measure the area of the lamellipodial protrusions in the region of illumination. However, tracking the area of the lamellipodia proved impractical in this application due to the quality of imaging of the visible membranes and the inherent difficulty of assigning and tracking a location for the

base of the lamellipodia. The results of these attempts show no clear trend in the size of lamellipodia, and the constantly fluctuating membrane edge complicates any further analysis.

Conclusions

Although I did not directly quantify the activation of PA-Rac1 in the amnioserosa, my results show a decrease in crawling speed of the amnioserosal leading edge when the dominant-negative version of PA-Rac1 is activated. This provides evidence of Rac1's role in leading edge motility, adding credence to the hypothesis that it is instrumental in regulating the lamellipodium-like projections that are visible as the amnioserosa crawls over the germband. Interestingly, Fig. C-4 shows that crawling does not return to pre-photoactivation speeds during the 400 s of recovery time, suggesting that the 43 s half-life recovery time is not sufficient for the leading edge to recover its lost speed. Further experiments that measure crawling speed of the leading edge later in retraction would help determine whether the decreased speed persists beyond the limits of my imaging protocol. Another useful metric to incorporate into future experiments is the measurement of photoactivation strength or efficacy, based on being able to distinguish the fluorescence of activated PA-Rac1 from its surroundings.

Future work with similar GTPase constructs could also focus on the subsequent developmental stage of dorsal closure, which was the developmental stage of interest in my original plans to combine photoactivatable proteins with embryonic GAL4 expression. Like germband retraction, dorsal closure features a leading edge of cells moving over another tissue, in this case the germband moving over the amnioserosa rather than the other way around. As described in Chapter 2, in addition to an actomyosin cable, the leading edge also features lamellipodia, which may help with migration, and filopodia, which help match up the segments from opposite sides of the leading edge as they join (Jacinto et al., 2000; Jacinto et al., 2002a). The ability to investigate the GTPases that are thought to be responsible for

regulating these features using the precise and reversible spatial and temporal control offered by photoactivatable proteins would be a great asset in future research.

My work with photoactivatable proteins, though relatively modest in scope, has demonstrated that optogenetics is a useful tool for biophysics investigations. Encouragingly, more recent experiments have met with success in *Drosophila* embryos undergoing ventral furrow formation, in which researchers successfully targeted a membrane protein upstream of cortical actin and inhibited apical constriction in ventral midline cells (Guglielmi et al., 2015). In this case, photoactivation occurred with illumination times of about 1 second, testifying to the wide variety of possible protocols that may be useful for future use of photoactivatable proteins in various developmental contexts. Guglielmi et al. also made use of two-photon microscopy to improve the precision of their targeted illumination, allowing increased control over the photoactivated area (2015). Although this specific setup is not available in all cases, improvements in imaging capabilities and the quality and convenience of optogenetic constructs will make such projects increasingly feasible for a variety of laboratory environments.

Methods

Crossing and Mounting

The process of creating crosses for this experiment has been described in Chapter 3. Embryos were obtained from the Montell lab that were homozygous for a UAS-linked dominant-negative PA-Rac1 on the second chromosome; a separate strain with a ubiquitous embryonic GAL4 driver was ordered from the Bloomington *Drosophila* Stock Center and crossed through several generations with a strain containing a fluorescent gap43 membrane marker. The resulting stable strain was continually crossed with the UAS-DN-PA-Rac1 strain rather than permanently combining the two, and the offspring were used directly in the experiment. Collected embryos were aged until the pause after germband retraction when the germband can be observed at full extension, and mounted dorsally as described previously.

Imaging and Targeted Illumination

The slides were imaged on a spinning-disk confocal microscope and illuminated in targeted areas with a 455 nm Mosaic laser at low power. Throughout imaging and illumination, all ambient light was eliminated as much as possible by conducting the experiments in darkness and with foil wrapped around the microscope head and stage. For the crawling speed experiment, the Mosaic laser was targeted at a thin rectangle spanning approximately half of the field of view to the left or right of the dorsal midline, corresponding to the position of the leading edge of the amnioserosal dorsal bridge at the onset of illumination. The division of targeted and untargeted halves allowed later tracking of the leading edge on both sides for the same embryo during image processing, so that fair comparisons could be made. For the projection area experiment, the Mosaic laser was targeted at a rough polygon approximating the shape of the lamellipodial projection visible at the dorsal midline on the leading edge.

To approach as close as possible to constant illumination while still recording the effect on the amnioserosa, I developed a protocol that collected images for 100 seconds before Mosaic illumination, then waited for a period to allow drawing of the target area, and thereafter interspersed fifteen seconds of Mosaic illumination with approximately five seconds of imaging to obtain several planes of depth. This alternation continued for 500 seconds, after which I continued to record images to observe the effect of the return to the dark state.

REFERENCES

2016. Mathematica. In. Mathematica: Wolfram Research, Inc.

Araujo H, Bier E. 2000. *sog* and *dpp* exert opposing maternal functions to modify toll signaling and pattern the dorsoventral axis of the *Drosophila* embryo. Development 127:3631-3644.

Arora K, Nusslein-Volhard C. 1992. Altered mitotic domains reveal fate map changes in *Drosophila* embryos mutant for zygotic dorsoventral patterning genes. Development 114:1003-1024.

Ashe HL, Mannervik M, Levine M. 2000. Dpp signaling thresholds in the dorsal ectoderm of the *Drosophila* embryo. Development 127:3305-3312.

Azevedo D, Antunes M, Prag S, Ma X, Hacker U, Brodland GW, Hutson MS, Solon J, Jacinto A. 2011. DRhoGEF2 regulates cellular tension and cell pulsations in the amnioserosa during *Drosophila* dorsal closure. PLOS ONE 6:e23964-e23964.

Belacortu Y, Paricio N. 2011. *Drosophila* as a model of wound healing and tissue regeneration in vertebrates. Developmental Dynamics.

Bertet C, Sulak L, Lecuit T. 2004. Myosin-dependent junction remodelling controls planar cell intercalation and axis elongation. Nature 429:667-671.

Blanchard GB, Murugesu S, Adams RJ, Martinez-Arias A, Gorfinkiel N. 2010. Cytoskeletal dynamics and supracellular organisation of cell shape fluctuations during dorsal closure. Development 137:2743-2752.

Blankenship JT, Backovic ST, Sanny JSP, Weitz O, Zallen JA. 2006. Multicellular rosette formation links planar cell polarity to tissue morphogenesis. Developmental Cell 11:459-470.

Bothma JP, Levine M, Boettiger A. 2010. Morphogen gradients: limits to signaling or limits to measurement? Current Biology 20:R232--R234.

Brodland GW, Chen DIL, Veldhuis JH. 2006. A cell-based constitutive model for embryonic epithelia and other planar aggregates of biological cells. International Journal of Plasticity 22:965-995.

Brodland GW, Conte V, Cranston PG, Veldhuis J, Narasimhan S, Hutson MS, Jacinto A, Ulrich F, Baum B, Miodownik M. 2010. Video force microscopy reveals the mechanics of ventral furrow invagination in *Drosophila*. Proceedings of the National Academy of Sciences of the United States of America 107:22111-22116.

Brodland GW, Veldhuis JH, Kim S, Perrone M, Mashburn D, Hutson MS. 2014. CellFIT: A Cellular Force-Inference Toolkit Using Curvilinear Cell Boundaries. PLOS ONE 9:e99116.

Brodland GW, Viens D, Veldhuis JH. 2007. A new cell-based FE model for the mechanics of embryonic epithelia. Comput Methods Biomech Biomed Engin 10:121-128.

Brodland GW, Wiebe CJ. 2004. Mechanical effects of cell anisotropy on epithelia. Comput Methods Biomech Biomed Engin 7:91-99.

Brody T. 1999. The Interactive Fly: gene networks, development and the Internet. Trends Genet 15:333-334.

Butler LC, Blanchard GB, Kabla AJ, Lawrence NJ, Welchman DP, Mahadevan L, Adams RJ, Sanson B. 2009. Cell shape changes indicate a role for extrinsic tensile forces in *Drosophila* germ-band extension. Nature Cell Biology 11:859-864.

Canty EG, Garrigue-Antar L, Kadler KE. 2006. A complete domain structure of *Drosophila* Tolloid is required for cleavage of Short gastrulation. Journal of Biological Chemistry 281:13258-13267.

Colas J-F, Launay J-M, Maroteaux L. 1999a. Maternal and zygotic control of serotonin biosynthesis are both necessary for *Drosophila* germband extension. Mechanisms of Development 87:67-76.

Colas J-F, Launay J-M, Vonesch J-L, Hickel P, Maroteaux L. 1999b. Serotonin synchronises convergent extension of ectoderm with morphogenetic gastrulation movements in *Drosophila*. Mechanisms of Development 87:77-91.

Cormier O, Mohseni N, Voytyuk I, Reed BH. 2012. Autophagy can promote but is not required for epithelial cell extrusion in the amnioserosa of the *Drosophila* embryo. Autophagy 8:252-264.

Crews SM, McCleery WT, Hutson MS. 2015. Pathway to a phenocopy: heat stress effects in early embryogenesis. Developmental Dynamics:000-000.

Créton R, Kreiling JA, Jaffe LF. 2000. Presence and roles of calcium gradients along the dorsal-ventral axis in *Drosophila* embryos. Developmental Biology 217:375-385.

Decotto E, Ferguson EL. 2001. A positive role for Short gastrulation in modulating BMP signaling during dorsoventral patterning in the *Drosophila* embryo. Development 128:3831-3841.

Dorfman R, Shilo B-Z. 2001. Biphasic activation of the BMP pathway patterns the *Drosophila* embryonic dorsal region. Development 128:965-972.

Duffy JB. 2002. GAL4 system in *Drosophila*: a fly geneticist's Swiss army knife. Genesis 34:1-15.

Eberlein S. 1986. Stage specific embryonic defects following heat shock in *Drosophila*. Developmental Genetics 6:179-197.

Edgar BA, O'Farrell PH. 1989. Genetic control of cell division patterns in the *Drosophila* embryo. Cell 57:177-187.

Falciani F, Hausdorf B, Schröder R, Akam M, Tautz D, Denell R, Brown S. 1996. Class 3 Hox genes in insects and the origin of *zen*. Proceedings of the National Academy of Sciences 93:8479-8484.

Ferguson EL, Anderson KV. 1992. *decapentaplegic* acts as a morphogen to organize dorsal-ventral pattern in the *Drosophila* embryo. Cell 71:451-461.

Fernandez-Gonzalez R, Zallen JA. 2009. Cell mechanics and feedback regulation of actomyosin networks. Science Signaling 2:pe78-pe78.

Fernández BG, Arias AM, Jacinto A. 2007. Dpp signalling orchestrates dorsal closure by regulating cell shape changes both in the amnioserosa and in the epidermis. Mechanisms of Development 124:884-897.

Figard L, Xu H, Garcia HG, Golding I, Sokac AM. 2013. The plasma membrane flattens out to fuel cell-surface growth during *Drosophila* cellularization. Developmental Cell 27:648-655.

Fischer SC, Blanchard GB, Duque J, Adams RJ, Arias AM, Guest SD, Gorfinkiel N. 2014. Contractile and mechanical properties of epithelia with perturbed actomyosin dynamics. PLOS ONE 9:e95695-e95695.

Francois V, Solloway M, O'Neill JW, Emery J, Bier E. 1994. Dorsal-ventral patterning of the *Drosophila* embryo depends on a putative negative growth factor encoded by the short gastrulation gene. Genes & Development 8:2602-2616.

Frank LH, Rushlow C. 1996. A group of genes required for maintenance of the amnioserosa tissue in *Drosophila*. Development 122:1343-1352.

Gavin-Smyth J, Wang Y-C, Butler I, Ferguson EL. 2013. A genetic network conferring canalization to a bistable patterning system in *Drosophila*. Current Biology 23:2296-2302.

Goldenberg G, Harris TJC. 2013. Adherens junction distribution mechanisms during cell-cell contact elongation in *Drosophila*. PLOS ONE 8:e79613-e79613.

Gorfinkiel N, Blanchard GB, Adams RJ, Arias AM. 2009. Mechanical control of global cell behaviour during dorsal closure in *Drosophila*. Development 136:1889-1898.

Gorfinkiel N, Schamberg S, Blanchard GB. 2011. Integrative approaches to morphogenesis: lessons from dorsal closure. genesis 49:522-533.

Guglielmi G, Barry Joseph D, Huber W, De Renzis S. 2015. An optogenetic method to modulate cell contractility during tissue morphogenesis. Developmental Cell 35:646-660.

Hamaguchi T, Yabe S, Uchiyama H, Murakami R. 2004. *Drosophila* Tbx6-related gene, *Dorsocross*, mediates high levels of Dpp and Scw signal required for the development of amnioserosa and wing disc primordium. Developmental Biology 265:355-368.

Harden N. 2002. Signaling pathways directing the movement and fusion of epithelial sheets: lessons from dorsal closure in *Drosophila*. Differentiation 70:181-203.

Harris TJC, Sawyer JK, Peifer M. 2009. How the cytoskeleton helps build the embryonic body plan: models of morphogenesis from *Drosophila*. Current Topics in Developmental Biology 89:55-85.

Hartenstein V, Campos-Ortega JA. 1985. Fate-mapping in wild-type *Drosophila melanogaster*. Wilhelm Roux's Archives of Developmental Biology 194:181-195.

Haskel-Ittah M, Ben-Zvi D, Branski-Arieli M, Schejter ED, Shilo B-Z, Barkai N. 2012. Self-organized shuttling: generating sharp dorsoventral polarity in the early *Drosophila* embryo. Cell 150:1016-1028.

Heffer A, Pick L. 2013. Conservation and variation in Hox genes: how insect models pioneered the evo-devo field. Annual Review of Entomology 58:161-179.

Heisenberg C-P. 2009. Dorsal closure in *Drosophila*: Cells cannot get out of the tight spot. Bioessays 31:1284-1287.

Hibberd MG, Trentham DR. 1986. Relationships between chemical and mechanical events during muscular contraction. Annual Review of Biophysics and Biophysical Chemistry 15:119-161.

Hodar C, Zuñiga A, Pulgar R, Travisany D, Chacon C, Pino M, Maass A, Cambiazo V. 2014. Comparative gene expression analysis of *Dtg*, a novel target gene of Dpp signaling pathway in the early *Drosophila melanogaster* embryo. Gene 535:210-217.

Hong J-W, Hendrix DA, Papatsenko D, Levine MS. 2008. How the Dorsal gradient works: insights from postgenome technologies. Proceedings of the National Academy of Sciences 105:20072-20076.

Horn T, Hilbrant M, Panfilio KA. 2015. Evolution of epithelial morphogenesis: phenotypic integration across multiple levels of biological organization. Frontiers in Genetics 6:303.

Huang J-D, Schwyter DH, Shirokawa JM, Courey AJ. 1993. The interplay between multiple enhancer and silencer elements defines the pattern of *decapentaplegic* expression. Genes and Development 7:694-704.

Hutson MS, Tokutake Y, Chang M-S, Bloor JW, Venakides S, Kiehart DP, Edwards GS. 2003. Forces for morphogenesis investigated with laser microsurgery and quantitative modeling. Science 300:145-149.

Hutson MS, Veldhuis J, Ma X, Lynch HE, Cranston PG, Brodland GW. 2009. Combining laser microsurgery and finite element modeling to assess cell-level epithelial mechanics. Biophys J 97:3075-3085.

Irvine KD, Wieschaus E. 1994. Cell intercalation during *Drosophila* germband extension and its regulation by pair-rule segmentation genes. Development 120:827-841.

Jacinto A, Wood W, Balayo T, Turmaine M, Martinez-Arias A, Martin P. 2000. Dynamic actin-based epithelial adhesion and cell matching during *Drosophila* dorsal closure. Current Biology 10:1420-1426.

Jacinto A, Wood W, Woolner S, Hiley C, Turner L, Wilson C, Martinez-Arias A, Martin P. 2002a. Dynamic analysis of actin cable function during *Drosophila* dorsal closure. Current Biology 12:1245-1250.

Jacinto A, Woolner S, Martin P. 2002b. Dynamic analysis of dorsal closure in *Drosophila*: from genetics to cell biology. Developmental Cell 3:9-19.

Jiang J, Cai H, Zhou Q, Levine M. 1993. Conversion of a *dorsal*-dependent silencer into an enhancer: evidence for *dorsal* corepressors. The EMBO Journal 12:3201-3201.

Kanodia JS, Rikhy R, Kim Y, Lund VK, DeLotto R, Lippincott-Schwartz J, Shvartsman SY. 2009. Dynamics of the Dorsal morphogen gradient. Proceedings of the National Academy of Sciences 106:21707-21712.

Keller R, Davidson L, Edlund A, Elul T, Ezin M, Shook D, Skoglund P. 2000. Mechanisms of convergence and extension by cell intercalation. Philosophical Transactions of the Royal Society B: Biological Sciences 355:897-922.

Kiehart DP, Galbraith CG, Edwards KA, Rickoll WL, Montague RA. 2000. Multiple forces contribute to cell sheet morphogenesis for dorsal closure in *Drosophila*. The Journal of Cell Biology 149:471-490.

Kozlova T, Thummel CS. 2003. Essential roles for ecdysone signaling during *Drosophila* mid-embryonic development. Science 301:1911-1914.

Künnapuu J, Tauscher PM, Tiusanen N, Nguyen M, Löytynoja A, Arora K, Shimmi O. 2014. Cleavage of the *Drosophila screw* prodomain is critical for a dynamic BMP morphogen gradient in embryogenesis. Developmental Biology 389:149-159.

Lamka ML, Lipshitz HD. 1999. Role of the amnioserosa in germ band retraction of the *Drosophila melanogaster* embryo. Developmental Biology 214:102-112.

Levayer R, Lecuit T. 2013. Oscillation and polarity of E-cadherin asymmetries control actomyosin flow patterns during morphogenesis. Developmental Cell 26:162-175.

Liberman LM, Reeves GT, Stathopoulos A. 2009. Quantitative imaging of the Dorsal nuclear gradient reveals limitations to threshold-dependent patterning in *Drosophila*. Proceedings of the National Academy of Sciences 106:22317-22322.

Lynch HE, Crews SM, Rosenthal B, Kim E, Gish R, Echiverri K, Hutson MS. 2013. Cellular mechanics of germ band retraction in *Drosophila*. Developmental Biology 384:205-213.

Lynch HE, Veldhuis J, Brodland GW, Hutson MS. 2014. Modeling cell elongation during germ band retraction: cell autonomy versus applied anisotropic stress. New Journal of Physics 16:55003-55003.

Lynch JA, El-Sherif E, Brown SJ. 2012. Comparisons of the embryonic development of *Drosophila*, *Nasonia*, and *Tribolium*. Wiley Interdisciplinary Reviews: Developmental Biology 1:16-39.

Ma X, Lynch HE, Scully PC, Hutson MS. 2009. Probing embryonic tissue mechanics with laser hole drilling. Phys Biol 6:036004.

Martin AC. 2010. Pulsation and stabilization: contractile forces that underlie morphogenesis. Developmental Biology 341:114-125.

Mashburn DN, Lynch HE, Ma X, Hutson MS. 2012. Enabling user-guided segmentation and tracking of surface-labeled cells in time-lapse image sets of living tissues. Cytometry A 81:409-418.

Mazumdar A, Mazumdar M. 2002. How one becomes many: blastoderm cellularization in *Drosophila melanogaster*. Bioessays 24:1012-1022.

McCall K, Peterson JS. 2004. Detection of apoptosis in *Drosophila*. Methods Mol Biol 282:191-205.

Mizutani CM, Nie Q, Wan FYM, Zhang Y-T, Vilmos P, Sousa-Neves R, Bier E, Marsh JL, Lander AD. 2005. Formation of the BMP activity gradient in the *Drosophila* embryo. Developmental Cell 8:915-924.

Morisalo D, Anderson KV. 1995. Signaling pathways that establish the dorsal-ventral pattern of the *Drosophila* embryo. Annual Review of Genetics 29:371-399.

Moussian B, Roth S. 2005. Dorsoventral axis formation in the *Drosophila* embryo—shaping and transducing a morphogen gradient. Current Biology 15:R887--R899.

Neuman KC, Nagy A. 2008. Single-molecule force spectroscopy: optical tweezers, magnetic tweezers and atomic force microscopy. Nature Methods 5:491-505.

Nguyen M, Park S, Marqués G, Arora K. 1998. Interpretation of a BMP activity gradient in *Drosophila* embryos depends on synergistic signaling by two type I receptors, SAX and TKV. Cell 95:495-506.

Nobes CD, Hall A. 1995. Rho, rac, and cdc42 GTPases regulate the assembly of multimolecular focal complexes associated with actin stress fibers, lamellipodia, and filopodia. Cell 81:53-62.

Oda H, Tsukita S. 2001. Real-time imaging of cell-cell adherens junctions reveals that *Drosophila* mesoderm invagination begins with two phases of apical constriction of cells. J Cell Sci 114:493-501.

Panfilio KA. 2008. Extraembryonic development in insects and the acrobatics of blastokinesis. Developmental Biology 313:471-491.

Panfilio KA, Roth S. 2013. Development: getting into the groove, or evolving off the rails? Current Biology 23:R1101--R1103.

Paré AC, Vichas A, Fincher CT, Mirman Z, Farrell DL, Mainieri A, Zallen JA. 2014. A positional Toll receptor code directs convergent extension in *Drosophila*. Nature 515:523-527.

Pickering K, Alves-Silva J, Goberdhan D, Millard TH. 2013. Par3/Bazooka and phosphoinositides regulate actin protrusion formation during *Drosophila* dorsal closure and wound healing. Development 140:800-809.

Pollard TD, Cooper JA. 1986. Actin and actin-binding proteins: a critical evaluation of mechanisms and functions. Annual Review of Biochemistry 55:987-1035.

Pope KL, Harris TJC. 2008. Control of cell flattening and junctional remodeling during squamous epithelial morphogenesis in *Drosophila*. Development 135:2227-2238.

Rafiqi AM, Lemke S, Ferguson S, Stauber M, Schmidt-Ott U. 2008. Evolutionary origin of the amnioserosa in cyclorrhaphan flies correlates with spatial and temporal expression changes of *zen*. Proceedings of the National Academy of Sciences 105:234-239.

Rafiqi AM, Lemke S, Schmidt-Ott U. 2010. Postgastrular *zen* expression is required to develop distinct amniotic and serosal epithelia in the scuttle fly *Megaselia*. Developmental Biology 341:282-290.

Rafiqi AM, Park C-H, Kwan CW, Lemke S, Schmidt-Ott U. 2012. BMP-dependent serosa and amnion specification in the scuttle fly *Megaselia abdita*. Development 139:3373-3382.

Rasband WS. 1997-2017. ImageJ. In. Bethesda, Maryland, USA: U. S. National Institutes of Health.

Rauzi M, Lenne P-F, Lecuit T. 2010. Planar polarized actomyosin contractile flows control epithelial junction remodelling. Nature 468:1110-1114.

Ray HJ, Niswander L. 2012. Mechanisms of tissue fusion during development. Development 139:1701-1711.

Reed BH, Wilk R, Schöck F, Lipshitz HD. 2004. Integrin-dependent apposition of *Drosophila* extraembryonic membranes promotes morphogenesis and prevents anoikis. Current Biology 14:372-380.

Reeves GT, Trisnadi N, Truong TV, Nahmad M, Katz S, Stathopoulos A. 2012. Dorsal-ventral gene expression in the *Drosophila* embryo reflects the dynamics and precision of the dorsal nuclear gradient. Developmental Cell 22:544-557.

Rickoll WL. 1976. Cytoplasmic continuity between embryonic cells and the primitive yolk sac during early gastrulation in *Drosophila melanogaster*. Developmental Biology 49:304-310.

Rickoll WL, Counce SJ. 1980. Morphogenesis in the embryo of *Drosophila melanogaster*—germ band extension. Wilhelm Roux's Archives of Developmental Biology 188:163-177.

Ridley AJ, Hall A. 1992. The small GTP-binding protein rho regulates the assembly of focal adhesions and actin stress fibers in response to growth factors. Cell 70:389-399.

Ridley AJ, Paterson HF, Johnston CL, Diekmann D, Hall A. 1992. The small GTP-binding protein rac regulates growth factor-induced membrane ruffling. Cell 70:401-410.

Rugendorff A, Younossi-Hartenstein A, Hartenstein V. 1994. Embryonic origin and differentiation of the *Drosophila* heart. Wilhelm Roux's Archives of Developmental Biology 203:266-280.

Rushlow C, Colosimo PF, Lin M-c, Xu M, Kirov N. 2001. Transcriptional regulation of the *Drosophila* gene *zen* by competing Smad and Brinker inputs. Genes & Development 15:340-351.

Saias L, Swoger J, D'Angelo A, Hayes P, Colombelli J, Sharpe J, Salbreux G, Solon J. 2015. Decrease in cell volume generates contractile forces driving dorsal closure. Developmental Cell 33:611-621.

Schaerlinger B, Launay JM, Vonesch JL, Maroteaux L. 2007. Gain of affinity point mutation in the serotonin receptor gene 5-HT$_{2Dro}$ accelerates germband extension movements during *Drosophila* gastrulation. Developmental Dynamics 236:991-999.

Schmidt-Ott U. 2000. The amnioserosa is an apomorphic character of cyclorrhaphan flies. Development Genes and Evolution 210:373-376.

Schmidt-Ott U, Rafiqi AM, Lemke S. 2010. Hox3/zen and the evolution of extraembryonic epithelia in insects. In: Hox Genes: Studies from the 20th to the 21st Century. Springer. pp 133-144.

Schweisguth F, Vincent A, Lepesant J-A. 1991. Genetic analysis of the cellularization of the *Drosophila* embryo. Biology of the Cell 72:15-23.

Schöck F, Perrimon N. 2002. Cellular processes associated with germ band retraction in *Drosophila*. Developmental Biology 248:29-39.

Schöck F, Perrimon N. 2003. Retraction of the *Drosophila* germ band requires cell-matrix interaction. Genes & Development 17:597-602.

Sharma R, Beermann A, Schröder R. 2013. The dynamic expression of extraembryonic marker genes in the beetle *Tribolium castaneum* reveals the complexity of serosa and amnion formation in a short germ insect. Gene Expression Patterns 13:362-371.

Shimmi O, Umulis D, Othmer H, O'Connor MB. 2005. Facilitated transport of a Dpp/Scw heterodimer by Sog/Tsg leads to robust patterning of the *Drosophila* blastoderm embryo. Cell 120:873-886.

Simonova OB, Burdina NV. 2009. Morphogenetic movement of cells in embryogenesis of *Drosophila melanogaster*: mechanism and genetic control. Russian Journal of Developmental Biology 40:283-299.

Solon J, Kaya-Çopur A, Colombelli J, Brunner D. 2009. Pulsed forces timed by a ratchet-like mechanism drive directed tissue movement during dorsal closure. Cell 137:1331-1342.

St Johnston D, Nüsslein-Volhard C. 1992. The origin of pattern and polarity in the *Drosophila* embryo. Cell 68:201-219.

Stark KA, Yee GH, Roote CE, Williams EL, Zusman S, Hynes RO. 1997. A novel α integrin subunit associates with βPS and functions in tissue morphogenesis and movement during *Drosophila* development. Development 124:4583-4594.

Stronach BE, Perrimon N. 2001. Investigation of leading edge formation at the interface of amnioserosa and dorsal ectoderm in the *Drosophila* embryo. Development 128:2905-2913.

Sutherland DJ, Li M, Liu X, Stefancsik R, Raftery LA. 2003. Stepwise formation of a SMAD activity gradient during dorsal-ventral patterning of the *Drosophila* embryo. Development 130:5705-5716.

Tada M, Heisenberg C-P. 2012. Convergent extension: using collective cell migration and cell intercalation to shape embryos. Development 139:3897-3904.

Toyama Y, Peralta XG, Wells AR, Kiehart DP, Edwards GS. 2008. Apoptotic force and tissue dynamics during *Drosophila* embryogenesis. Science 321:1683-1686.

Valanne S, Wang J-H, Rämet M. 2011. The *Drosophila* Toll signaling pathway. Journal of Immunology 186:649-656.

van der Zee M, Berns N, Roth S. 2005. Distinct functions of the *Tribolium zerknüllt* genes in serosa specification and dorsal closure. Current Biology 15:624-636.

Veldhuis JH, Mashburn D, Hutson MS, Brodland GW. 2015. Practical aspects of the Cellular Force Inference Toolkit (CellFIT). Methods in Cell Biology 125:331-351.

Wada A, Kato K, Uwo MF, Yonemura S, Hayashi S. 2007. Specialized extraembryonic cells connect embryonic and extraembryonic epidermis in response to Dpp during dorsal closure in *Drosophila*. Developmental Biology 301:340-349.

Walters JW, Dilks SA, DiNardo S. 2006. Planar polarization of the denticle field in the *Drosophila* embryo: Roles for Myosin II (Zipper) and Fringe. Developmental Biology 297:323-339.

Wang X, He L, Wu YI, Hahn KM, Montell DJ. 2010. Light-mediated activation reveals a key role for Rac in collective guidance of cell movement in vivo. Nat Cell Biol 12:591-597.

Weisstein EW. 2017. "Area Moment of Inertia." From *MathWorld* --A Wolfram Web Resource. In.

Wells AR, Zou RS, Tulu US, Sokolow AC, Crawford JM, Edwards GS, Kiehart DP. 2014. Complete canthi removal reveals that forces from the amnioserosa alone are sufficient to drive dorsal closure in *Drosophila*. Molecular Biology of the Cell 25:3552-3568.

Wood W, Jacinto A, Grose R, Woolner S, Gale J, Wilson C, Martin P. 2002. Wound healing recapitulates morphogenesis in *Drosophila* embryos. Nature Cell Biology 4:907-912.

Wotton KR, Jiménez-Guri E, Matheu BG, Jaeger J. 2014. A staging scheme for the development of the scuttle fly *Megaselia abdita*. PLOS ONE 9.

Wu YI, Frey D, Lungu OI, Jaehrig A, Schlichting I, Kuhlman B, Hahn KM. 2009. A genetically-encoded photoactivatable Rac controls the motility of living cells. Nature 461:104-108.

Yip ML, Lamka ML, Lipshitz HD. 1997. Control of germ-band retraction in *Drosophila* by the zinc-finger protein HINDSIGHT. Development 124:2129-2141.

Zallen JA, Wieschaus E. 2004. Patterned gene expression directs bipolar planar polarity in *Drosophila*. Developmental Cell 6:343-355.